Modelling of FMCW ground penetrating radar

Zhang, X.

Award date:
1997

Awarding institution:
University of Bath

MODELLING OF FMCW GROUND PENETRATING RADAR

Submitted by X.Zhang
for the Degree of PhD.
of the University of Bath
1997

ProQuest LLC
789 East Eisenhower Parkway
P.O. Box 1346
Ann Arbor, MI 48106-1346

To my parents, my husband and my lovely son

Summary

This thesis presents a Frequency Modulation Continuous Wave(FMCW) signal processing mathematical model and target analysis software concerning a sponsored contract work to build a new FMCW radar system for measurement of the depth of underground cables and pipes.

This system consists of five head antennas including two transmitters and three receivers which enables the novel approach of triangulation and convolution to be implemented. This system facilitates accurate measurement of the depth of the shallowest target and then the calculation of the safe digging depth to that target without knowing the refractive index of the ground media.

The mathematical model has been established to model this FMCW radar system and tested successfully using simulated target environment and radar parameters in both single or multi-target situations.

The target analysis algorithm has been developed and tested successfully on an experimental FMCW radar system in a multi-target sand filled test site. The results show the software can detect targets and calculate their depth correctly.

Several methods of improving system detection resolution have been investigated. Matched filter and clutter rejection filters show different degrees of improvement. The principles of synthetic aperture algorithm applied on FMCW radar are also presented.

Acknowledgements

I would like to extend my thanks to Dr. Steve Pennock and Dr. Miles Redfern for their helpful guidance as supervisors and their many valuable suggestions that have done much to enhance my research efforts.

I would also like to express my thanks to Dr. Hugh Burchett for his kind, patient and valuable advice and help during my work. I must also thank the other postgraduates and staff in the department for their help during these years.

I am also indebted to London Electricity for their financial support for this research work.

Abbreviations

GPR	Ground Penetrating Radar
FMCW	Frequency Modulated Continuous Wave
FDTD	Finite Difference Time Domain
CW	Continuous Wave
VCO	Voltage Control Oscillator
UHF	Ultra High Frequency
FFT	Fast Fourier Transform
IFFT	Inverse Fast Fourier Transform
SDD	Safe Digging Depth

Glossary of Terms

a_0	conversion constant
A	wave amplitude
A_t	transmitted signal amplitude
A_r	received signal amplitude
B	received mixer signal amplitude
c	the speed of light
d	target depth
D	separation between transmitter and receiver
f	frequency
f_0	base frequency of FMCW radar
f_t	transmitted frequency
f_d	frequency difference
f_{d1}, f_{d2}	frequency difference from T_A to R_A and T_A to R'_A
$f_t(t)$	instantaneous transmitted frequency
$f(y - y_0)$	range function in $U(x, y)$
$F(\omega)$	Fourier Transform of input signal
$F_t(\omega)$	Fourier Transform of input template signal
Δf	change of frequency
G_a	constant in matched filter transfer function
G_t	transmitter antenna gain
G_r	receiver antenna gain
$G(\omega)$	desired output of triangular templating
$g(x_0, y_0)$	target distribution function
$h_1(x - x_0, y_0), h_2(y - y_0)$	phase function in $U(x, y)$
$H(\omega), H_1(\omega), H_2(\omega)$	filter transfer function
$I(\omega)$	output spectrum of inverse filter
k	frequency spacing
k_0	free space propagation wavenumber
K_1, K_2, K	constants in filter transfer function
l_1, l_2	soil layer thickness

L	scan width in azimuth direction
L_p	path propagation loss due to media attenuation
M	number of time samples
m	sampling number
n	refractive index
n_1, n_2	refractive index
$n_{21}, n_{22}, n_{23}, n_{31}, n_{32}, n_{33}$	refractive index in trenched media
$n(t)$	white noise
$n_i(t)$	clutter
$N(\omega)$	clutter spectrum
$N_0/2$	power density spectrum of white noise
n'	the real part of n
n''	the imaginary part of n
$O(\omega)$	output of triangular templating
P_t	transmitter power
$P_t(t)$	transmitter power
P_r	receiver power
r	target distance
r_1	distance from transmitter to target
r_2	distance from target to receiver
$resp(t)$	convolution of input signal $sig(t)$ and template function $templ(t)$
$RESP(X)$	Fourier Transform of $resp(t)$
R	target distance
R_A, R'_A, R_B, R'_B	receiver antenna head
R_1, R_2	target distance from T_A to R_A and T_A to R'_A
R_X	receiver
$sig(t)$	input signal
$SIG(X)$	Fourier Transform of $sig(t)$
$S(f)$	Fourier Transform of $S(t)$

$S_t(t)$	transmitted signal waveform
$S_r(t)$	received signal waveform
$S(t)$	receiver mixer output
$s_i(t)$	clutter filter input signal
$S_i(\omega)$	Fourier Transform of $s_i(t)$
$S_i^\star(\omega)$	conjugate of $S_i(\omega)$
$S(\omega)$	Fourier Transform of input signal $S(t)$
$S_n(\omega)$	power density spectrum of clutter
T	ratio of τ_1 and τ_2
T_A, T_B	transmitter antenna head
T_d	target diameter
T_X	transmitter
t_d	time delay in filter transfer function
$templ(t)$	template function
$TEMPL(X)$	Fourier Transform of $templ(t)$
T_s	frequency sweep time
Δt	frequency sweep time
T_r	repetition rate
$T(\omega)$	template function in frequency domain
$U(\omega)$	output of filter processing
$U(x, y)$	space variable function
v	the velocity of propagation in the media
x_0, y_0	point target position
$x(t)$	input time signal plus clutter
x_1, x_2	target propagation path vertical position in model
x_{ta}, y_{ta}	target position in model
x_{un}, y_{un}	transmitter/receiver position in model
$y_0(t)$	output from clutter filter
y_1, y_2	target propagation path horizontal position in model
y_{t1}, y_{t2}	trench boundary

Symbols

$\lambda, \lambda_t(t)$	instantaneous wavelength of the transmitted waveform
α	coefficient in window function
σ	Radar Cross Section of the target
θ	the angle between ground to target position
$\theta_1, \theta_2 ... \theta_6$	the refractive angles at soil interface
θ_i	incident angle
θ_r	reflected angle
θ_t	refracted angle
τ_d	time delay between transmitted signal and received signal
$\tau_1, \tau_2, \tau_3, \tau_4$	time delay from four channels
	(T_A to R_A, T_B to R_B, T_A to R'_A and T_B to R'_B)
ω	circular frequency
$\omega_t(t)$	instantaneous transmitted signal angular frequency
$\omega_r(t)$	instantaneous received signal angular frequency
$\omega(n)$	window function
Γ	reflection coefficient

Contents

Chapter 1

Introduction

1.1 Outline

This chapter provides background information on Ground Penetrating Radar(GPR), its applications, and the motivation behind the research work. The chapter concludes with an outline of the work contained in the thesis.

1.2 Ground Penetrating Radar

Radar means "Radio Detection and Ranging". The first use of electromagnetic signals to determine the presence of remote terrestrial metal objects is generally attributed to Hülsmeyer in 1904 [38], but the first description of their use for location of buried objects appeared six years later in a German patent by Leimbach and Löwy [39]. For almost 90 years, ground penetrating radar which uses a wide range of electromagnetic techniques to detect objects or interfaces buried beneath the earth's surface has been the subject of research and development.

The application range of GPR has been expanded steadily from the geophysical and geological needs [1] [2] [3] into archaeology [4] [5], road [6] [7] and railbed quality assessment, location of voids and containers [8], tunnels [9] [10] and mineshafts [11] [12],

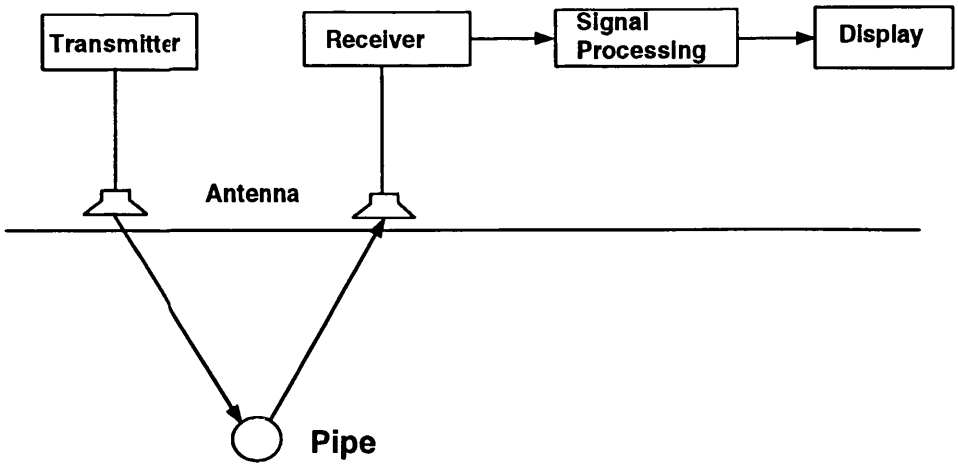

Figure 1.1: General Ground Penetrating Radar(GPR) system

pipe and cable detection [13] [14] [15] [16], as well as remote sensing by satellite.

The essence of the techniques is not different from that of conventional, free-space radar, but ground penetrating radar must take on an added significance of propagation loss, clutter characteristics and target characteristics which are distinctly different. Further, because of the interface between air and ground, the surface reflected wave can easily be stronger than that from the targets. The short distances involved in multi-target situations also produce serious interactions which complicate analysis.

1.2.1 GPR Systems

Ground penetrating radar system has been built using a variety of modulation types depending on the particular requirements of penetration depth, resolution, target characteristics, software available for data processing, reduction of electromagnetic interference, system size and cost. Most GPR system can be mainly divided into three types according to its modulation methods, that is continuous wave(CW), frequency modulated continuous wave(FMCW) and pulse radar. The general GPR system as shown in Figure 1.1 is composed of transmitter, receiver, antennas, signal processing and display.

Most early GPR systems use CW radar which use a single frequency transmission.

The narrowband nature of the transmissions means that problems of broadband antenna design and high-speed data capture are avoided, but because of single frequency transmission, the radar return signal will contain limited target information, which is the serious disadvantage. Several early patents [40]— [48] described the CW operation which use diffraction effects due to underground features, and the reliance on conductivity variations to produce scattering.

The majority of current GPR systems use impulse radar techniques. Impulse radar transmits the baseband narrow pulse whose width is typically of the order of 1ns in GPR applications. The production of such a pulse can be quite difficult. The return signal has a time delay which is proportional to the target distance and the spectrum of return signal contains a great deal of information about the target. The design of antenna can be complicated due to bandwidth and low distance requirements. The work of Hülsenbeck in 1926 [49] appears to be the first use of pulse techniques to determine the structure of buried features. Pulse techniques were developed extensively over the next 50 years as a means of probing in ice, fresh water, salt deposits, desert sand, rock formations and coal seams [17].

Step frequency radar [18] [19] [20] employs coherent detection and utilizes both the phase and amplitude of the target reflected signal. This radar can achieve a resolution of much less than one wavelength by using an accurate phase measurement. However, this radar is more complicated, requiring full vector reception.

In FMCW radar the transmitted signal is continuously swept in frequency. The received signal is mixed with a sample of the currently transmitted wave to produce a difference frequency. The difference frequency depends on the time delay between transmitted and received signal, and hence the range to the buried target. FMCW radar has the main advantages of easier control of transmitted spectral shape, high resolution and wide dynamic range. FMCW systems have been used by Clarricoats, Olver and others in [21] [22] [23]. In these papers they described FMCW radar to locate and characterise shallow targets.

1.2.2 Antenna

Unlike an atmosperic radar the design of ground penetrating radar antennas must match to the characteristics of the medium of propagation and to the geometrical shape of the target, so the design of GPR antennas stress parameters such as impulse response, fractional bandwidth and polarisation state. The crosscoupling between closely-spaced transmitter and receiver, interaction of the reactive field of the antenna with the medium of propagation, as well as the antenna geometry are also important features to be taken into account.

Four major types of antenna have been used successfully in ground penetrating radar [17], which are element antennas, travelling-wave antennas, angle independent antennas and aperture antennas.

1.2.3 Signal Processing

Signal processing techniques are required for the extraction of information from the signal generated by a radar system. Because of the action of clutter, and the similarity between delays within circuits and the time delays between the signal transmitted to the target and the signal received from it, the signal processing for ground penetrating radar is more complicated than free-space radar.

Several signal processing techniques have been adopted to process the GPR signals, including correlation, reference subtraction and filtering [7] to reduce clutter and noise. Synthetic aperture techniques [24] [25] are also been used to produce images of the infill and objects buried in it.

The signal processing work for ground penetrating radar can be considered at different levels as following:

1. Processes applied to raw time-waveform data
2. Processes applied to a collection of time-waveforms, either along a line or over an area

3. Processes appled in two or three dimensions

4. Processes appied to perform reconstruction of features so that the final image only contains nformation in a predetermined form

5. Processes whi:h extract information according to a user-controlled menu with labelling, discrimination and the possibility of addition of independently derived supporting material.

The majority of signal processing work are at level 1 and 2 some at level 3. Levels 4 and 5 are currently the subject of research work in the field of advanced image processing, information technology and expert systems. Their practical application to the handling of GPR data is still at an early stage.

1.3 Applications of GPR

Ground penetrating radar [17] techniques have many applications, including geophysical prospecting, subsurface mapping, structural appraisal, the location of pipes and cables, and the detection of explosive mines. Comparing with some traditional method to detect underground target, GPR technique has the advantages of fast detection, high resolution, easy handle operation and low cost. GPR has advantages over seismic methods because any dielectric variation, not necessarily involving conductivity, will also produce reflections. Also another advantage of GPR over seismic is in the remote application such as lunar investigate. Remote transducers are possible because the dielectric impedance ratio between free space and soil materials, typically from 2 to 4, is very much less than the corresponding ratio for acoustic impedances, by a factor which is typically of order 100. So GPR techniques have been widely used in civil engineering and military application.

The application of ground penetrating radar to geophysical prospecting [2] [26], that is detecting the layers present in a structure, is the oldest of the applications since the technology required to generate the radar pulses is less demanding than for higher resolution and short range systems. Systems designed for this purpose operate at relatively

low frequencies of tens to hundreds of MegaHertz to achieve penetration of hundreds of metres in rock.

Archaeological surveying [27] and general mapping of areas of ground normally uses frequencies of between 200 to 1000 MHz [4], which provides a lower penetration into the earth, but a higher resolution. These systems are required to map areas and identify objects such as water tables, disturbed earth, bodies, voids, pipes and cables. The majority of commercial systems are designed primarily for this application and a number of companies operate surveying services. The data produced from the surveys often require significant post-processing to interpret the results, and hence the software can take account of up to 25% of the equipment cost.

The use of ground penetrating radar systems to perform structural appraisal of buildings and tunnels is of increasing interest [22]. These systems are designed to detect voids and concrete reinforcing rods with a lower depth of penetration required than for a ground mapping system. The frequency of operation can be as high as 2GHz [22] to achieve good resolution. The moisture content of buildings is normally lower than that of soil, therefore a lower transmitter power can be used.

A related application is the mapping of road pavement structures [28] [29] [8] [30] [31], to detect voids [32] and accurately measure the depths of the pavement layers. The hardware requirement is significantly different from a structural appraisal system. Pavement mapping systems are normally mounted on a vehicle and are designed to survey a single carriageway with one sweep. This normally requires a multi-channel system with the processing power to handle very high data rates [33].

The location of pipes and cables [16] [34] [50] using ground penetrating radar has predominantly been concerned with the mapping of utilities prior to the laying of new services using excavation or micro-tunneling [35]. These systems produce an image showing the location of pipes and cables in the scanned area. One requirement for this application is that the area is surveyed in the smallest amount of time. The amount of signal processing that is required will vary, and is dependent on the training and experience of the operator. Significant post-processing is generally required to produce a clear image.

The systems with the highest resolution are those required to identify small objects such as explosive mines [11]. These systems frequently use a library of target responses to increase the probabilty of detection in real time. They normally require high resolution with a lower penetration than other applications.

The number of companies involved demonstrates the interest shown in ground penetrating radar systens, specifically amongst the UK, US and Japanese utilities [15]. These companies have all developed equipment to map an area of ground and trace the position of pipes and cables down to a depth of 3.5m to 4m, with resolutions of approximately 10 to 20cm. Some of the equipment also provides information concerning the geological profile, which is of interest where micro-tunnelling machines are used instead of conventional excavation techniques [35].

Sensors and Software Inc., Canada (PulseEKKO Systems) are most widely used for geological prospecting and mapping. A range of transducers are available which operate at 25, 50, 100 and 200MHz, and offer good depth capability, but at the cost of poor resolution. A higher frequency transducer is believed to have been recently made available (PulseEKKO IV-H) which gives better resolution.

Geophysical Survey Systems Inc., USA (GSSI) produce a range of Subsurface Interface Radars (SIR Family) that are used for geological prospecting and general mapping of areas of ground. The equipment can also be used for the location of pipes and pavement mapping, but with limited success. A study by BRGM, France, showed an 80% success rate with depth errors of approximately 10% at 500MHz. The GSSI equipment is probably the most widely used for mapping purposes and transducers are available at frequencies of 24 to 50MHz (continuous); 80, 120, 300, 500 and 900MHz. The SIR-10 system which is the most recent model can store data digitally and operate as a multi-channel system if required. The multi-channel system can use pairs of transducers at different frequencies or up to four transducers at the same frequency. The signal processing enables this system to map a wider swath of ground or provide increased resolution over a narrow area. The signal processing also enables the equipment to focus on details at a particular depth. The data bandwidth of the current system is being enhanced to enable the equipment to be used for pavement mapping.

A number of agencies have developed ground penetrating radar equipment to fulfil one particular role, therefore provide a performance benefit.

EMRAD are offering a survey service using a multi-channel system [7], [36] with up to four transmit/receive modules that offers either improved resolution or a wider area coverage. The PIPEHAWK gives a real time readout of the area scanned and depth information can be calculated using target returns to compute the refractive index. Both EMRAD systems can log data to an external computer to post-process information.

To date, the only system that has specifically been designed to measure the depth of pipes and cables has been the TERRASCAN system developed by the Ohio State University in conjunction with the Electric Power Research Institute (EPRI), USA [7]. This equipment was manufactured by MACom Inc. (formerly Microwave Associates) and was still in production in 1988 although no further details have been obtained. EPRI withdrew funding in 1988 after 10 years of work had failed to obtain any significant results.

The Tokyo Electric [15] system has been developed to provide three dimensional mapping of buried utilities, and does not require any data interpretation. This is achieved by using extremely powerful and expensive post-processing techniques.

The means by which the dielectric constant (hence the calibrated depth) is determined varies widely between systems. Some systems use a simple estimate, or a database of values. Alternatively, samples of earth can be taken and the dielectric constant is measured as part of the post-processing work.

The pavement mapping ground penetrating radar systems frequently utilise multiple channels and are usually mounted on a vehicle, enabling them to map a carriageway with one sweep. This leads to a very high data rate and the processing system has to be very powerful to cope with it. The majority of the research in this area is mainly concerned with increasing the data bandwidth of the system to provide better resolution. The aim of most pavement mapping systems is to cover a large survey area, even if this requires post-processing to increase the resolution of the images [31], [37].

In the USA, Ohio State University [7] have been researching ground penetrating

radar systems for a number of years in conjunction with US utility companies and research agencies (EPRI, Gas Research Institute) which has led to the TERRASCAN system manufactured by MA Com. The wide range of applications means that optimum results are obtained when the ground penetrating radar equipment is designed to meet a particular need, as opposed to using a general purpose design.

Most of the systems are general purpose in nature, and consequently a significant amount of interpretation is required, and hence a high level of training of operators. In addition to the generally high price due to the hardware requirements, this makes these systems unsuitable for widespread use.

The majority of the ground penetrating radar systems use pulse radar techniques and have had a varying degrees of success. A British Gas system reached the pre-production stage, however the practical use of the system was finally envisaged as a tool to provide depth and position information to interface to a digital mapping system. It was expected to allow each trenching gang to be equipped with a unit.

1.4 The Purpose of this Research Project

This thesis concerns the use of ground penetrating radar to detect the presence of buried cables or pipes to enhance the safety of trenching personnel. The object is to provide a display of the "safe digging depth" of the upper surface of a buried object when the system is directly above a target.

This system must be portable, provide real-time processing and display, be easy to handle and its use must be straightforward to field personnel who have only been given a basic introduction to its use.

FMCW radar has been chosen for this project because of its high resolution and wide dynamic range and since it is suitable for short range detecting. A pulse radar system could be used to determine the target safe digging depth in this project, but high resolution and accuracy requirements in the time domain impose severe restrictious for pulse radar design because the very short pulse width(1–3nsec) requires specialised circuits, particularly if predistortion of the transmitted pulse is to be used. Predistortion

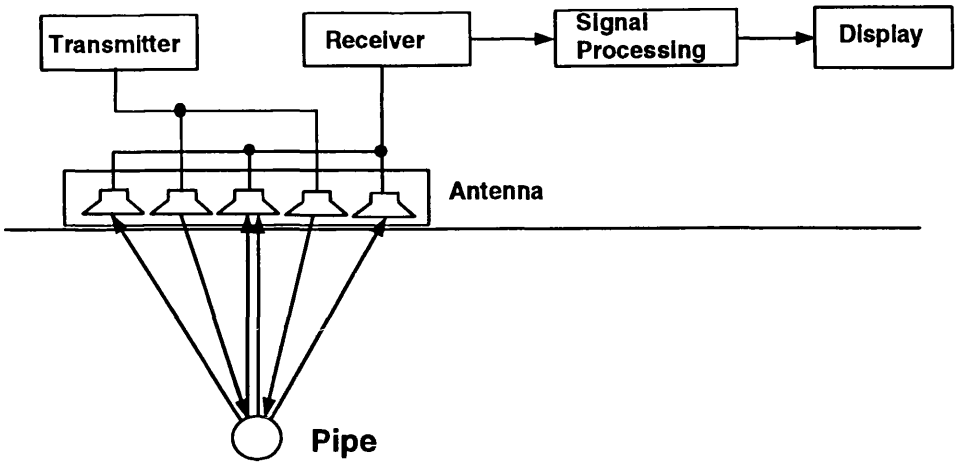

Figure 1.2: 5 Head Ground Penetrating Radar(GPR) system

in the FMCW radar system requires a simple ramp in output power as the frequency is increased. FMCW radar utilizes the continuous wave principle for which the range accuracy is determined by the frequency resolution. This can be adjusted to a desired value. In addition the frequency ranges used are similar to the commonly used TV and mobile telephone bands where relatively cheap mass produced integrated circuits are available.

This FMCW GPR system is unique and uses a 5 antenna head structure in order to provide accurate measurement of the depth of a shallowest target. The 5 head system as seen in Figure 1.2 has two transmitters and three receivers, one pair of transmitter and receiver has been used at one time. This 5 head system provides four combinations of transmitter and receiver which enables the target triangulation and convolution techniques to be used to accurately obtain the depth of targets.

The target triangulation technique uses the two propagation paths to eliminate the unknown refractive index of the propagation media. The convolution approach convolves the signals from two channels and enables the system to concentrate on targets directly below the centre point of the measurement unit. Data from the two channels is combined so that reflections from targets not on the centre line are attenuated. The measured depth of the shallowest target corresponds to the measured depth of the upper surface

of the object causing a significant reflection of the transmitted signal.

Mathematical models have been developed to simulate the FMCW radar system and process radar return signals in order to predict the system reaction to realistic infill and target situations. It has been designed to simulate the FMCW transmitted signal generation, the return signal and soil media. The model has been divided into two parts: target simulation and target analysis. The target simulation model simulates the FMCW UHF system signal propagation in uniform, layered and trenched soil, and then produces the sampled time domain signals. The target analysis model takes the Fast Fourier Transform(FFT) of these sampled signals, convolves pairs of receiver responses and calculates the desired unit movement direction and target safe digging depth. The target analysis software forms the basis for the safe digging depth calculations used in the experimental system.

Different methods have also been investigated to improve system detection resolution. Reference signal subtraction and a 'limiter' algorithm have been employed to improve system resolution which has been shown to reduce most of clutter signals.

A set of matched filter and clutter rejection filter algorithm have also been produced and used on the subtracted data. This has resulted in a improved resolution and clarity of image for multi-target situations.

Synthetic aperture algorithm has been studied and tested using simulated and real data. The results show a improved horizontal resolution of the target image on the simulated data.

A dedicated sand filled test site has been built in the University campus and the experimental system has been tested in this test site successfully. The presence of multiple targets can be detected and their depths has been computed correctly. Tests also have been carried out on tarmac roadway.

1.5 Outline of this thesis

This thesis describes work of the modelling and processing of FMCW ground penetrating radar system signal. There are seven chapters and six appendices.

Chapter One provides a brief introduction of GPR system, its applications, the purpose of this research work and the outline of this thesis.

Chapter Two provides a summary of a literature review which includes information concerning modelling of GPR, ray tracing methods and the signal processing methods of FMCW radar. It also gives conclusions from the literature search on signal processing for FMCW ground penetrating radar.

Chapter Three describes the basis of FMCW radar and its signal processing theory, mathematical model requirement and structure. The target simulation model includes UHF signal calculation, and signal propagation and target path calculation. This is based on the ray tracing method considering the refraction and reflection of signals at each index boundary.

Chapter Four provides the target analysis model which includes an FFT algorithm, convolution algorithm, and safe digging depth and unit movement calculation. The chapter also gives the details of the effect of timing quantisation errors on the safe digging depth calculation. Some spectrum processing algorithms such as window function, target templating and different filters are described which have been investigated to improve system resolution. The principles of synthetic aperture algorithms applied to the FMCW radar image processing have also been provided.

Chapter Five presents and discusses simulation results for uniform, layered and trenched soil conditions for single and multiple targets from the signal processing mathematical model. The chapter also provides details of the horizontal and vertical resolution for the mathematical model. 2D scan simulation results and the results of the synthetic aperture algorithm applied to simulated data are also presented.

Chapter Six provides details of the applications of experimental results to the analysis model. The chapter also provides the results from a set of matched filter, clutter

rejection filter and synthetic aperture algorithms applied to real data,

Chapter Seven describes the conclusion of the research work undertaken and the further work which is envisaged concerning the mathematical algorithms to improve the detection resolution.

Appendix A provides the derivation of safe digging depth algorithm.

Appendix B describes the secant method flowchart to solve the non-linear equation.

Appendix C provides the target path functions in layered media for the target simulation model.

Appendix D provides the target path functions in trenched media for the target simulation model.

Appendix E provides the current FMCW system configuration.

Appendix F examines the convolution algorithm using $\frac{\sin x}{x}$ functions.

References

[1] By TL et al. Geo-radar development at the Norwegian Geotechnical Institute. In *Fourth International Conference on Ground Penetrating Radar*, volume 1, pages 21–28, 1992. Author(s) with Norwegian Geotechnical Institute (NGI).

[2] Daniels DJ. The use of radar in geophysical prospecting. In *RADAR 77*, volume 1, pages 540–546. IEE Publ. No. 155, 1977. Author(s) with Plessey Radar.

[3] Finkelstein M. Subsurface radar: Principle problems of development and practical use. In *IEEE International Geoscience and Remote Sensing Symposium (IGARSS)*, volume 3, pages 2145–2147, 1991. Author(s) with Riga Institute of Civil Aviation Engineers.

[4] David A and Fookes G et al. Ground penetrating radar for archaeology. Technical report, Ancient Monuments Laboratory, 1992. Author(s) with Ancient Monuments Laboratory.

[5] Goodman D and Nishimura Y. 2D synthetic radargrams for archaeological investigation. In *Fourth International Conference on Ground Penetrating Radar*, volume 1, pages 339–343, 1992. Author(s) with University of Miami, Japan.

[6] Bashforth M and Koppenjan S. Ground penetrating radar applications for non-destructive inspection of construction work. In *54th Meeting of the European Association of Exploration Geophysicists*, volume 1, page 408, 1992. Author(s) with US Dept. of Energy Special Technology Lab.

[7] Caldecott R et al. Underground mapping of utility lines using impulse radar. *IEE Proc. Pt.F*, 135(4):343–353, August 1988. Author(s) with Ohio State University and EPRI.

[8] Lau CL. Using ground penetration radar technology for pavement evaluations in Texas, USA. In *Fourth International Conference on Ground Penetrating Radar*, volume 1, pages 277–383, 1992. Author(s) with Highway Materials Division, Texas A& M University.

[9] Cariou J. Performance of a synthetic pulse ground penetrating radar in relation to impulse radars. In *54th Meeting of the European Association of Exploration Geophysicists*, volume 1, pages 440–441, 1992. Author(s) with CETE / SNCF / RATP.

[10] Daniels DJ. Radar techniques for the evaluation of masonry structures. In *54th Meeting of the European Association of Exploration Geophysicists*, volume 1, page 414, 1992. Author(s) with ERA Techology.

[11] Chignell RJ et al. Early developments in ground probing radar at ERA Technology Ltd. *IEE Proc. Pt.F*, 135(4):362–370, August 1988. Author(s) with ERA Technology.

[12] Ozdemir J et al. Imaging of shallow subsurface objects: An experimental observation. *IEEE Transactions on Geoscience and Remote Sensing*, GE-30(3):472–481, May 1992. Author(s) with University of Pennsylvania.

[13] Eberle AC and Young JD. Development and field testing of a new locator for buried plastic and metal utility lines. Technical Report 631, Transportation Research Board, National Academy of Science, Washington DC, 1977. Author(s) with Columbia Gas System Service Corp.

[14] Junrong Z et al. The development of sub-surface impulse imaging radar and its application. In *Fourth International Conference on Ground Penetrating Radar*, volume 1, pages 71–77, 1992. Author(s) with Changchun Institute of Geography, China.

[15] Michiguchi Y et al. Advanced subsurface radar system for imaging buried pipes. *IEEE Transactions on Geoscience and Remote Sensing*, GE-26(6):733–740, November 1988. Author(s) with Hitachi Ltd., Japan.

[16] Scott HF and Gunton DJ. Radar detection of buried pipes and cables. In *Proc. Institute of Gas Engineers 53rd Autumn Meeting*, volume Comm. No. 1345, pages 57–68, 1987. Author(s) with British Gas.

[17] Daniels DJ et al. Introduction to subsurface radar. *IEE Proc. Pt.F*, 135(4):278–320, August 1988. Author(s) with ERA Technology.

[18] Iizuka K and Freundorfer AP. Step frequency radar. *Journal of Applied Physics*, 56(9):2572–2583, November 1984. Author(s) with University of Toronto, Canada.

[19] Ybarra GA et al. Optimal signal processing of frequency-stepped cw radar data. *IEEE Transactions on Microwave Theory and Techniques*, 43(1):94–105, January 1995. Author(s) with Duke University, USA.

[20] Iizuka K and Freundorfer AP. Detection of non-metallic buried objects by a step frequency radar. *Proc. IEEE*, 71(2):276–278, February 1983. Author(s) with University of Toronto, Canada.

[21] Olver AD et al. Portable FMCW radar for locating buried pipes. In *Radar 82*, volume 1, pages 413–418. IEE Publ. No. 216, 1992. Author(s) with QMWC University of London.

[22] Botros AZ et al. Microwave detection of hidden objects in walls. *Electronics Letters*, 20:379–380, April 1984. Author(s) with QMWC University of London.

[23] Clarricoats PJB. Portable radar for the detection of buried objects. In *Radar '77*, volume 1, pages 547–551. IEE Publ. No. 155, 1977. Author(s) with QMWC University of London.

[24] Osumi N and Ueno K. Synthetic aperture approach to underground pulse-radar imaging. In Musha T et al., editor, *International Symposium on Noise and Clutter Rejection in Radars and Imaging Sensors (INSCR)*, volume 1, pages 667–672. IECE, 1984. Author(s) with Nippon Telegraph and Telephone, Japan.

[25] Yamaguchi Y et al. Synthetic aperture fm-cw radar applied to the detection of objects buried in snowpack. In *IEEE Transactions on Geoscience and Remote Sensing*, volume GE-32(1), pages 11–18, January 1994. Author(s) with Niigata University, Japan.

[26] Saarenketo T et al. GPR applications in geotechnical investigations of peat for road survey purposes. In *Fourth International Conference on Ground Penetrating Radar*, volume 1, pages 292–305, 1992. Author(s) with Finnish National Road Administration.

[27] Bohan Q and Yilin Q. An experimental underground radar for historical archaeology. In *IEEE Symposium on EMC*, volume 1, pages 359–361, 1985. Author(s) with Northwest Telecommunications Engineering Institute, Xi'an, China.

[28] Colombel JH. Pavement surveying with the LPC radar. In *54th Meeting of the European Association of Exploration Geophysicists*, volume 1, pages 446–447, 1992. Author(s) with CETE, France.

[29] Hopman V. Ground radar applications for road constructions. In *54th Meeting of the European Association of Exploration Geophysicists*, volume 1, pages 410–411, 1992. Author(s) with Delft Geotechnics, The Netherlands.

[30] Parry NS et al. Ground penetrating radar for roads and bridges: Strengths and limitations. In *54th Meeting of the European Association of Exploration Geophysicists*, volume 1, page 406, 1992. Author(s) with EBA Engineering Consultants Ltd., Canada.

[31] Parry NS et al. GPR systems for roads and bridges. In *Fourth International Conference on Ground Penetrating Radar*, volume 1, pages 247–257, 1992. Author(s) with EBA Engineering Consultants Ltd., Canada.

[32] Glover JM. Void detection using standing wave analysis. In Pilon J., editor, *Ground Penetrating Radar (Paper 90-4)*, volume 1, pages 63–73. Geological Survey of Canada, 1992. Author(s) with Subsurface Geotechnical Services.

[33] Ulriksen P. Multistatic radar system-mrs. In *Fourth International Conference on Ground Penetrating Radar*, volume 1, pages 57–62, 1992. Author(s) with Tekniska Högskolan, Lund, Sweden.

[34] Tsuchihashi H et al. A radar system for udergrounds pipe detection. In *Conference of the Committee International Regional Electricity Distribution (CIRED)*, volume 1, pages 247–251. IEE Publ. No. 305, 1989. Author(s) with Tokyo Electric.

[35] Kathage AF. A challenge: GPR in advance of horizontal drilling. In *Fourth International Conference on Ground Penetrating Radar*, volume 1, pages 119–124, 1992. Author(s) with Flow-Tex Service, Germany.

[36] Chignell RJ. A multi-channel surveying radar system. In *54th Meeting of the European Association of Exploration Geophysicists*, volume 1, pages 444–445, 1992. Author(s) with EMRAD.

[37] Weil GJ. Non-destructive testing of bridge, highway and airport pavements. In *Fourth International Conference on Ground Penetrating Radar*, volume 1, pages 259–266, 1992. Author(s) with Entech Engineering, USA.

[38] Hulsmeyer C. Patent No. 165546, 1904, German.

[39] Leimbach G. and Lowy H. Patent No. 237944, 1910, German.

[40] Lowy H. and Leimbach G. Patent No. 246836, 1910, German.

[41] Lowy H. Patent No. 254517, 1911, German.

[42] Raven E. Patent No. 331426, 1919, German.

[43] Leimbach G. Patent No. 273339, 1913, German.

[44] Raven E. Patent No. 331427, 1919, German.

[45] Gesellschalt fur drahtlose Telegraphie m.b.H, Patent No. 377187, 1920, German.

[46] 'Erda'A-G. Patent No. 404098, 1922, German.

[47] Konigsberger J. Patent No. 444506, 1922, German.

[48] 'Seismos' GmbH, Patent No. 458097, 1923, German.

[49] Hülsenbeck & Co. Patent No. 489434, 1926, German.

[50] Young JD and Caldecott R. Underground pipe detector. Patent No. 4 062 010 US 77, Ohio State University, USA.

Chapter 2

Literature Review

2.1 Outline

Several factors make ground penetrating radar more complicated than free-space radar. In order to design a successful GPR system which produces a reasonable result in an acceptable time, the modelling method appears to be the most effective way to do it, which uses computer software to simulate the GPR system work, predicate how the underground topology is presented and how the system will react to the realistic targets, therefore optimizing the GPR system. This chapter provides an overview of the literature search about the modelling of GPR systems, ray tracing methods, FMCW radar signal processing and image processing. The chapter also gives the conclusion on the literature search.

2.2 Modelling of GPR System

2.2.1 Ray Tracing Algorithm

From Snell's law, the ray tracing algorithm indicates that any electromagnetic wave or light wave will produce a reflection and a refraction at the surface between two media

with different dielectric constant. Ray tracing methods can be used in modelling the propagation of GPR to simulate the reflections and refractions in the path to and from a target. Several papers [1] [2] reported using ray tracing methods to model GPR systems.

Goodman [1] used an exact ray tracing technique to produce a 2-D forward modelling package to simulate ground penetrating radar. The software can predict the full waveform signatures for a variety of different ground conditions and structures. Some simulation results were given.

In Cai's paper [2] a ray-based algorithm for synthesizing bistatic GPR profiles was described and applied to the modelling of a multi-offset, multi-frequency data set from fractured carbonates. The program generates reflections from complicated geometrical features by explicit computation of source and receiver directivity, reflection and transmission coefficients, 3-D geometrical spreading, and attenuation. The modelling results concentrate on the geologic environment.

From the literature review, ray tracing was shown to be a suitable method to model the FMCW radar system in this project.

2.2.2 Finite-Difference Time-Domain

In recent years, time-domain electromagnetic methods have attracted an increasing amount of attention. Geophysical prospecting, remote sensing of objects and people, nondestructive testing, and ground penetrating radar are the areas which benefit from transient electromagnetic methods.

In Moghaddam's [3] paper, the FDTD(Finite-Difference Time-Domain) method is used to solve the $2\frac{1}{2}$D problem of the response of an arbitrary source, in particular a point source of an impulse signal, in a two-dimensional isotropic inhomogeneous medium. The analysis of a single line source component using 225 time steps requires 7 minutes on a SUN-SPARC workstation, with a point source example requires about 6.5 hours. Some more complicated practical cases such as locating reinforcing bar or a void have also been demonstrated by this numerical model.

The FDTD 2D+ method has been reported by Livelybrooks [4] who developed a

user-interface for Moghaddam's program. Program FDTD 2D+ has been used to simulate reverberation of radar waves within a mine tunnel in an effort to discriminate reverberations from reflections from interesting targets. This program ran on a SUN workstation in tens to hundreds of minutes, depending upon the number of nodes and the number of wave numbers for which solutions are calculated. A user-interface has been included in the program.

Wang [5] also developed a FDTD solution to Maxwell's equations for simulating electromagnetic wave propagation in three-dimensional media. The algorithm allows arbitrary variations of electrical conductivity and permittivity to be used in the model. On a Cray C-90 computer, the run time is about 6 CPU minutes for each source position for a 3-D model. The results show that the FDTD solution generally agrees well with closed-form solutions.

Although FDTD method has reported for modelling GPR propagation and produced good simulation results, the long program execution times are the big shortcoming for real time application, and also the FDTD method needs to simulate cases for many positions, each needing complete simulation, therefore it was considered unsuitable for this project.

2.3 FMCW Radar Signal Processing

The application of FMCW radar to locate underground objects has attracted a growing interest because of its high resolution, wide dynamic range and short distance characteristics.

Olver and others at Queen Mary and Westfield College of the University of London (QMWC) have published work concerning FMCW systems incorporating basic microprocessor control of the frequency sweep linearity and digital signal processing techniques [6], [7]. They developed a FMCW radar which used three different frequency bands: 1—2GHz, 2—4GHz and 9—11GHz. Each of these bands suits a particular application type.

In [6], Olver *et al* described a FMCW radar which worked in the 1—2GHz band. The

signal repetition rate was 10Hz and the sweep time was about 10 ms. The antenna was 600mm in diameter. Tests were described which detected a 150mm diameter ceramic pipe buried 1.0m below surface. The result was a one dimensional return signal spectrum which need a trained operator to interpret.

The 9—11GHz FMCW radar [7] had been used to detect voids and non-metallic hidden objects with a smaller hand held unit. The results shown presented the comparison between the spectrum of the response to a plastic pipe and a metal bar, together with the 2D scan plots. These clearly show the difference between the images from a plastic pipe and a metal plate.

In Carr *et al* [8], a method of digital signal processing for extracting and isolating targets in the return signal of an FMCW radar was described. The work applied digital filtering to the frequency difference spectrum, followed by non-linear optimisation to detect the presence of multiple targets amid clutter. The results show that the method gives enhanced detection of weak return signals. But in this paper it can only spot targets on the spectrum of radar return signal rather than give the accurate target depth reading.

Yamaguchi [9] reported his work on a practical FMCW radar for detecting objects buried in wet snowpack. The operating frequency of this FMCW radar was from 1.2—2.2GHz with a maximum output power of 100 mW. An averaging and subtracting digital signal processing technique was employed. A laboratory simulation and two field experiments were carried out to detect and map various objects embedded in the snowpack. Results show that this system could map metallic objects larger than 5 cm wide buried at 80 cm depth. Yamagichi [10] also published another paper which described work into detecting human bodies in snowpack using an FMCW radar. Results show it was possible to map body buried at least 125 cm from the snow surface.

2.4 Filtering Process

Ground Penetrating Radar return signals contain noise and clutter, in order to extract a target signal from this background, some basic methods [11] are: averaging which re-

duces random noise but has no effect on clutter; subtraction which can reduce clutter if the statics of the ground are position-independent; time-varying gain which makes most effective use of the dynamic range of the data presentation medium; frequency filtering which uses lowpass, highpass and bandpass filters that are provided in some commercially available equipment. Except the above techniques, some other more advanced techniques [11], such as waveform-dependent methods and target-dependent methods enable the detection of received signal corresponding to a target much more effective.

Wiener filtering is an obvious waveform-dependent method which has the transfer function as Equation 2.1 [11]

$$H(\omega) = \frac{S^*(\omega)}{N_0/2 + K_c|S(\omega)|^2} \tag{2.1}$$

where N_0 is the noise power, $S(\omega)$ is the signal spectrum and $K_c|S(\omega)|^2$ is the clutter power. An important special case of the Wiener filter is the matched filter when noise dominates, when clutter dominates it becomes the inverse filter.

Ueno and Osumi [12] have adapted this approach in designing a filter for their subsurface radar data as part of a holographic imaging procedure. They multiplied $H(\omega)$ by a linear combination of multipliers and delays(a transversal filter) to obtain an output which had, when a know reference was used as input, an acceptable combination of mainlobe width and sidelobe levels.

Carr *et al* [8] tried to use matched filter on a FMCW radar return signal, but the results were poor, the resolution appeared to deteriorate.

2.5 Synthetic Aperture

The technique of coherent processing of several received radar signals has been used to enable the narrow beamwidth of wide aperture antennas to be synthesised by combining the measurements obtained from a number of wider beamwidth antennas arranged in an array. This kind of radar is so-called synthetic aperture radar which has high angular resolution.

Early synthetic aperture systems used optical techniques and storage of information on photographic film. More recently, Anderson and Coworkers have used single-frequency CW radiation to demonstrate true microwave holography applied to the imaging of buried objects [13] [14] [15] [16]. The technique has also been used for ice surveying [17].

The synthetic aperture and holographic process requires the measurement over an aperture at the ground surface of the amplitude and phase of reflected signals from a target, making use of the direct illumination of the receiver from the source to provide a phase reference. For underground targets, the synthetic aperture process also requires a knowledge of the refractive index of soil.

Several papers have reported the imaging techniques for processing GPR data. Image reconstruction principles based on microwave holography are treated in [18] [19] which use a computer-aided imaging method incorporating a wide-band holographic approach in pulse radar systems.

Michiguchi [20] introduced new imaging processing techniques for impulse band GPR. This takes two steps to produce a high resolution image: preprocessing and then synthetic aperture processing.

Synthetic aperture techniques have been successful employed using pulse radar systems for high resolution area mapping [21] [22] [23] [17] [16] [24] [25]. However, for locating a shallow target, the pulse radar has difficulty in achieving the high precision needed in the time domain. On the contrary, FMCW radar is very suitable for short distance applications. Yamaguchi [26] has published work using a synthetic aperture technique with an FMCW radar. In this, the principle of synthetic aperture FMCW radar was presented and results of several objects buried in natural snowpack by using this radar system was provided. The results show a high resolution image in the azimuth direction comparing with real aperture images, but for producing the high resolution image, a number of tests have to be done to obtain the underground refractive index value before the scan test.

2.6 Conclusion

From the literature search, most of the methods concerning the modelling of GPR are theoretical models. The FDTD method is not suitable for the processing requirements of this project, not only because of the computer memory requirements, but also the long execution times. Ray tracing methods were found to be suitable for establishing target path models.

The non-linear optimisation algorithm reported in QMWC's paper [8] cannot be adapted because it did not give the accurate target depth reading. Also this method took some time to run which presents a restriction on its use in the practical system.

Matched filter, clutter rejection filter and synthetic aperture algorithms for FMCW radar techniques were examined in this work to see what results will be produced by this method.

Considering the aims of this research, the need was for real-time processing which produce fast and easy to understand software output. The signal processing task was to establish a simulation model to perform the basic target analysis algorithm firstly, and then use this algorithm on the real measured data. This naturally led to an investigation of other methods to improve system resolution and produce software for practical use.

References

[1] Goodman D et al. Gprsim forward modeling software and time slides in ground penetrating radar surveys. In *Fifth International Conference on Ground Penetrating Radar*, volume 1, pages 31–43, 1994. Author(s) with Geophysical Archaeometry Laboratory, Japan.

[2] Cai Jun et al. Ray-based synthesis of bistatic ground penetrating radar profiles. In *Fifth International Conference on Ground Penetrating Radar*, volume 1, pages 19–29, 1994. Author(s) with University of Texas, USA.

[3] Moghaddam M et al. Modelling of the subsurface interface radar. *Journal of Electromagnetic Waves and Applications*, 5(1):17–39, January 1991. Author(s) with University of Illinois at Urbana-Champaign, USA.

[4] Livelybrooks D et al. Fdtd2d+ a finite-difference, time-domain radar modelling program for two dimensional structures. In *Fifth International Conference on Ground Penetrating Radar*, volume 1, pages 87–100, 1994. Author(s) with Ecole Polytechnique, Canada.

[5] Wang T et al. Simulation of electromagnetic wave propagation in three-dimensional media by an fdtd method. In *Fifth International Conference on Ground Penetrating Radar*, volume 1, pages 247–267, 1994. Author(s) with University of Utah, USA.

[6] Olver AD et al. Portable FMCW radar for locating buried pipes. In *Radar 82*, volume 1, pages 413–418. IEE Publ. No. 216, 1992. Author(s) with QMWC University of London.

[7] Olver AD and Cuthbert LG. FMCW radar for hidden object detection. *IEE Proc. Pt.F*, 135(4):354–361, August 1988. Author(s) with QMWC University of London.

[8] Carr AE et al. Digital signal processing for target detection in FMCW radar. *IEE Proceedings Part F*, 128(5):331–336, October 1981. Author(s) with QMWC University of London.

[9] Yamaguchi Y et al. Detection of objects in wet snowpack by an FMCW radar. *IEEE Transactions on Geoscience and Remote Sensing*, GE-29(2):201–208, March 1991. Author(s) with University of Niigata, Japan.

[10] Yamaguchi Y et al. Human body detection in wet snowpack by an FMCW radar. *IEEE Transactions on Geoscience and Remote Sensing*, GE-30(1):186–189, January 1992. Author(s) with University of Niigata, Japan.

[11] Daniels DJ et al. Introduction to subsurface radar. *IEE Proc. Pt.F*, 135(4):278–320, August 1988. Author(s) with ERA Technology.

[12] Osumi N and Ueno K. Microwave holographic imaging method with improved resolution. *IEEE Transactions on Antennas and Propagation*, AP-32(2):1018–1026, February 1984. Author(s) with Nippon Telegraph and Telephone, Japan.

[13] Richards PJ and Anderson AP. Microwave images of sub-surface utilities in an urban environment. In *8th Conference of the European Microwave*, volume 1, pages 33–37, 1978.

[14] Anderson AP. Micerwave holography. In *Proc. IEE*, volume 124, pages 946–962, 1977.

[15] Orme RD and Anderson AP. High-resolution microwave holographic technique: application to the imageing of objects obscured by dielectric media. In *Proc. IEE*, volume 120, pages 401–406, 1973.

[16] Junkin G and Anderson AP. A new system for microwave holographic imaging of buried services. In *16th European Microwave Conference, Dublin*, volume 2, pages 720–725, 1986. Author(s) with University of Sheffield.

[17] Junkin G and Anderson AP. Limitations in microwave holographic synthetic aperture imaging over a lossy half space. *IEE Proc. Pt.F*, 135(4):321–329, August 1988. Author(s) with University of Sheffield.

[18] Osumi N and Ueno K. Detection of buried plant. *IEE Proc. Pt.F*, 135(4):330–342, August 1988. Author(s) with Nippon Telegraph and Telephone, Japan.

[19] Osumi N and Ueno K. Microwave holographic imaging of underground objects. *IEEE Transactions on Antennas and Propagation*, AP-33(2):152–159, February 1985. Author(s) with Nippon Telegraph and Telephone, Japan.

[20] Michiguchi Y et al. Development of signal processing methods for imaging buried pipes. *IEEE Transactions on Geoscience and Remote Sensing*, GE-25(1):11–15, January 1987. Author(s) with Hitachi Ltd., Japan.

[21] Fitch JP, editor. *Synthetic Aperture Radar.* Berlin: Springer-Verlag, 1988.

[22] Mensa DL, editor. *High Resolution Radar Imaging.* Dedham, Mass: Artech House, c1981.

[23] Osumi N and Ueno K. Synthetic aperture approach to underground pulse-radar imaging. In Musha T et al., editor, *International Symposium on Noise and Clutter Rejection in Radars and Imaging Sensors (INSCR)*, volume 1, pages 667–672. IECE, 1984. Author(s) with Nippon Telegraph and Telephone, Japan.

[24] Michiguchi Y et al. Advanced subsurface radar system for imaging buried pipes. *IEEE Transactions on Geoscience and Remote Sensing*, GE-26(6):733–740, November 1988. Author(s) with Hitachi Ltd., Japan.

[25] Michiguchi Y et al. A subsurface radar for imaging buried structures. In *IEEE International Geoscience and Remote Sensing Symposium (IGARSS)*, volume 1, pages 1667–1671, 1988. Author(s) with Hitachi Ltd., Japan.

[26] Yamaguchi Y et al. Synthetic aperture fmcw radar applied to the detection of objects buried in snowpack. In *IEEE Transactions on Geoscience and Remote Sensing*, volume GE-32(1), pages 11–18, January 1994. Author(s) with Niigata University, Japan.

Chapter 3

Principles of FMCW Radar Operation

3.1 Outline

This chapter describes the principles of FMCW radar operation, signal processing and the FMCW system model aims and structure. The chapter also gives the target simulation mathematical model which uses the ray tracing method to evaluate the target path in different infill media.

3.2 FMCW Radar Operation

A basic FMCW radar system [1] is shown in Figure 3.1. The system is composed of a frequency generator, transmitter and receiver antennas, a receiver mixer and signal processing hardware. The frequency generator, typically a Voltage Controlled Oscillator(VCO), produces the transmitted signal whose frequency is swept linearly with time. The VCO output signal is connected to the transmitter amplifiers and antennas. The reference signal is extracted from the VCO and coupled to the receiver mixer to demodulate the received signal. The radar return signal is mixed in the receiver mixer

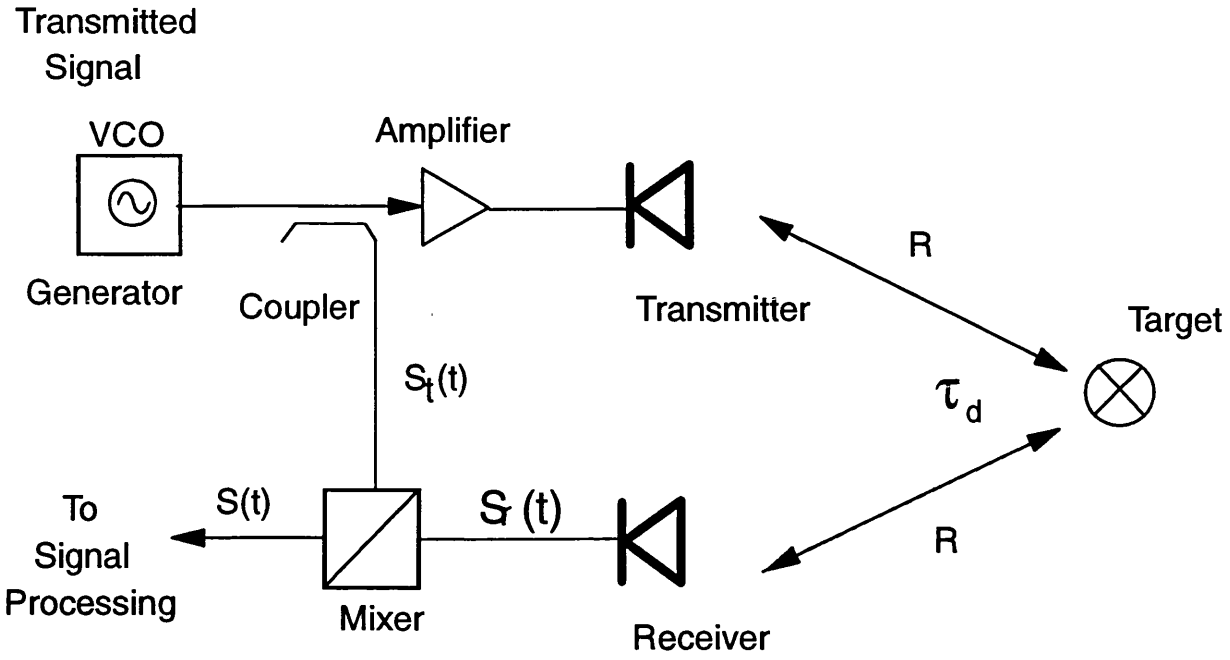

Figure 3.1: Basic Elements of an FMCW Radar System

to produce an audio-band beat frequency, which is proportional to the signal propagation time to and from the target. The audio-band signal is sampled and transformed into the frequency domain. The signal processing subsystem analyses this spectrum to determine the target distance.

An FMCW radar transmits a carrier wave which is linearly swept in frequency between a lower frequency, f_0, and an upper frequency, $f_0 + \Delta f$, during a time, T_s. This is repeated at a repetition rate, T_r, as shown in Figure 3.2. The time difference between transmitted signal and received signal is denoted by τ_d. Assuming that there is only one target at a distance R from the radar antenna, then the return signal will be delayed in time by ($\tau_d = \frac{2R}{v}$) where v is the velocity of propagation in the media.

The transmitted frequency f_t can be written in terms of a base frequency, f_0 and the rate of change of frequency with time:

$$f_t = f_0 + \frac{df}{dt}t = f_0 + \frac{\Delta f}{T_s}t \tag{3.1}$$

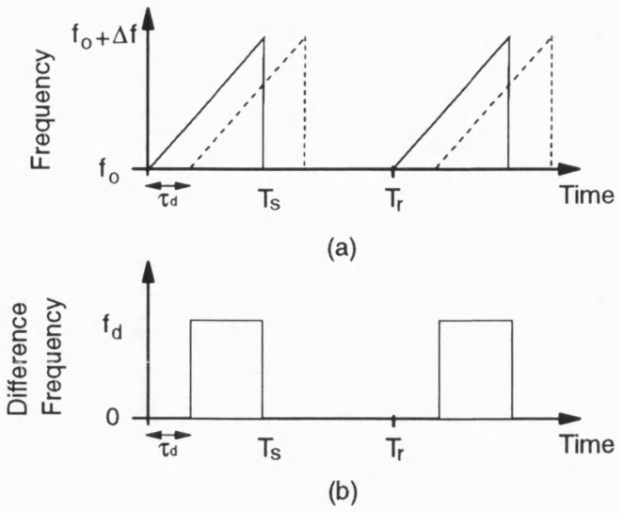

Figure 3.2: (a) Transmitted (—) and received (- - -) frequency profiles in an FMCW Radar System; (b) Difference frequency between profiles proportional to delay in 'echo' of signal, and hence depth of target

The delayed radar return signal, f_r, is therefore given by:

$$f_r = f_0 + \frac{\Delta f}{T_s}(t - \tau_d) \tag{3.2}$$

with the difference frequency, f_d, :

$$f_d = f_t - f_r = \tau_d \left(\frac{\Delta f}{T_s}\right) = \frac{2R}{v}\left(\frac{\Delta f}{T_s}\right) \tag{3.3}$$

the above equation shows that the difference frequency, f_d, is proportional to the target distance R.

The repetition rate (T_r) has a considerable effect on the received signal spectrum. If the signal is swept only once, the return signal is a single sinewave burst at the difference frequency. This signal is illustrated in Figure 3.3(a) along with its frequency spectrum in Figure 3.3(b). The fact that the signal has a finite duration results in it having a spectrum rather than being a single tone. The spectrum peaks at the difference frequency, giving a clear indication of the propagation time of the signal.

Repeatedly sweeping the signal with a fixed delay between sweeps, transforms the

smooth frequency spectrum into one which is sampled at the harmonics of the repetition frequency, as shown in Figure 3.4(a),(b). The return spectrum is then not a continuous, smooth trace, but a set of spectral lines. If the delay between sweeps is too short, the spectrum becomes as shown in Figure 3.5. The spectral lines become too separated in frequency to give a clear indication of the spectral peak, and hence signal propagation time.

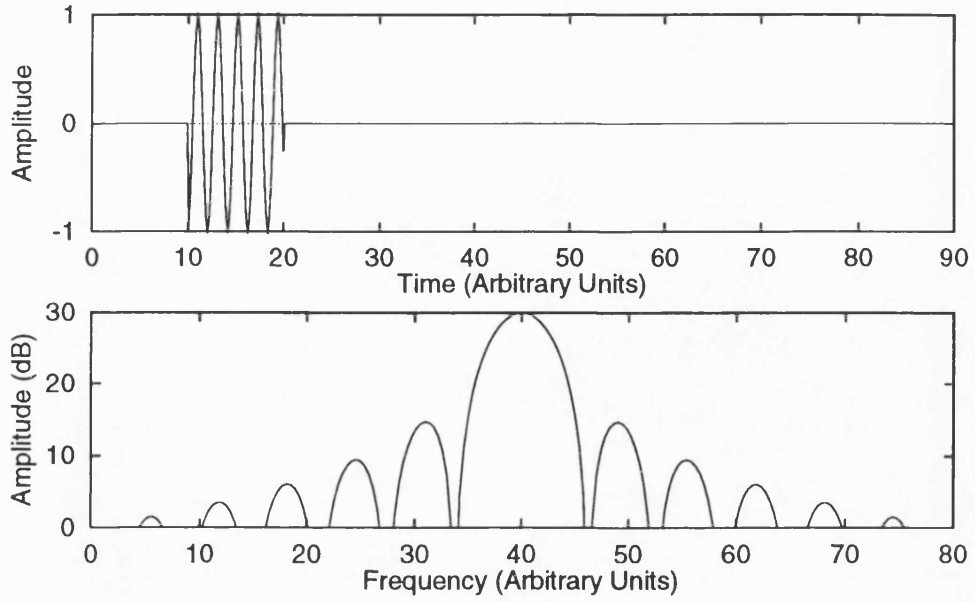

Figure 3.3: a) Return signal, and b) Frequency spectrum, of a single sweep of an FMCW radar system

3.3 Modulation of the FMCW Waveform

Recalling from Equation 3.1 the instantaneous transmitted frequency, $f_t(t)$, can be represented by:

$$f_t(t) = f_0 + \frac{\Delta f}{T_s} t \tag{3.4}$$

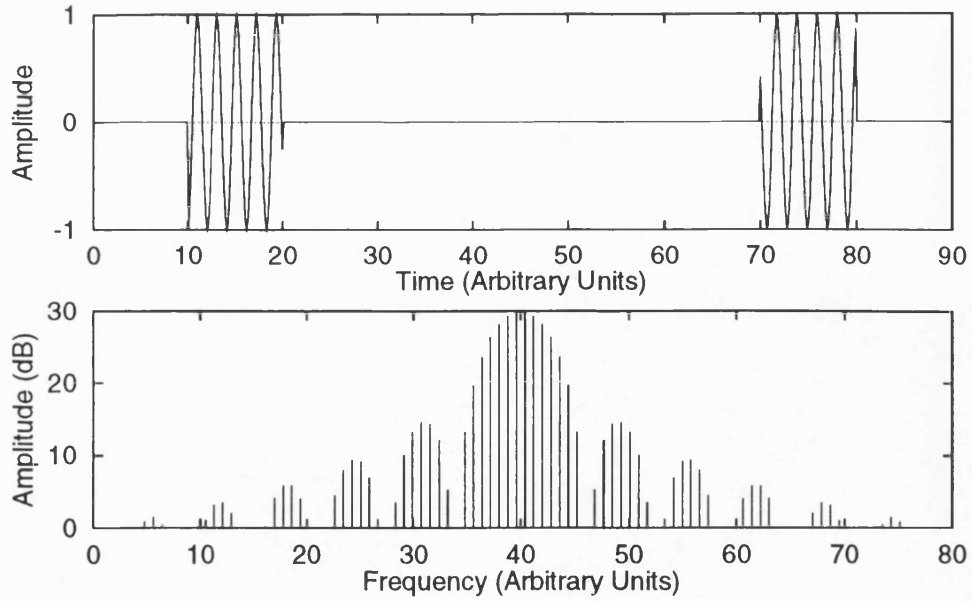

Figure 3.4: a) Return signal, and b) Frequency spectrum, of a repetitive sweep of an FMCW radar system

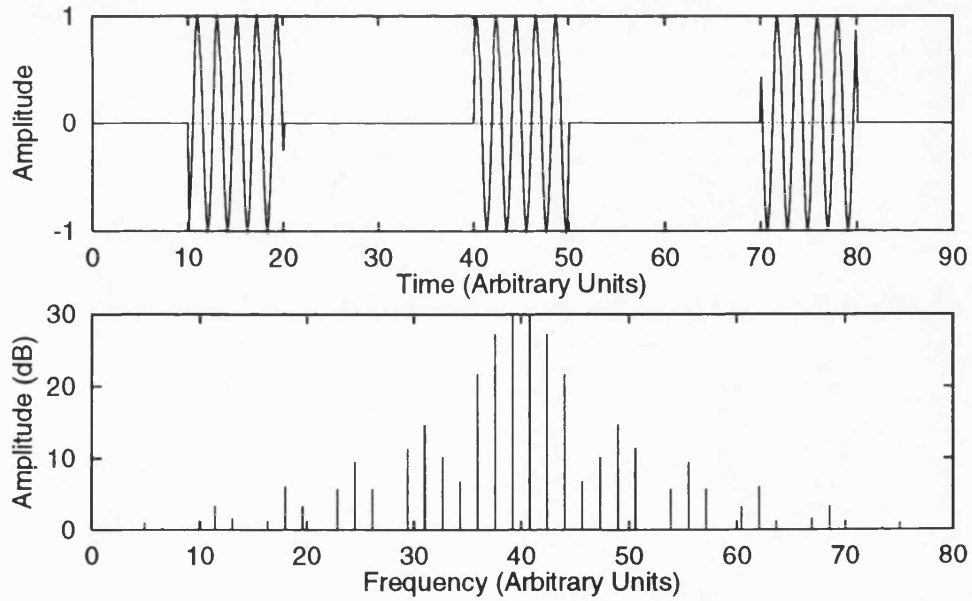

Figure 3.5: a) Return signal, and b) Frequency spectrum, of a repetitive sweep of the FMCW radar system. Repetition frequency is twice that of Fig.3.4

denoting the instantaneous transmitted angular frequency by $\omega_t(t)$ for $0 < t < T_r$:

$$\omega_t(t) = \begin{cases} 2\pi f_t(t) & 0 < t < T_s \\ 0 & T_s \leq t < T_r \end{cases} \tag{3.5}$$

the transmitted signal waveform can be represented as the integral of the instantaneous frequency [2]:

$$S_t(t) = A_t \cos \int \frac{d\phi}{dt} dt = A_t \cos \int_0^{T_s} \omega_t(t) dt \tag{3.6}$$

Where A_t is the amplitude of transmitted signal. Substituting $\omega_t(t)$ with Equation 3.4 and 3.5, gives the transmitted signal as:

$$S_t(t) = A_t \cos \left(2\pi f_0 t + 2\pi \frac{\Delta f}{T_s} \frac{t^2}{2} \right) \tag{3.7}$$

3.4 Demodulation of the FMCW Waveform

The receiver signal is the transmitter signal delayed by τ_d:

$$S_r(t) = A_r \cos \left(2\pi f_0 (t - \tau_d) + 2\pi \frac{\Delta f}{T_s} \frac{(t - \tau_d)^2}{2} \right) \tag{3.8}$$

A_r is the amplitude of receiver signal. The receiver mixer output is hence defined by:

$$\begin{aligned} S(t) &= S_t(t) S_r(t) \\ &= \frac{1}{2} A_t A_r \cos \left(4\pi f_0 t - 2\pi f_0 \tau_d + \frac{2\pi \Delta f}{T_s} t^2 - \frac{2\pi \Delta f \tau_d}{T_s} t + \frac{\pi \Delta f \tau_d^2}{T_s} \right) \\ &\quad + \frac{1}{2} A_t A_r \cos \left(2\pi f_0 \tau_d + \frac{2\pi \Delta f \tau_d}{T_s} t - \frac{\pi \Delta f \tau_d^2}{T_s} \right) \end{aligned} \tag{3.9}$$

Let $B = \frac{1}{2} A_t A_r$ and let the receiver output be low pass filtered to produce the baseband frequency difference signal:

$$S(t) = B \cos \left(2\pi f_0 \tau_d + \frac{2\pi \Delta f \tau_d}{T_s} t - \frac{\pi \Delta f \tau_d^2}{T_s} \right) \tag{3.10}$$

In typical use the condition $\frac{\pi \Delta f {\tau_d}^2}{T_s} \ll 2\pi f_0 \tau_d$ holds, and the receiver mixer signal

becomes

$$S(t) = B\cos\left(2\pi f_0\tau_d + \frac{2\pi\Delta f\tau_d}{T_s}t\right) \tag{3.11}$$

Here $2\pi f_0\tau_d$ is a phase term and the signal frequency is $\frac{\Delta f\tau_d}{T_s}$.

3.5 5 head FMCW system

A two transmitter and three receiver FMCW radar (Figure 3.6) has been proposed to facilitate accurate measurement of the depth of a buried object. This system contains two transmitter heads T_A, T_B, and three receiver heads $R_{A/B}$, R'_A and R'_B while $R_{A/B}$ is switchable receiver. As seen in Figure 3.6, there are four propagation paths: from T_A to R_A, T_B to R_B, T_A to R'_A and T_B to R'_B. When the target is directly beneath the measurement unit, the propagation path T_A to R_A will equal that from T_B to R_B and T_A to R'_A will equal T_B to R'_B. If the target is off unit centerline, the two pairs of propagation paths will be unequal. In the convolution technique described later in Chapter 4, Section 4.4, This enables the system to concentrate the measurement onto the target direct beneath the unit and filter the off line target. Using the ratio of the time delays in the two propagation paths we can calculate the target safe digging depth and avoid needing to know the refractive index of the soil, as described in Chapter 4, Section 4.5.

The UHF electronic sub-system provides the transmitted signal, and receives the reflected signal from the target to provide the input to the signal processing sub-system. The transmitted power is increased with frequency in order to reduce the dynamic range requirements of the signal processing system by compensating for the attenuation characteristics of the infill. The mixer decodes the received signals and provide the data for the signal processing stage.

The signal processing and system control sub-system inputs the data from a UHF scan and stores this in memory. Data from different scan pairs are then convolved to concentrate the measurements onto targets directly below the center of the measurement unit. The data from this stage is used to determine whether the unit is positioned directly over a significant target and then to compute its depth. The sub-system provides

an left or right arrow indicating facility in order to center the unit over the target, once centered the unit displays the safe digging depth.

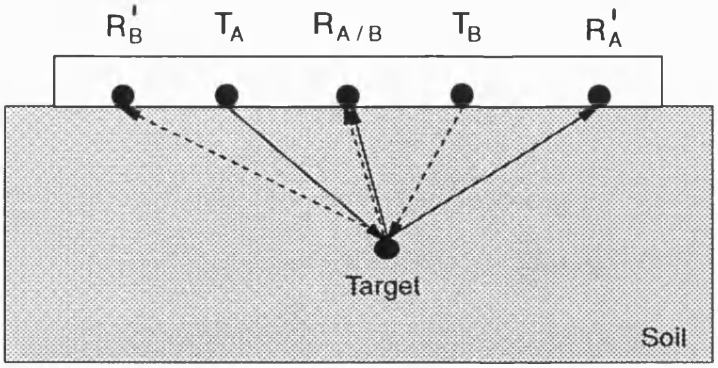

Figure 3.6: Array of transmitter and receiver heads used to measure the Safe Digging Depth of a target

3.6 FMCW System Model Aims and Structure

3.6.1 Aims of the Signal Processing Mathematical Model

Mathematical modelling of the FMCW radar has been developed to provide some prediction of how the system will react to realistic situations and to provide a reference for concerning field. The model simulates the UHF system and processes the signal spectrum, and finally gives the target depth measurement.

The signal processing system performs the following tasks:

- Generates the FM form of the transmitted signal.
- Calculates the propagation characteristics of the infill from the radar equation and the reflected signal from the target.
- Mixes the transmitter reference signal with the received signal.
- Filters the post-mixer signal.

- Samples audio-band frequency difference signal.
- Fourier transforms the data collected to determine its frequency spectrum.
- Convolves data from separate receiver channels to:
  - Provide an indication whether the unit should be moved left or right.
  - Concentrate system on targets directly under the center of the device.
  - Eliminate the unknown refractive index of the soil.
- Determines the safe digging depth and displays this to the operator.

In this chapter, the modelling of the signal propagation process is described. The modelling of the Target Analysis processes are described in Chapter 4. The signal processing model has two main aims. First is the prediction of how the transmitted signal profile affects the audio-band frequency difference spectrum and the effects of the convolution process on the output data. Second is the evaluation of various target analysis strategies used to compute the safe digging depth and unit movement. The model has been applied to a number of representative target situations.

3.6.2 Structure of the Mathematical Model

The signal processing model has been essentially divided into two main areas. The model outline is shown in Fig 3.7. The radar system and target simulation software models the UHF electronics sub-system and the signal propagation through the ground. The output from the software is a sampled form of the frequency difference signal produced by a number of user defined targets present in the soil.

The target analysis software computes the Fast Fourier Transform (FFT) of the sampled data. From this it calculates the movement direction of the unit to position it directly over the target and then calculates the safe digging depth.

The software has been written in the Microsoft QuickBasic computer language. The target simulation model and target analysis model have been programmed independently, using data files for the data input and output. In the experimental system, the

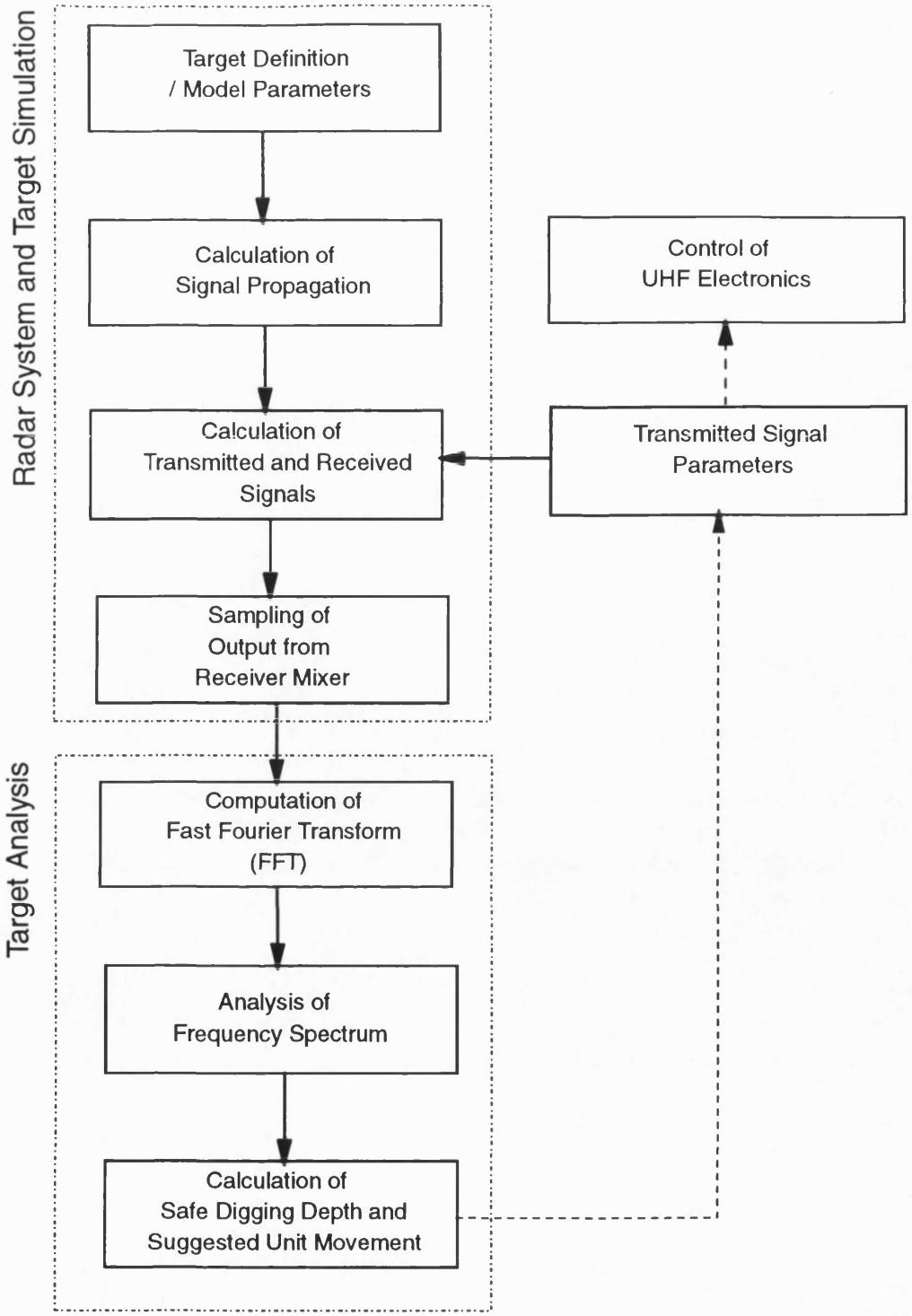

Figure 3.7: Sub-division of the Signal Processing Mathematical Model into Radar System and Target Simulation; and Target Analysis Modules

target analysis software will be used to process and analyse the sampled time domain signal produced from the UHF system.

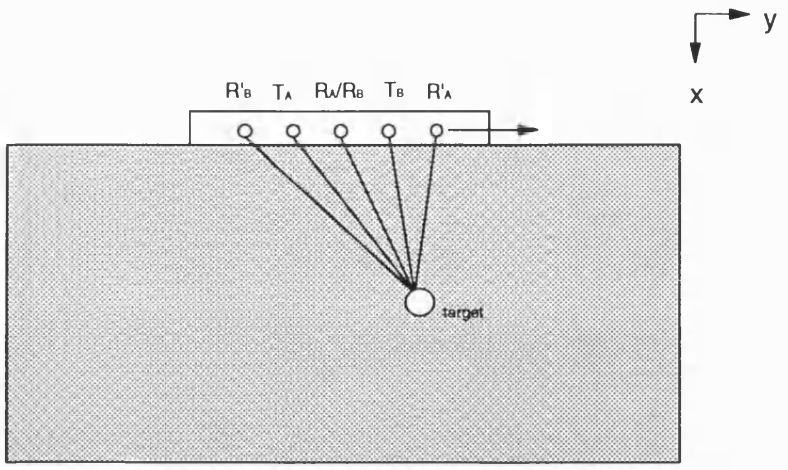

Figure 3.8: Cross Section of the Target Simulation Model

3.7 Target Simulation Model

The target simulation model uses the rectangular coordinates x,y as shown in Figure 3.8. The x=0 axis represents the ground level. The measurement unit can be moved along the y axis from left to right. The vertical axis represents the target's depth. The targets can be defined at various(x,y) positions with respect to the origin. The target size is also specified in terms of its radar cross section.

The target simulation model simulates the FMCW transmitted signals, their propagation though the soil and the reception and demodulation of signals. The model generates an output waveform(transmitted signal) and delays this by a time period related to the target depth(received signal). These signals are then mixed and sampled, and saved in data files for the target analysis model to use. The transmitted waveform can be programmed with a particular frequency and amplitude profile and so can explore various modulation and signal processing strategies that could be adopted. The propagation model through the soil is based on the radar equation and includes the soil's attenuation, transmitter and receiver antenna gains, target radar cross section,

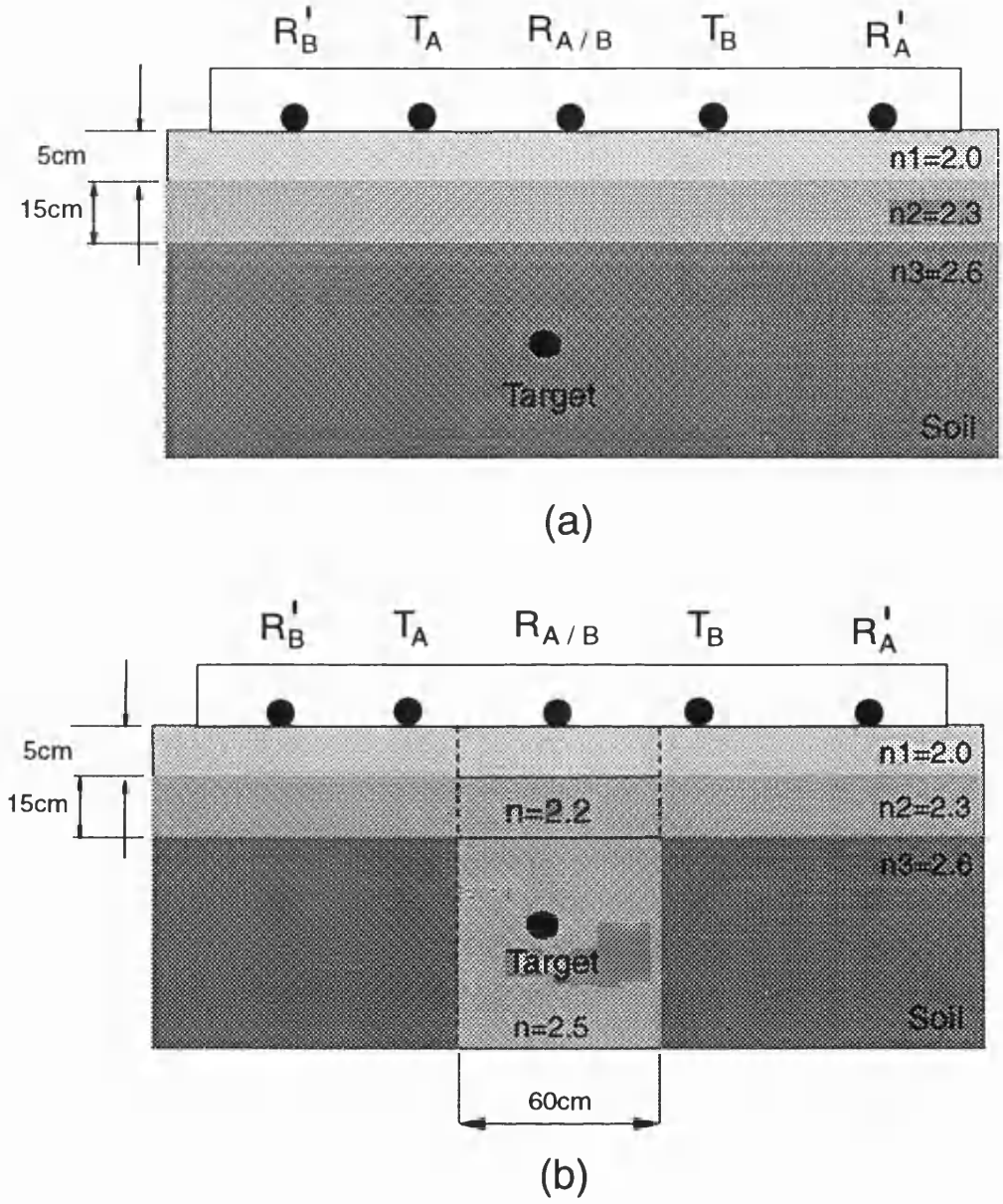

Figure 3.9: a) Layered b) Trenched infill profiles used in the target simulations

and the standard propagation losses resulting from beam spread.

The target simulation model can be specified with either: uniform, layered, or trenched infill profiles as shown in Figure 3.9. The refractive index values have been based on the results of the measurement on soil samples in the feasibility study [3]. The real part of the refractive index n' varies from 2.0 to 3.0, and the imaginary part of the refractive index n'' varies from 0.15 to 0.22.

3.7.1 Signal Propagation Model

The Radar equation [4] has been used to calculate the amplitude of radar return signals in the target simulation model and is shown below:

$$P_r = \frac{P_t G_t G_r \lambda^2 \sigma}{(4\pi)^3 r_1^2 r_2^2} L_p \tag{3.12}$$

Where the parameters are defined below:

- G_t: transmitter antenna gain
- G_r: receiver antenna gain
- λ: instantaneous wavelength of the transmitted waveform
- r_1: distance from transmitter to target
- r_2: distance from target to receiver
- σ: Radar Cross Section of the target
- P_t: transmitter power
- P_r: receiver power
- L_p: path propagation loss due to media attenuation

The transmitted signal frequency is varying with time as expressed in Equation 3.4, hence the wavelength can be written as:

$$\lambda_t(t) = \frac{c}{f_t(t)}$$

The radar cross section σ is calculated by the following formula:

$$\sigma = \Gamma T_d^2$$

Where T_d represents target's diameter, Γ is reflection coefficient, for metal object $\Gamma = 1.0$, non-metal object $\Gamma < 1.0$. The propagation of a plane wave along a direction, $(r_1 + r_2)$, in a medium with refractive index, n, is usually described by a complex exponential:

$$A\exp(j(\omega t - nk_0(r_1 + r_2))$$

where A is the wave amplitude, ω the angular frequency, and $k_0 = \frac{\omega}{c} = 2\pi f/c$ is the free space propagation wavenumber. c is the speed of light in vacuum 3×10^8 m/sec. In a general medium the refractive index is a complex quantity $n = n' - jn''$, so the propagation term becomes:

$$A\exp(j(\omega t - (n' - jn'')k_0(r_1 + r_2))) = A\exp(-n''k_0(r_1 + r_2))\exp(j(\omega t - n'k_0(r_1 + r_2)))$$

Hence the real part of the index, n', affects the phase change per unit length or wavelength of the propagating wave. The imaginary part of the index, n'', gives rise to an exponential attenuation of the wave amplitude. k_0 is a function of frequency, $k_0 = \omega/c = 2\pi f/c$, then the attenuation in propagation is:

$$L_p = A\exp(-2n''\frac{2\pi f_t(t)}{c}(r_1 + r_2))$$

In order to compensate the infill attenuation, the transmitted power can be increased with frequency, to maintain a constant receiver power. The transmitted power is changed with frequency as:

$$P_t(t) = 10\log\left(\frac{(f(t)^2}{c^2}\right) - 10\log(L_p)(dB) \tag{3.13}$$

then the receiver power will be a constant as below:

$$P_r = \frac{10^{\frac{P(t)}{10}}G_tG_r\lambda^2\sigma}{(4\pi)^3r_1^2r_2^2}L_p = \frac{G_tG_r\sigma}{(4\pi)^2r_1^2r_2^2} = Constant \tag{3.14}$$

The received signal amplitude is related with received power:

$$A_r = a_0\sqrt{P_r}$$

Where a_0 is a conversion constant. The transmitted power $P_t(t)$ compensates for the infill loss L_p so that the received power P_r will be a constant, as well as the received signal amplitude A_r.

3.7.2 Propagation Path within Infill Media

The mathematical model has been formulated to simulate uniform, layered or trenched infill as shown in Figure 3.9. A ray tracing algorithm has been used to calculate the distance from target to transmitter or receiver. A plane wave incident on the interface will be split into two waves: a refracted wave proceeding into the second medium and a reflected wave propagating back into the first medium. Suppose n_1, n_2, are the refractive index in the first and second medium. θ_i, θ_r, θ_t are the incident, reflected and refracted angles respectively. Snell's law [5] says n_1, n_2, θ_i and θ_t must have the following property:

$$\frac{\sin\theta_i}{\sin\theta_t} = \frac{n_2}{n_1}$$

Uniform Infill

Uniform infill as shown in Figure 3.10 is the ideal infill condition with a homogeneous dielectric constant. The target distance is therefore easily calculated using the following formula:

$$d = \sqrt{(x_{un} - x_{ta})^2 + (y_{un} - y_{ta})^2}$$

x_{ta}, y_{ta}: target position

x_{un}, y_{un}: transmitter/receiver position

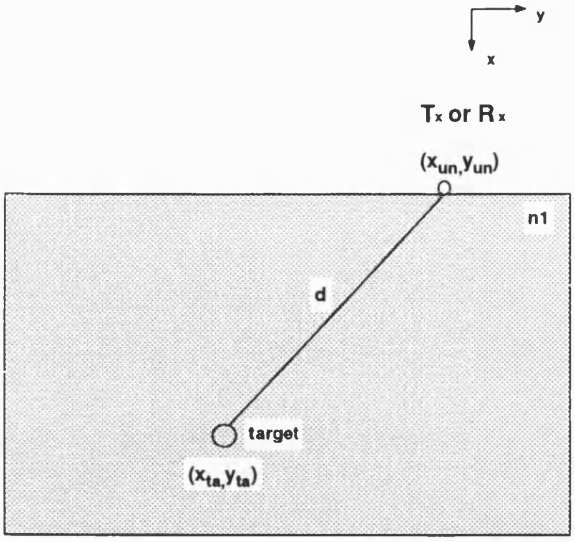

Figure 3.10: Target signal path calculate in uniform soil

Layered Infill

The majority of practical target situations involve layered infill conditions, as shown in Figure 3.9(a). The layered infill has a small number layers each with it own refractive index. The radar signal is refracted and reflected at every dielectric interface where the permittivity changes, as shown in Figure 3.11. According to Snell's law, the target simulation model which calculates the distance the signals propagate through the soil must therefore be calculated by solving a set of non-linear equations as shown below:

$$n_1 \sin\theta_1 = n_2 \sin\theta_2 \tag{3.15}$$

$$n_2 \sin\theta_3 = n_3 \sin\theta_4 \tag{3.16}$$

$$\theta_2 = \theta_3 \tag{3.17}$$

The angles are given by trigonometric relationships below:

$$\sin\theta_1 = \frac{y_{un} - y_1}{\sqrt{(y_{un} - y_1)^2 + l_1^2}} \tag{3.18}$$

$$\sin\theta_2 = \frac{y_1 - y_2}{\sqrt{(y_1 - y_2)^2 + l_2^2}} \tag{3.19}$$

$$\sin\theta_4 = \frac{y_2 - y_{ta}}{\sqrt{(y_2 - y_{ta})^2 + (x_{ta} - (l_1 + l_2))^2}} \tag{3.20}$$

where θ_1, θ_2, θ_3 and θ_4 are the refractive angles at the layered infill interface and l_1, l_2 represent the layer thickness. (x_{un}, y_{un}) is the transmitter/receiver position. (x_{ta}, y_{ta}) is the target's position as shown in Figure 3.11.

When the target is in the second layer and third layer, there will be a different target path function which can be obtained by this manner. All target path functions in the layered medium are given in Appendix C.

The secant method [6] has been used to solve the non-linear equations to obtain target path. This is described in Appendix B.

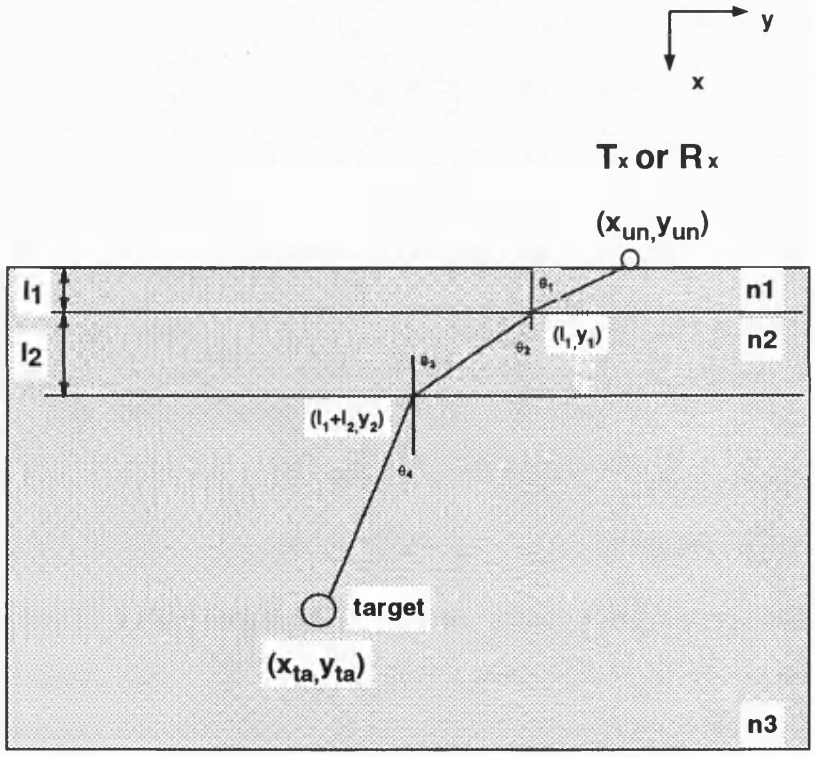

Figure 3.11: Target signal path calculation in layered soil

Trenched Infill Media

Trenched infill, as illustrated in Figure 3.12 has a two dimensional refractive index profile which may be encountered in pipe and cable installations. In the trenched infill case

the target path calculation becomes more complicated than in the cases above with the set of propagation relationships given below by Snell's law:

$$n_1 \sin\theta_1 = n_{23} \sin\theta_2 \tag{3.21}$$

$$n_{23} \sin\theta_3 = n_{22} \sin\theta_4 \tag{3.22}$$

$$n_{22} \sin\theta_5 = n_{32} \sin\theta_6 \tag{3.23}$$

$$\theta_3 = 90^o - \theta_2 \tag{3.24}$$

$$\theta_5 = 90^o - \theta_4 \tag{3.25}$$

and with the additional relationships as shown in Figure 3.12

$$\sin\theta_1 = \frac{y_{un} - y_1}{\sqrt{(y_{un} - y_1)^2 + l_1^2}} \tag{3.26}$$

$$\sin\theta_2 = \frac{y_1 - y_{t2}}{\sqrt{(y_1 - y_{t2})^2 + (x_1 - l_1)^2}} \tag{3.27}$$

$$\sin\theta_3 = \frac{x_1 - l_1}{\sqrt{(y_1 - y_{t2})^2 + (x_1 - l_1)^2}} \tag{3.28}$$

$$\sin\theta_4 = \frac{l_1 + l_2 - x_1}{\sqrt{(l_1 + l_2 - x_1)^2 + (y_{t2} - y_2)^2}} \tag{3.29}$$

$$\sin\theta_5 = \frac{y_{t2} - y_2}{\sqrt{(l_1 + l_2 - x_1)^2 + (y_{t2} - y_2)^2}} \tag{3.30}$$

$$\sin\theta_6 = \frac{y_2 - y_{ta}}{\sqrt{(y_2 - y_{ta})^2 + (tx - (l_1 + l_2))^2}} \tag{3.31}$$

All parameters used in these equations are as shown in Fig 3.12.

When the measurement unit's position is changed, the target path to transmitter/receiver will be varying, all the different target path functions in trenched medium are derived and provided in Appendix D. The Secant method as seen in Appendix B has been used to solve the non-linear equations.

3.8 Received Signal Characteristics

In order to calculate the characteristic of the received signals, the propagation is considered to be from the transmitter antenna to the target through the appropriate infill

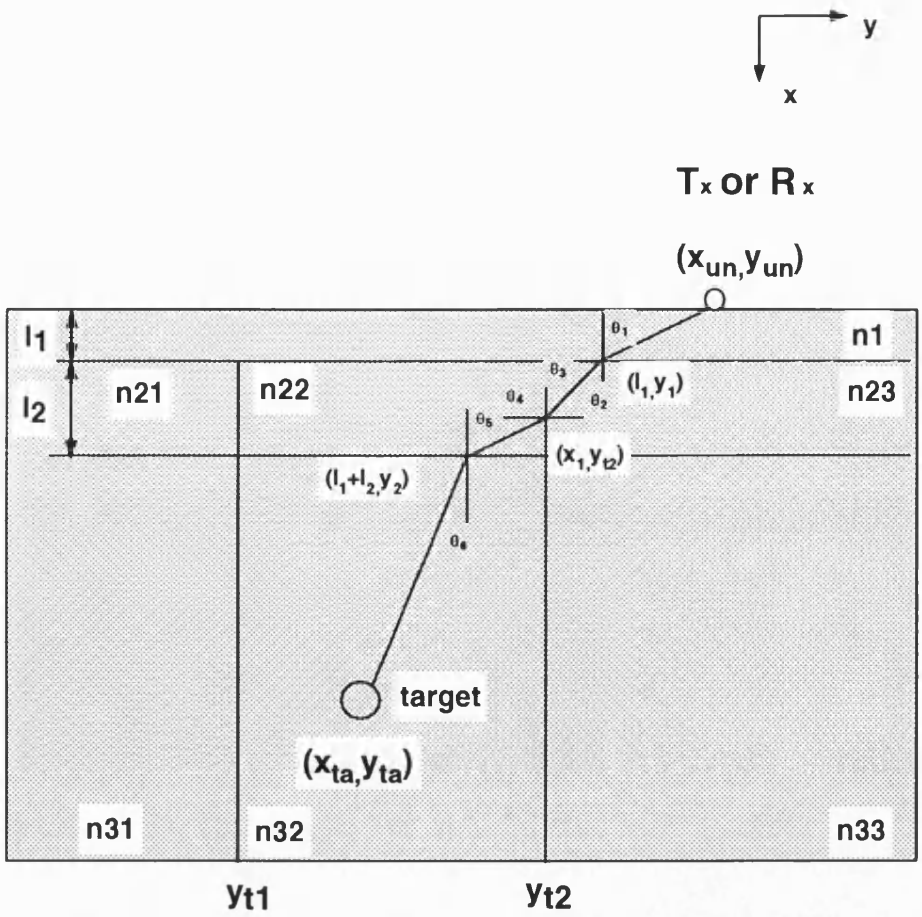

Figure 3.12: Target signal path calculation in trenched soil

configuration and back from the target to the receiver antenna.

Using this approach, it is therefore possible to characteries the transmitted signal and the received signal under the test condition. These provide the signals required for the Target Analysis process.

3.9 Conclusion

FMCW radar principles have been reviewed and the signal processing of the FMCW radar have also been studied. The mathematical model has been established. Details of radar system and target simulation have been provided which includes ray tracing algorithm to calculate target signal propagation path.

References

[1] Skolnik M I. *Introduction to Radar Systems.* Mcgraw-Hill, Inc, 1962.

[2] Botros AZ and Olver AD. Analysis of target response of FM-CW radar. *IEEE Transactions on Antennas and Propagation*, AP-34(4):575–581, April 1986. Author(s) with University of London, QMWC.

[3] Redfern M.A. and Pennock S.R. *Feasibility Study for Underground Cable Depth Measurement System.* University of Bath, 1992.

[4] Cook C E and Bernfeld M. *Radar Signals an Introduction to Theory and Application.* Academic Press, Inc, 1967.

[5] Yeh P. *Optical Waves in Layered Media.* c, 1988.

[6] Lafara R L. *Computer Methods for Science and Engineering.* c, 1973.

Chapter 4

Target Analysis Model Development

4.1 Outline

This chapter describes the target analysis model which includes various basic target analysis algorithms, these include the FFT algorithm, the convolution algorithm, the target depth calculation and the unit movement calculation. Other processes have been investigated to improve target detection resolution including the application of window functions, reference signal subtraction, target templating and different filter algorithms. This work includes an analysis of the effect of quantisation errors present in the target analysis algorithm due to Fast Fourier Transform(FFT) resolution. Finally a synthetic aperture algorithm for FMCW radar is included.

4.2 Target Analysis Model Outline

The Target Analysis Model (Figure 4.1) processes and analyses the audio-band frequency domain signals. The target analysis model forms the basis of the software that was used to analyse data in the experimental system.

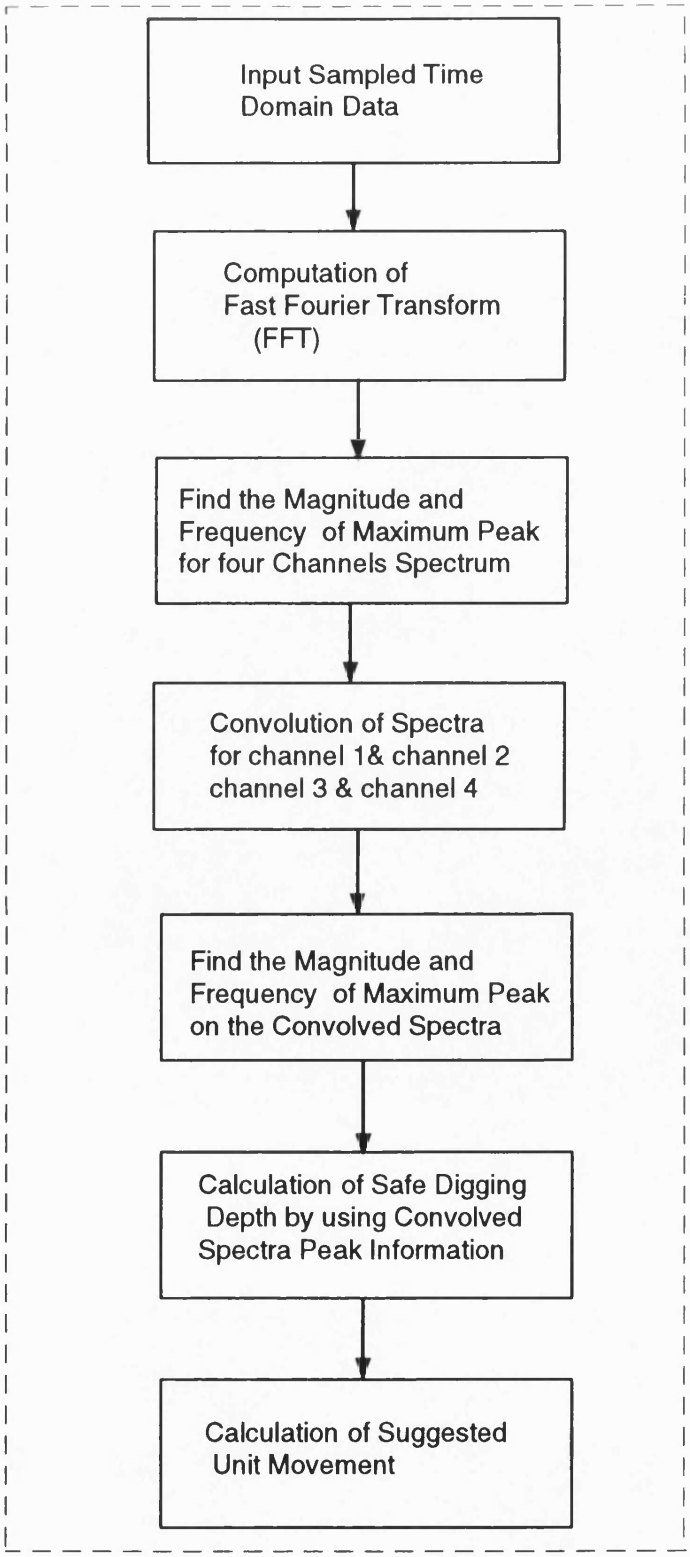

Figure 4.1: Target Analysis Model

The model has been developed to generate the two outputs that will be shown to the unit's operator. These are the arrows that indicate the direction the unit should be moved to place it directly over the target, and the depth reading when the unit is directly over the target.

A threshold level is used in calculating safe digging depth, in order to consistently provide a safe digging depth which is shallower than the target. This ensures that the system will always err on the side of caution hence giving a 'safe' digging depth.

The model has been developed to compute the safe digging depth and unit movement using a "triangulation" approach to eliminate the calculation of the refractive index of the infill. The performance of the "triangulation" approach has been investigated using realistic target situations with either single or multiple targets of various sizes, and at various depths.

The algorithms that have been developed to calculate the safe digging depth and the unit movement are shown in the following section.

4.3 Fast Fourier Transform(FFT) Algorithm

A Fast Fourier Transform(FFT) is used to transform the sampled time domain data to the frequency domain [1]. The process of computing the FFT of a series of time samples produces a discrete frequency spectrum, with frequency components calculated at a spacing of k Hz where k is given by:

$$k = \frac{Sampling\ Frequency}{Number\ of\ Points\ in\ the\ FFT}$$

Therefore only components at frequencies of nk Hz exist ($n = 1, 2, ...$). For Example, if $k = 5Hz$, only signals with frequencies at 5Hz, 10Hz, 15Hz, 20Hz, ... would have their true spectra calculated. If a signal was sampled which was not divisible by k Hz (e.g. 7.5Hz) the spectrum of that signal is computed as having components at 5Hz and 10Hz. This effect is known as spectral leakage [2].

Figure 4.2 illustrates that for a non-integral number of wavelengths spectral leakage

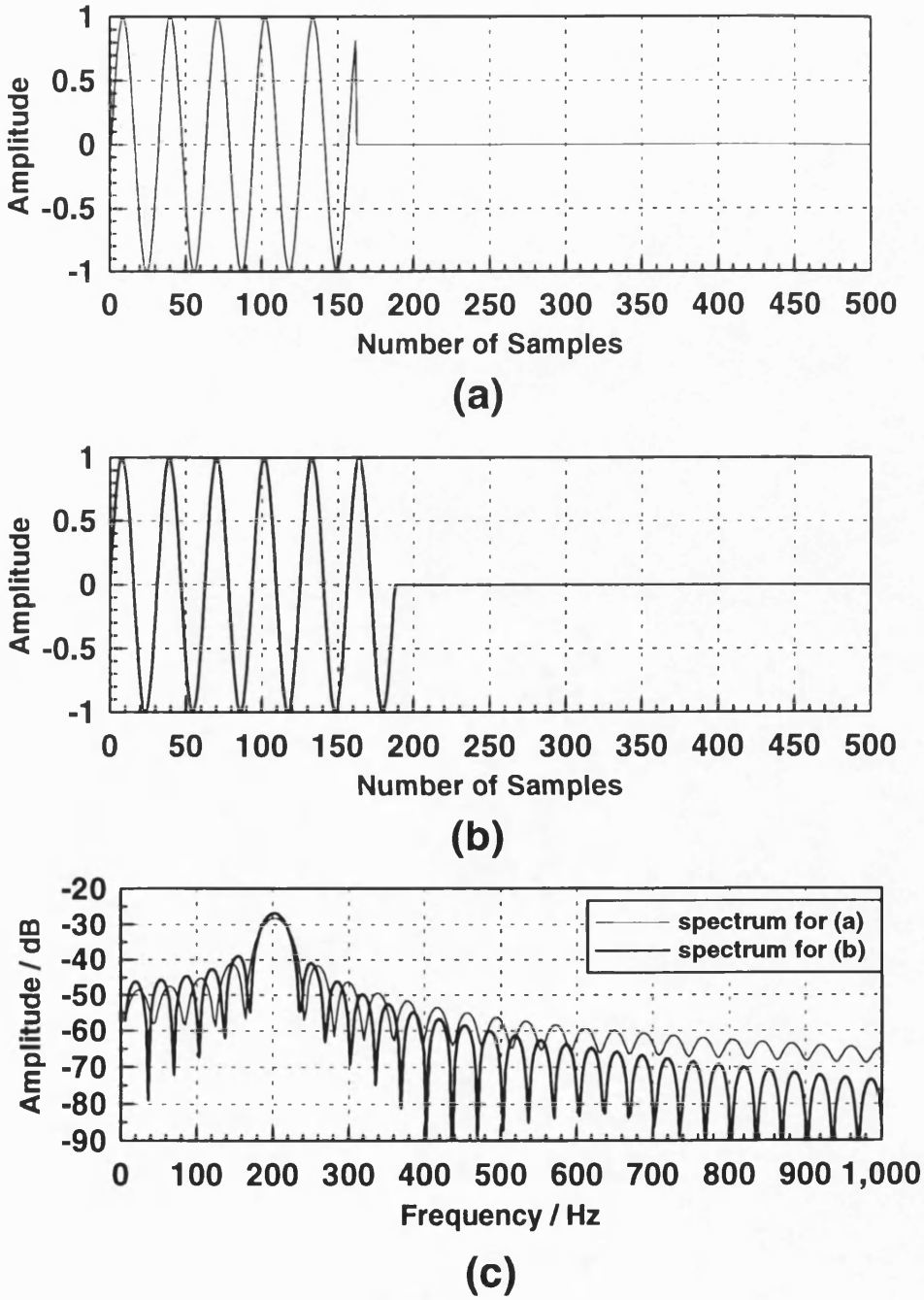

Figure 4.2: Sinewave burst with (a) Non-integral and (b) Integral number of wavelengths sampled and the (c) corresponding frequency spectrum

occurs, with signal power present at frequencies other than multiples of $1/T_r$. The degree of this spectral leakage is a function of the audio-band frequency difference signal and can change very rapidly with a small change in unit movement.

Two means of reducing this effect can be used. Firstly the resolution of the FFT can be reduced such that the value of k is greater than or equal to the repetition rate of the waveform studied. Alternatively the process of zero padding, or adding additional zeroes to the time series can be used to synchronize the effective repetition rate to that of the FFT resolution [3].

The latter has been implemented and has been shown to improve the performance of the process. It also decreases the sensitivity to small movements of the measurement unit.

4.4 Convolution Algorithm

The convolution Algorithm has been used in the target analysis model after FFT algorithm to enable the system to concentrate on targets directly below the measurement unit. This technique uses convolution of received waveforms which use similar but different paths to measure the target's path, and hence is able to filter reflections not obtained from targets directly beneath the measurement unit. The process also provides operators with simple instructions to position the measurement head directly over the principal target.

Figure 4.3 shows the convolution result for real measured data. This gives an enhancement of the signal return from the target directly below the system with a clearer peak than the unprocessed data. The off centre target response apparent in the channel 2 response has clearly been suppressed.

4.5 Safe Digging Depth Calculation

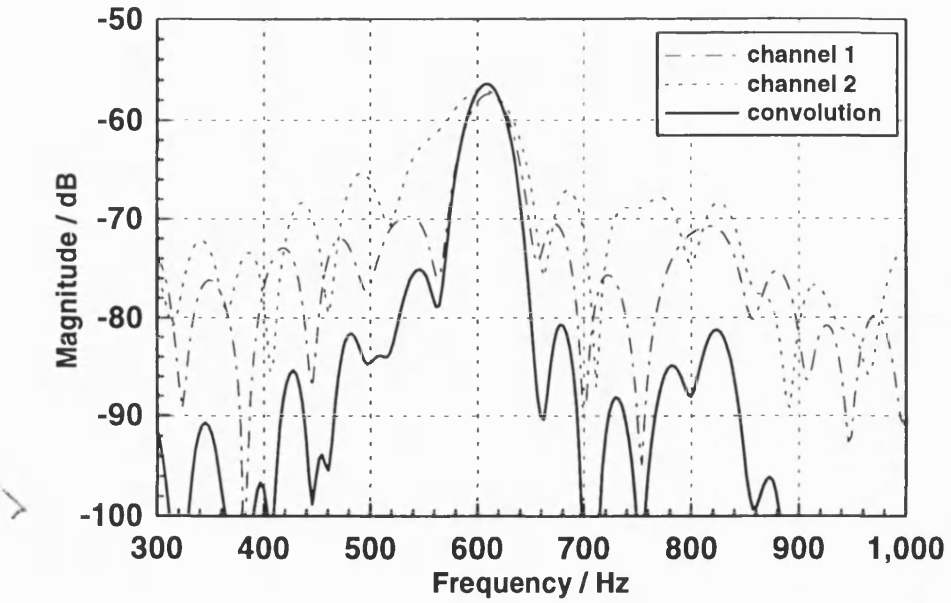

Figure 4.3: Output spectrum of the receiver mixer for Channel 1 (τ_1), Channel 2 (τ_3) and the convolved waveform

The safe digging depth calculation is based on the measurement of time delays (τ_1 to τ_4) while τ_1 is the time delay from T_A to R_A, τ_2 is the time delay from T_A to R'_A, τ_3 is the time delay from T_B to R_B and τ_4 is the time delay from T_B to R'_B which is computed from the frequency spectra from each of the four propagation paths shown in Figure 4.4 using the following equation

$$\tau_d = f_d \left(\frac{T_s}{\Delta f} \right) \tag{4.1}$$

where f_d is the frequency peak corresponding to the target; T_s is the time taken to sweep a frequency bandwidth Δf.

The threshold level detector has been introduced in order to cope with the situation where two target responses interfere. If no action were taken and main peak is used, the unit would provide too deep an indication of an safe digging depth(SDD). The simulated results have found that a threshold value of 3.0dB below the main peak provides a safe digging depth which meets the depth accuracy requirement of between 0 and -8.5cm.

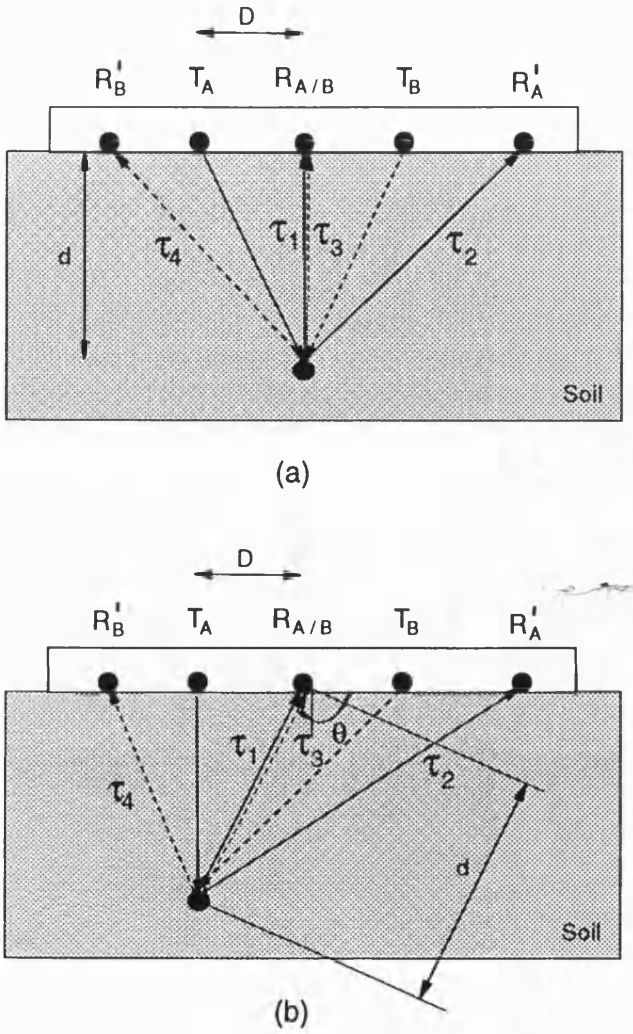

Figure 4.4: Relationship between time delays for (a) on-centre target, and (b) Off-centre target for a system with an antenna spacing D

4.5.1 Safe Digging Depth Computation for an Infill of Known Refractive Index

The initial target simulations used to verify the performance of the convolution technique used a calculation methodology with an infill of known value of the refractive index, n.

Denoting the signal propagation paths between T_A and R_A, and between T_A to R'_A, as shown in Figure 4.4; as R_1 and R_2 respectively: The distances can be computed from the corresponding frequency differences, f_{d1} and f_{d2} from:

$$R_1 = c\,\frac{f_{d1}}{n}\left(\frac{\Delta t}{\Delta f}\right) \qquad\qquad R_2 = c\,\frac{f_{d2}}{n}\left(\frac{\Delta t}{\Delta f}\right) \tag{4.2}$$

where c is the speed of light $c = 3\ \times 10^8$, Δt is frequency sweep time.

The digging depth and angle, θ, can be computed from the following formulae:

$$d = \frac{3R_1^2 - 2R_1R_2 + R_2^2 - 6D^2}{2(3R_1 - R_2)} \tag{4.3}$$

$$\cos(\theta) = \frac{1}{D}\left(\frac{R_1^2 - D^2}{2d} - R_1\right) \tag{4.4}$$

The derivations of Equations 4.3 and 4.4 are shown in Appendix A.

4.5.2 Safe Digging Depth Calculation for an Unknown Refractive Index

The safe digging depth calculations can also be formulated in terms of the signal propagation delays which removes the need to know the refractive index of the media. This formula is used in the experimental measurement system.

Using the process of convolution to filter out targets which appear off-centre, as shown in Figure 4.4(b), such that:

$$\tau_1 = \tau_3 \tag{4.5}$$

$$\tau_2 = \tau_4 \tag{4.6}$$

The time taken τ_1 and τ_2 can be represented as:

$$\tau_1 = \frac{n}{c} R_1 \tag{4.7}$$

$$\tau_2 = \frac{n}{c} R_2 \tag{4.8}$$

Where n is the unknown refractive index, c is the speed of light. Then the ratio of τ_1 and τ_2 is defined as T:

$$T = \frac{\tau_1}{\tau_2} = \frac{R_1}{R_2} \tag{4.9}$$

therefore T is independent of the refractive index n. The time delays are computed from the convolved waveforms and the safe digging depth is given by:

$$d = \frac{D}{2} \frac{3T^2 + 2T - 1}{\sqrt{2T^2 - 3T^3 + T}} \tag{4.10}$$

The detailed derivation of Equation 4.10 is shown in Appendix A.

This equation is valid when a target is detected directly beneath the unit as shown in Figure 4.4(a). In the case where an off-centre target is present, the unconvolved waveforms can be used to provide two equations with two unknown: the distance, d, and the angle, θ:

$$\frac{\tau_1}{\tau_2} = \frac{d + \sqrt{d^2 + D^2 - 2dD\cos(\theta)}}{\sqrt{d^2 + D^2 - 2dD\cos(\theta)} + \sqrt{d^2 + 4D^2 + 4dD\cos(\theta)}} \tag{4.11}$$

$$\frac{\tau_3}{\tau_4} = \frac{d + \sqrt{d^2 + D^2 + 2dD\cos(\theta)}}{\sqrt{d^2 + D^2 + 2dD\cos(\theta)} + \sqrt{d^2 + 4D^2 - 4dD\cos(\theta)}} \tag{4.12}$$

The above equation can be solved using numerical methods [4].

4.6 Safe Digging Depth Accuracy Studies

Important tests for the target analysis algorithm are the computation of the safe digging depth of a single target in uniform, layered and trenched media. Ideally the safe digging depth should equal the actual depth, however, thresholding applied to maintain the safe

digging depth will provide an underestimate of this value ensuring that the measurement is 'safe'. The numerical accuracy of the algorithm and the errors in this system will affect the system accuracy.

The results of this test are shown in Figure 4.5. The computed safe digging depth values all provide a consistent underestimate of the target depth. The results also indicate that for target below 0.8m, there is a linear variation in the safe digging depth with actual target depth. Above this value, a systematic variation in safe digging depth is observed, most particularly in the trenched case. For trenched case, because of the multiple reflection and refractions between the boundaries, the quantisation error is worse than uniform and layered cases. For example, when the actual target depth is 1m, the calculated safe digging depth is about 0.8m. The deeper the actual depth, the bigger the quantisation error is.

This systematic variation is a direct result of the quantisation of the time delays used in the safe digging depth algorithm which cannot be avoided.

4.6.1 Timing Quantisation Errors

The target analysis algorithm operates using sampled values of the frequency difference signal obtained from the UHF electronics sub-system. The Fast Fourier Transform (FFT) operation on this discrete data provides an estimate of the frequency spectra of the frequency difference signal at set frequency points, as determined by equalization. The frequency axis of the spectrum is only given at discrete values, and hence the peak of the frequency difference spectrum will occur at one of these points. This gives rise to a quantisation error where the actual peak frequency of the frequency difference signal may not coincide with a frequency point in the FFT spectrum. The maximum error is given by: frequency spacing/2=1.526Hz

The processing of the spectra converts the peak frequency of the FFT to a time delay for computing the safe digging depth in a closed form expression, hence any quantisation errors will have an effect on the accuracy of the safe digging depth calculation.

The quantisation process has been modelled using MathCad software and the result

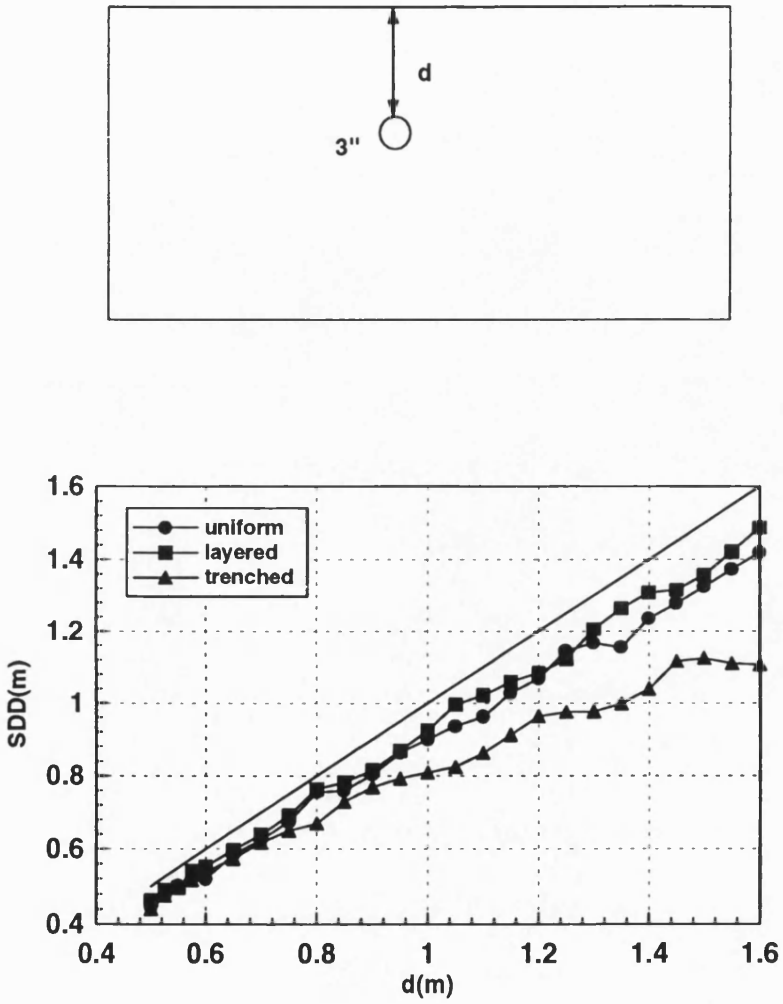

Figure 4.5: Variation in Safe Digging Depth (SDD) with actual target depth (d) for a single target

for the proposed two transmitter / three receiver configuration is shown in Figure 4.6.

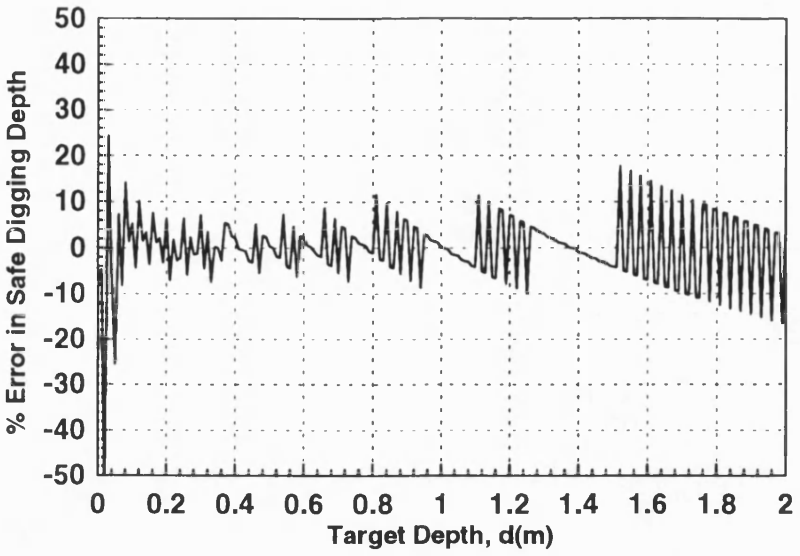

Figure 4.6: Percentage error in Safe Digging Depth for a single target due to quantisation error for the proposed two transmitter / three receiver configuration with a 2048 point FFT

The results indicate that the systematic variation seen in the safe digging depth computations for depths above 0.8m, are sample points of the error curve computed in Figure 4.6, and indicate errors due to quantisation of approximately 10% for targets with depth shallower than 1.5m. More important, the quantisation errors are both negative and positive. A negative error is acceptable in the calculation of the safe digging depth, however, a positive error would lead to the unacceptable condition where the calculated safe digging depth greater than the actual depth.

A negative quantisation error has been ensured by applying a threshold percentage value to the safe digging depth calculation, which effectively shifts the entire error curve. However, the problem of quantisation would still result in an accuracy that would not meet the specification for the system.

Two approaches can be used to reduce the effect of quantisation errors in the safe digging depth calculation:

- Increase the resolution of the FFT

- Increase the base line of the triangulation measurement to compute the safe digging depth.

4.6.2 FFT Resolution

An increase in FFT resolution would lead to a reduction in the frequency spacing of the FFT spectrum and hence the quantisation error. This is demonstrated in Figure 4.7.

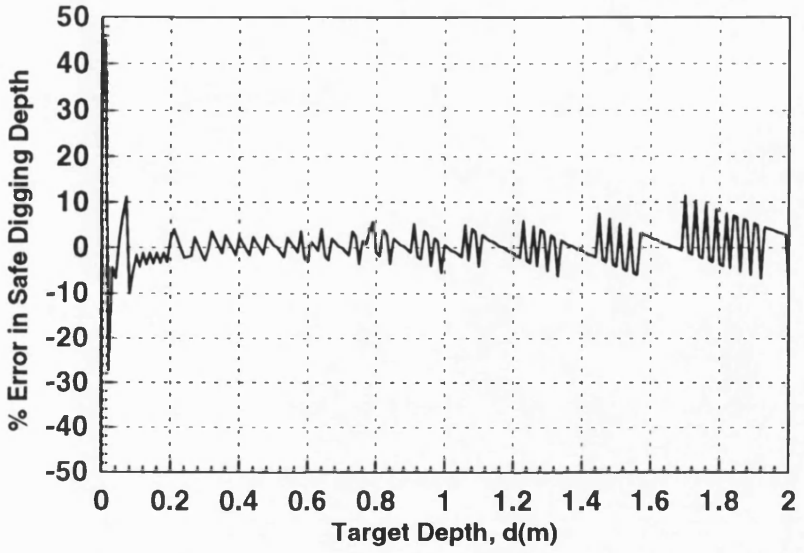

Figure 4.7: Percentage error in Safe Digging Depth for a single target due to quantisation error for the proposed two transmitter / three receiver configuration with a 4096 point FFT

The results show that reduction in the frequency spacing of the FFT spectrum by 1.526Hz produces an improvement of the quantisation error performance of a factor of two. Theoretically, this appears to provide the simplest means of reducing the quantisation error.

In practice, the safe digging depth algorithms rely on accurately computing the peak of the frequency spectrum. The peak value may only be a fraction of a dB above the surrounding values, hence by increasing the FFT resolution this difference in amplitude between successive points will decrease. This may increase the susceptibility of the algorithm to noise. In addition the computation time of FFT will increase hence slowing

the process, which may not be acceptable in the real system.

4.6.3 Transmitter Receiver Configurations

The increase in resolution of the FFT directly reduces the quantisation error present in the system. The configuration of the transmitters and receivers can also directly influence the effect of the quantisation errors.

The safe digging depth algorithm uses a triangulation approach to determine the depth of a target. The algorithm effectively uses two propagation delay measurements, and the studies have shown that the difference in propagation path length between these two measurements is critical to the effect of the quantisation errors. The overall length of the unit is set by the target specification of a one metre length, hence the reduction in the effect of the quantisation error can only be achieved by altering the transmitter / receiver configuration.

Figure 4.8(b) shows the proposed two transmitter / three receiver configurations for the measurement unit. This configuration has a base line difference of 2D between the R_A and R'_A, where D is the separation between the transmitter and receiver elements. Figure 4.8(a) also shows another $1D$ configuration.

A number of studies have been carried out with the $3D$ configuration shown in Figure 4.8(c). These results are shown in Figures 4.9 and 4.10.

These results show a reduced effect of quantisation errors on the safe digging depth calculation. In broad terms, the revised configuration improves the error performance by a factor of two, indicating a percentage error of five percent for depths up to 2 metres when a 4096 point FFT is used in conjunction with a $3D$ measurement configuration.

In all the cases examined it is apparent that the percentage error is quite high for target depths of less than 5cm. This effect appears to be a general limitation of the triangulation approach as opposed to a quantisation error effect and places a lower limit on the effective operating range of the unit.

Using this 3D configuration requires the function of same heads to be switched. The

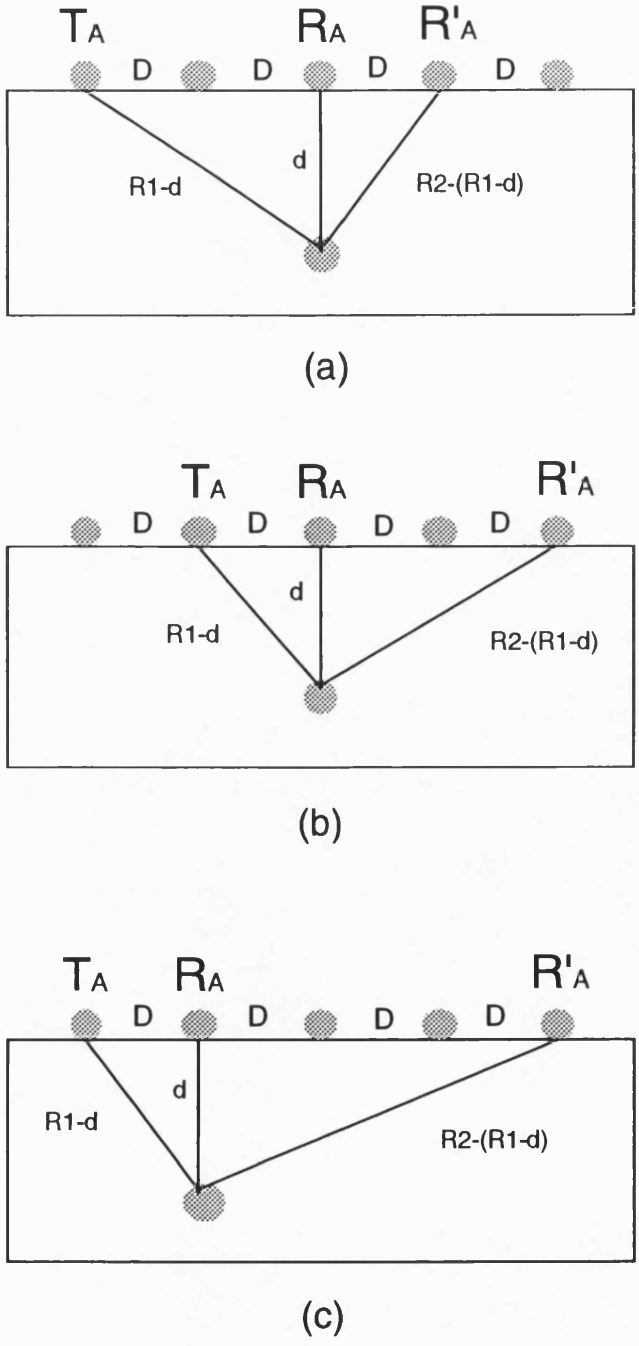

Figure 4.8: Transmitter and receiver configurations. (a) 1D configuration (b) 2D configuration (c) 3D configuration

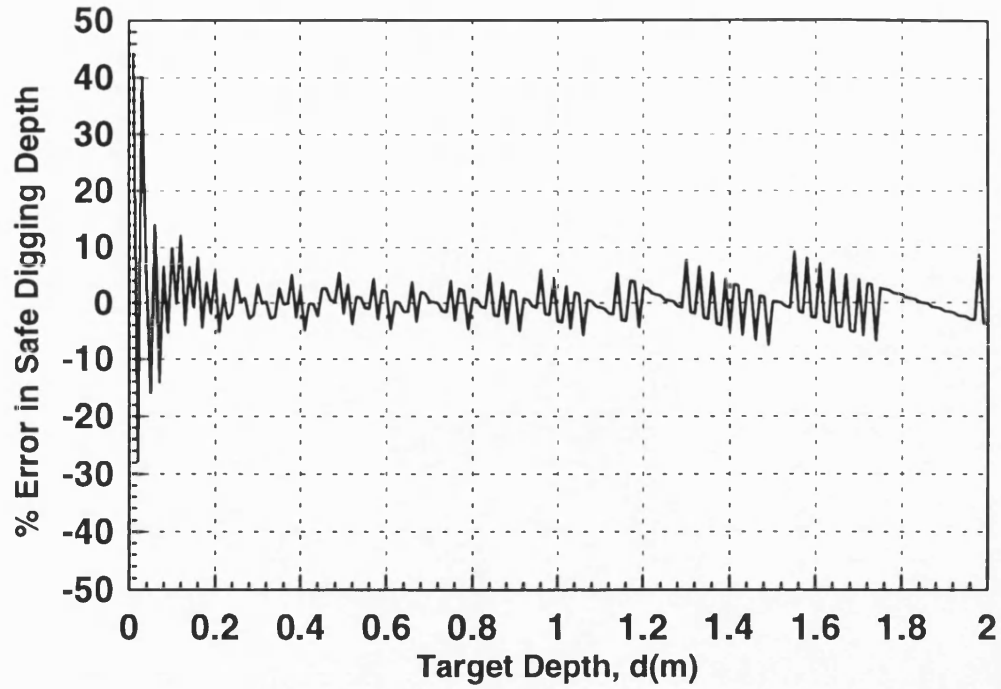

Figure 4.9: Percentage error in Safe Digging Depth for a single target due to quantisation error for the transmitter / receiver 3D configuration with a 2048 point FFT

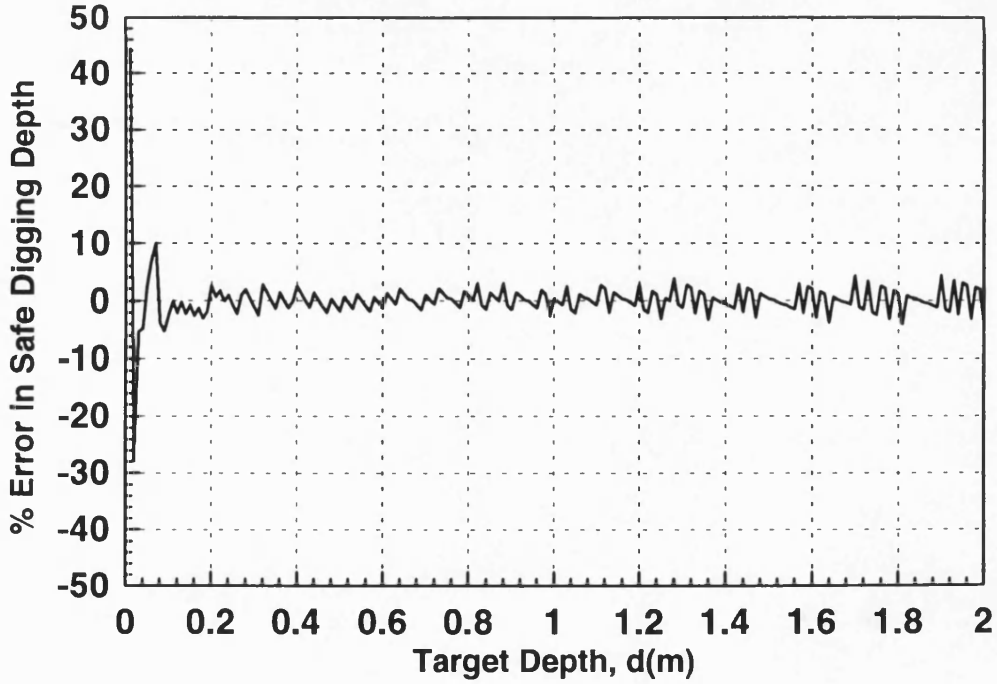

Figure 4.10: Percentage Error in Safe Digging Depth for a Single Target due to Quantisation Error for the Transmitter / Receiver 3D Configuration with a 4096 Point FFT

old configuration does not require a switch. Switches have recently become cheaply available.

4.7 Effect of Input Signal Phase

Figure 4.11 shows the effect of the initial phase of the input signal on the frequency spectrum. The maximum effect was determined for a phase of 30^o. The phase of the frequency difference signal is dependent on the target, hence will vary randomly for a set of measurements. The main peak frequency, as expected is independent of the initial phase, however the sidelobe level varies below 30dB down on the main peak amplitude (200Hz).

Figure 4.12 shows the result of subtracting the spectrum of the signal with a zero initial phase from the signal with a 30^o initial phase. The results show a practical "noise" floor on a subtraction technique will be around 35dB below the main peak of the spectrum. They also show a spurious response 28dB below the main peak.

4.8 Computation of Unit Movement

The system uses its two transmitter / three receiver arrangement to focus on targets directly below the unit. A means of deciding when the unit is above a target has therefore been formulated and is shown in the flow diagram of Figure 4.13.

The algorithm computes the spectra from each of the receiver channels and identifies the peaks corresponding to targets by using a threshold value 12dB below the peak amplitude of the spectrum. For each of the peaks that are identified the algorithm then determines the sidelobe level. If this level is significantly greater than 12dB then this indicates that multiple targets are present. 12dB corresponds to the sidelobe level of a single target and hence when the sidelobes are greater than this, it is reasonable to assume that a second target is present.

In the presence of multiple targets the $T_A - R_A$ and $T_B - R_B$ spectra are convolved

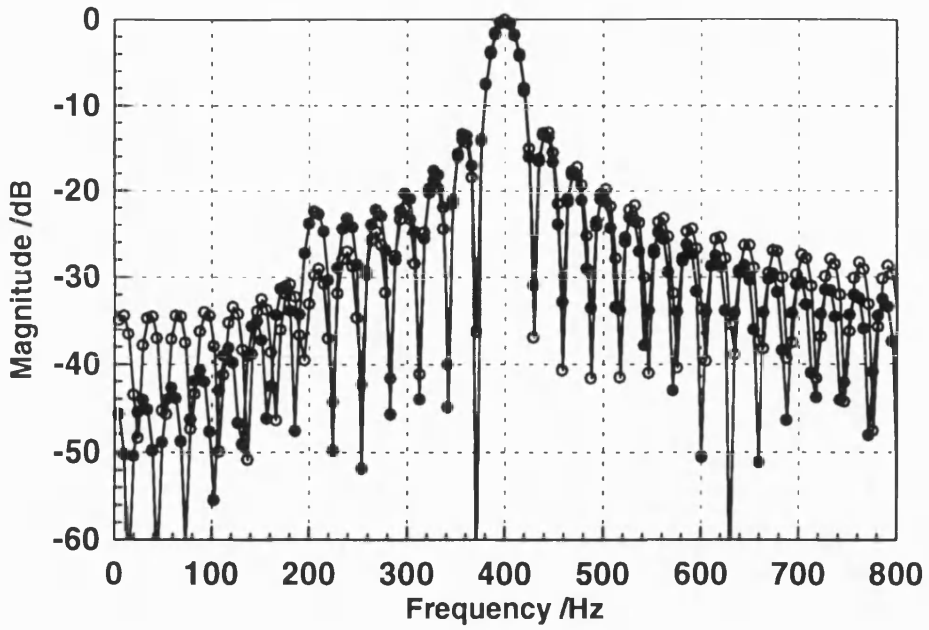

Figure 4.11: Variation in spectra of input signal for an initial phase of 0° (○) *and* 30° (•)

to sharpen the target response. The peaks of the convolved spectra are then compared to the peaks in the individual responses. If the peaks coincide to within a threshold level of 20Hz, then the algorithm determines that a target is directly below the unit. Otherwise the algorithm computes the unit movement to place the target on the unit centre line by comparing the peak responses of the receiver channels.

The process for a single target is identical, however in this case the convolution is not required to sharpen the target responses.

4.9 Processing and Display Algorithms

In addition to the development of the target analysis algorithms, work has also been undertaken into the processing of the data obtained from the scans recorded across the target area. The aim of this work has been to provide a two dimensional image of buried target from the scans in order to aid the development of the target analysis algorithms

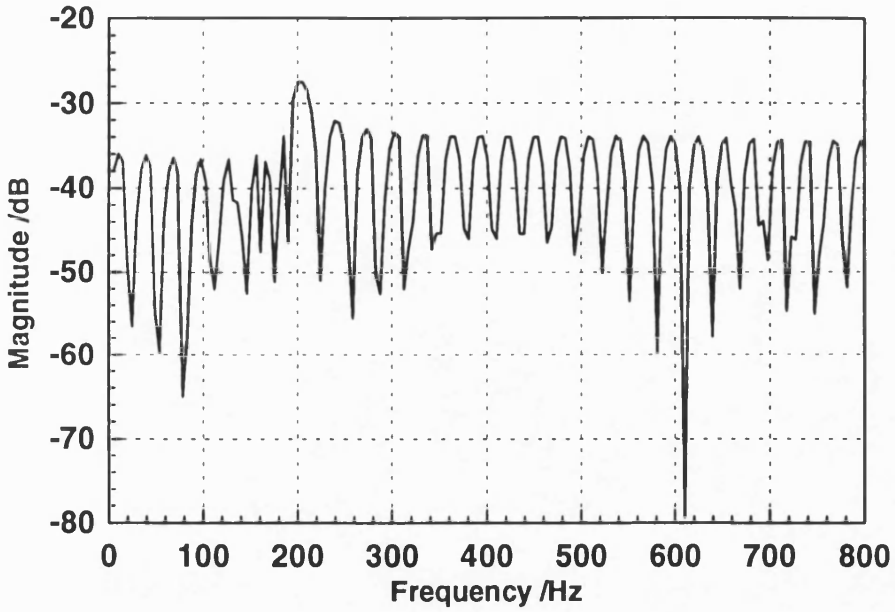

Figure 4.12: Difference between spectra of input signal for an initial phase of 0^o *and* 30^o

through improved data interpretation.

The algorithm development has primarily involved the merging of data from a number of scans and the output in a common format for plotting as a two dimensional colour intensity plot. The software is currently in a form such that data from any set of system tests can be easily merged into a two dimensional scan format.

4.10 Application of Window Functions

Window functions are widely used in signal processing as a means of reducing the sidelobe level associated with the Fourier Transform of a rectangular pulse. This improvement is achieved at the expense of a broader main peak. Sidelobe attenuation can be achieved using specially constructed window function [2] and the effects of some of these have been investigated.

The general form of a window function is given below, for a sequence of M time

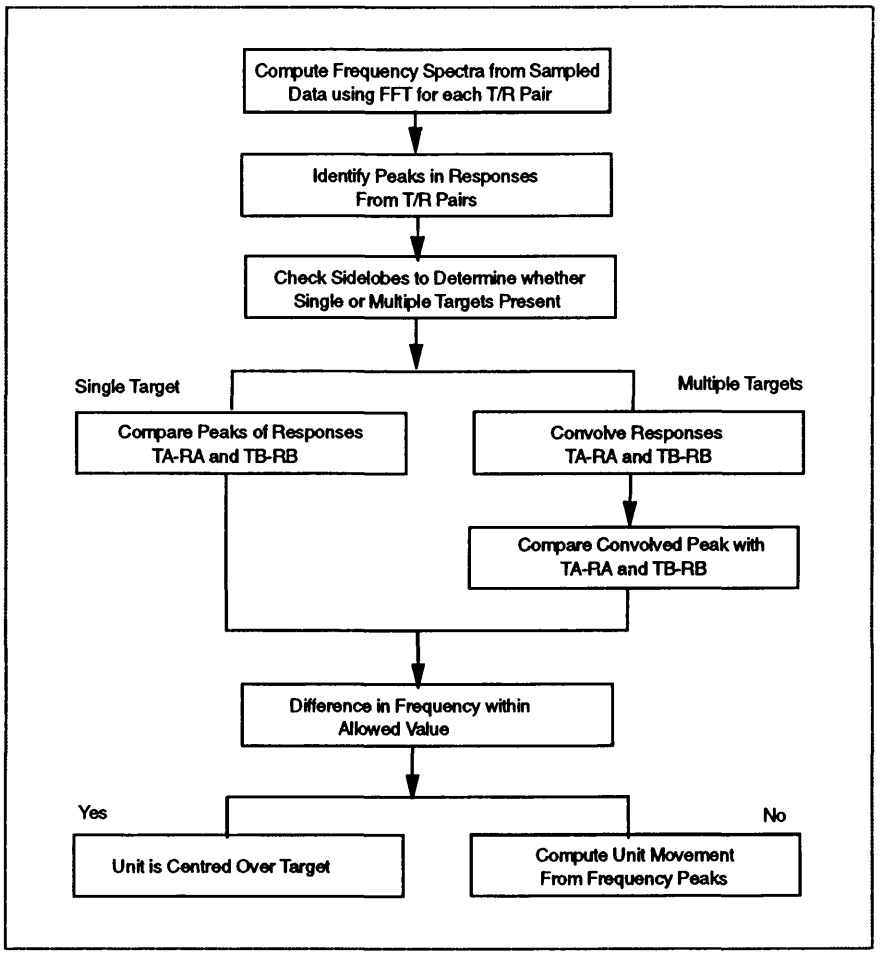

Figure 4.13: Outline of the algorithm used to compute when the unit is directly above a target

samples:

$$w(n) = \alpha - (1 - \alpha)\cos\left(\frac{2\pi m}{M-1}\right) \qquad 0 \leq m \leq M-1 \tag{4.13}$$

The Fourier transform of a number of window functions is given in Figure 4.14.

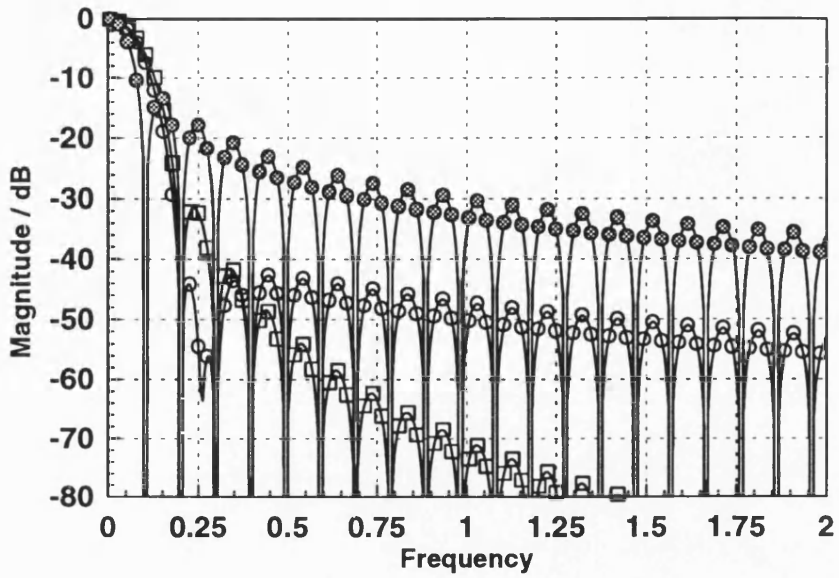

Figure 4.14: Frequency spectrum for a rectangular window, $\alpha = 1$,(•), a Hamming window, $\alpha = 0.54$, (∘), and a Hanning window, $\alpha = 0.50$, (□)

The value of $\alpha = 1$ provides a rectangular window, and is equivalent to not applying a window function to the time series. This has the narrowest peak, but with a relatively high sidelobe level. The Hamming window with $\alpha = 0.54$ and Hanning window with $\alpha = 0.50$ show a broader peak, but with a much reduced sidelobe level.

The processing applied to the real system tests data used a Hanning window with $\alpha = 0.50$, and the results are shown in Figure 4.15. These show an attenuation of the sidelobe level and broadening of the main peak by the window function. Figure 4.15 also demonstrates that for a signal with a broad asymmetrical peak, as would be expected with an interacting target response.

The work on the use of windowing has concluded that the technique would be of

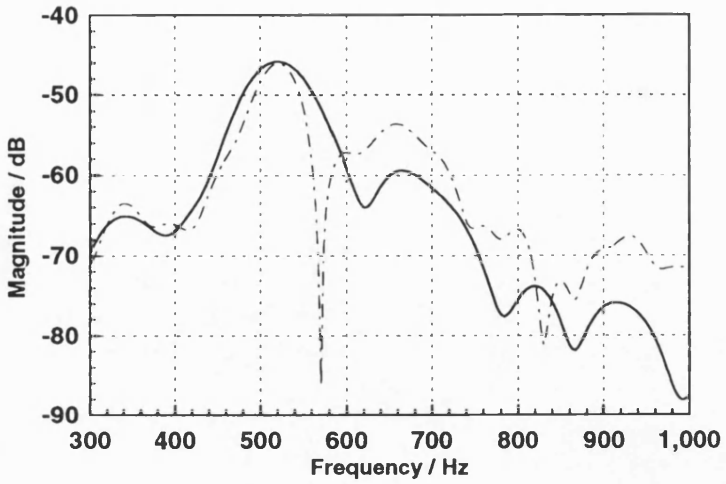

Figure 4.15: Unprocessed (— - —) and windowed (—) frequency spectra computed from sampled data

value where significant sidelobe interaction causes a ghost target, however for targets where main lobe interaction is dominant, the technique cannot be applied due to the possible distortion of the frequency peaks. The broader main peak will also have poor accuracy in time delay because it is difficult to find the peak.

4.11 Application of Target Templating

This 5 head FMCW system detects target by measuring target propagation path, but at the same time the transmitted signal also propagates directly into the receiver which we call the direct coupling signal. Usually the unwanted direct coupling signal is stronger than the target response. Target templating has been investigated as a means of reducing the effect of interaction between the desired target response and the undesired direct coupling signal between the transmitter and receiver antennas. The templating technique is based on the mathematical process of convolution, using a template function and can be described as:

$$resp(t) = \int_{-\infty}^{+\infty} sig(\tau)\ templ(t-\tau)\ d\tau \tag{4.14}$$

The function $resp(t)$ can be seen as a computation of the overlap of the input signal $sig(t)$, and the template function, $templ(t)$, as the template function is swept across the x ordinate. The integral will provide the maximum response when the signal and template coincide. The convolution process can be implemented using the following relationship:

$$RESP(X) = SIG(X) \cdot TEMPL(X) \tag{4.15}$$

where the upper case function represents the Fourier transform of the lower case function, hence the templated response is given by the Inverse Fast Fourier Transform (IFFT) of $RESP$.

A flow diagram of the templating technique used in the target analysis algorithm is shown in Figure 4.16. The template is defined in the time domain and the FFT taken to produce the template function in the frequency domain. The Fourier transform of the template and the audio-band frequency difference spectrum is then computed and multiplied together. The IFFT is then taken to transform the templated data back to the frequency domain.

4.11.1 Target Templating with $\frac{\sin x}{x}$

For an ideal FMCW radar return signal, the difference frequency spectrum will have a $\frac{\sin x}{x}$ characteristic. The real radar return signal spectrum will combine the $\frac{\sin x}{x}$ spectrum, noise and any multi-target interaction. The theoretical study of templating uses the template function $\frac{\sin x}{x}$ and an input signal simulated by a uniform sine wave burst.

A comparison of the magnitude of the input signal and the output response of the templating algorithm with a $\frac{\sin x}{x}$ template function are shown in Figure 4.17. The results indicate that the use of this templating algorithm has left the shape of the signal unchanged, hence indicating its inability to sharpen the response, and hence enable the algorithm to reduce the effect of the main 'noise' signal possibly from the direct coupling response and sharpen the desired target response. The theoretical proof of this result is given in the Appendix F.

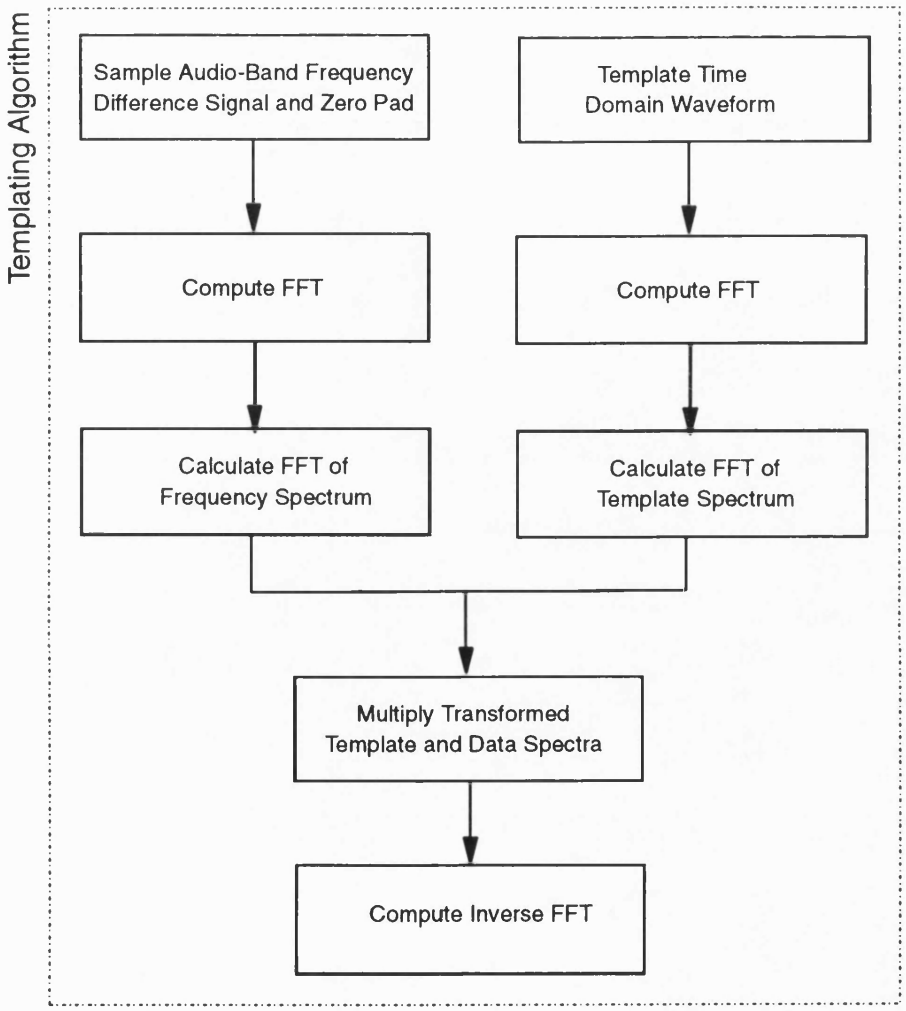

Figure 4.16: Outline of templating algorithm

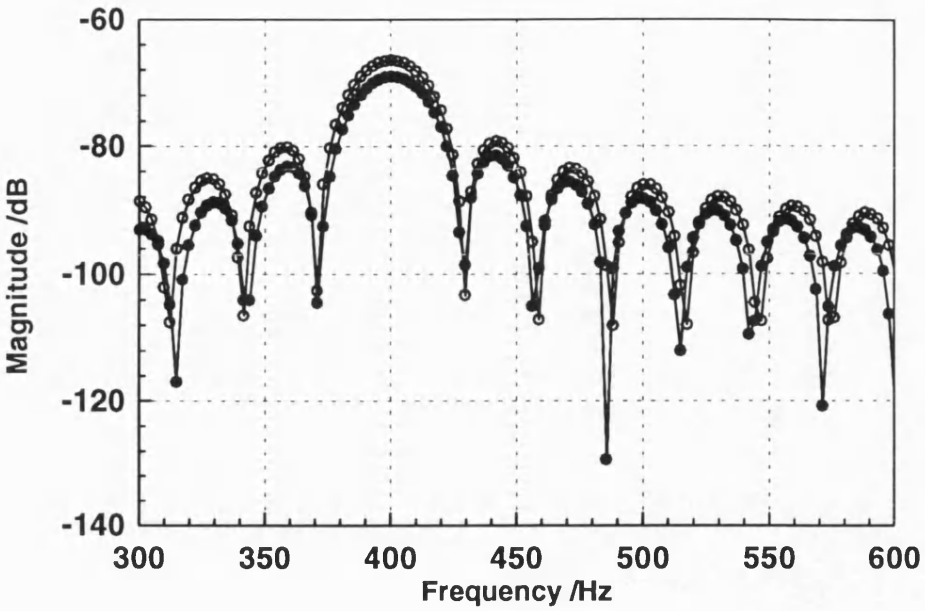

Figure 4.17: Magnitude comparison of input (•) and output (○) of templating algorithm using a $\frac{\sin x}{x}$ *template function*

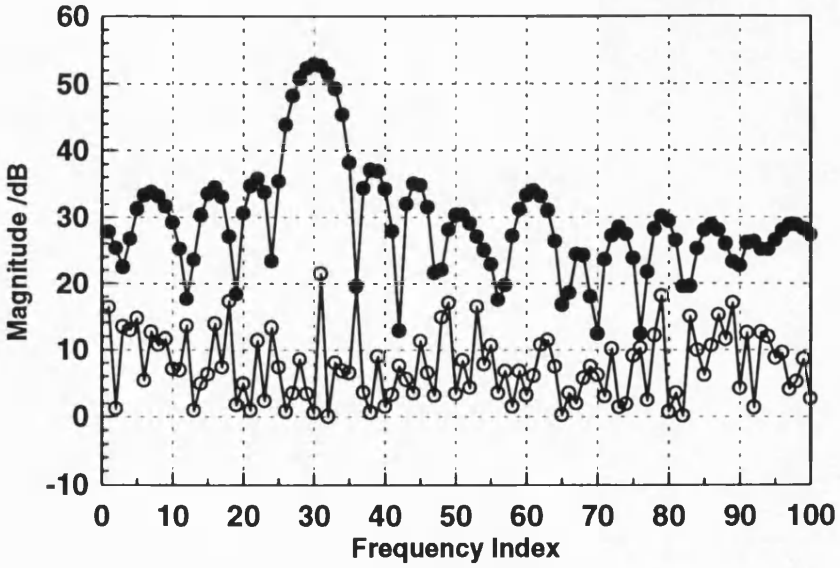

Figure 4.18: Magnitude comparison of input (○) and output (•) of templating algorithm using a $\frac{\sin x}{x}$ *template function against noise*

Although target templating with $\frac{\sin x}{x}$ as template function didn't show an ability to sharpen the response, this method can be used in filtering out general noise. When the input signal contains a single frequency component plus general noise, even if the noise is stronger than the signal, after templating with $\frac{\sin x}{x}$, the output shows that noise has been considerably removed and left the correct signal spectrum as shown in Figure 4.18 whose relative magnitude of signal verse noise is 1:10.

4.11.2 Triangular Templating

Work has also been carried out to compute a suitable template function to give a desirable output from the templating algorithm, called triangular templating. Expressing the output of the templating algorithm $O(\omega)$ in terms of the Fourier Transform of the Input Signal, $F(\omega)$, and the template function, $T(\omega)$:

$$O(\omega) = \mathcal{F}^{-1}\left[\mathcal{F}[F(\omega)] \bullet \mathcal{F}[T(\omega)]\right] \tag{4.16}$$

Given a desired output of the templating algorithm, $G(\omega)$, a suitable template function can be described as:

$$T(\omega) = \mathcal{F}^{-1}\left[\frac{\mathcal{F}[G(\omega)]}{\mathcal{F}[F_t(\omega)]}\right] \tag{4.17}$$

Where $F_t(\omega)$ is the input template signal for which the template is derived.

Single Frequency Input Signal

Suppose that the output signal $G(\omega)$ is a delta or a triangle function, and that the input signal is a uniform sine wave burst. The template function is derived from Equation 4.17, and, the output signal is obtained from Equation 4.16.

Figure 4.19 shows the comparison of the magnitude of the input and output responses of the templating where the template function was derived for a delta output signal at 30 frequency index(92Hz). When the input template signal and the input signal are at the same frequency, the output signal has a triangular response. When the input template signal frequency and the input signal frequency differ, the output signal has

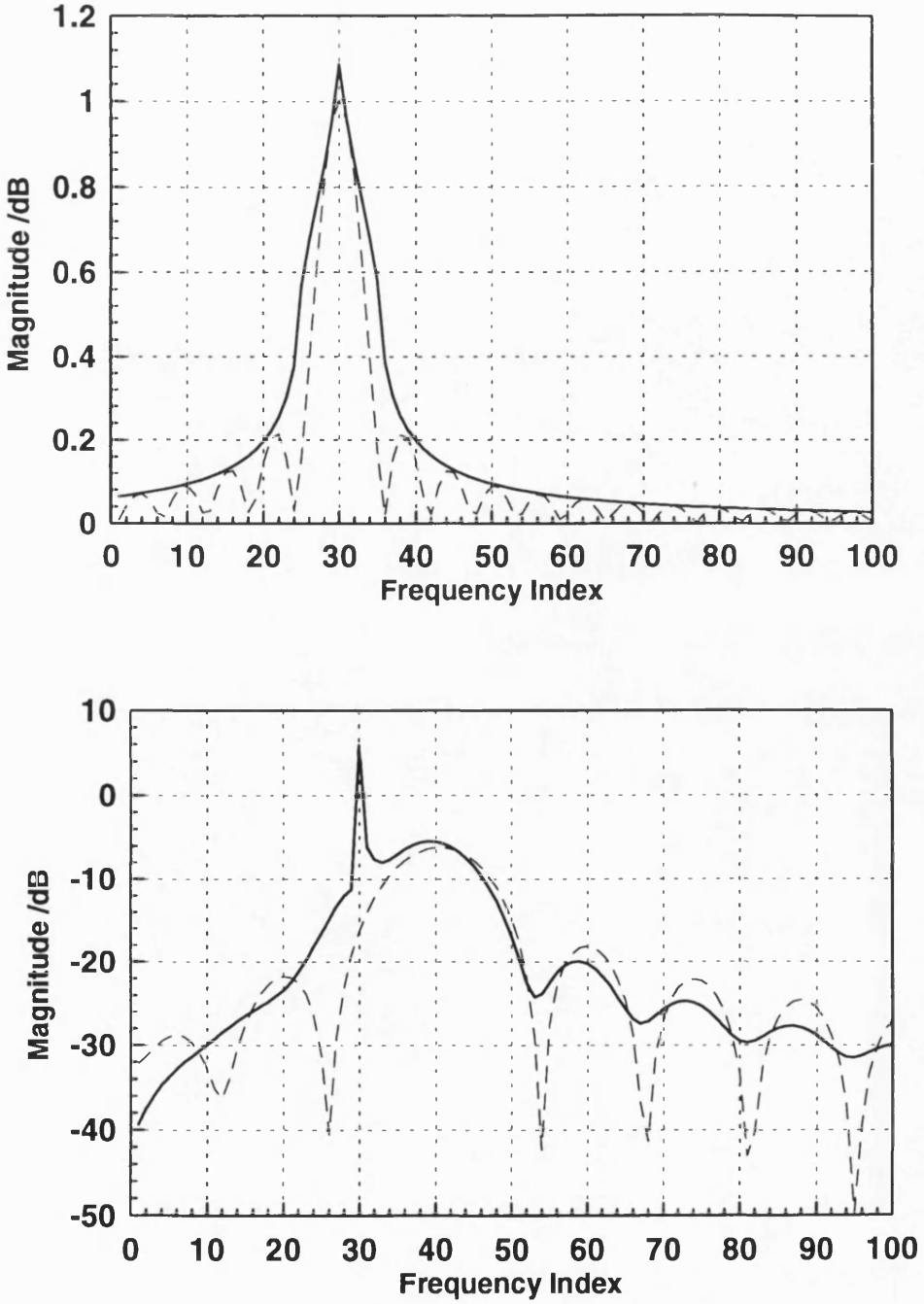

Figure 4.19: Magnitude comparison of input(- - -) and output(—) of triangular templating with single frequency input, (a) Input frequency equals template signal frequency, (b) Input frequency is offset template signal frequency

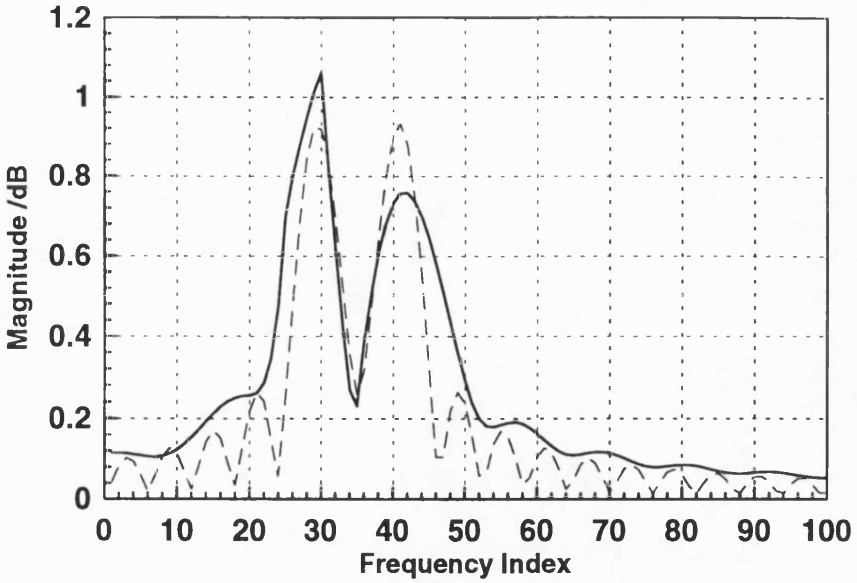

Figure 4.20: Magnitude comparison of input(- - -) and output(—) of triangular templating with two tone input signal

two peaks responses, one is on the template function frequency which is a triangle response, another is a broader peak near the input signal frequency.

In conclusion the output of triangular templating always has a sharp peak at the template frequency but that does not follow the input signal frequency. Hence triangular templating is not suitable for practical use.

Two Tone Input Signal

Consider the case where the input signal has two frequencies, one is equal to the input template signal's frequency, the second frequency has Δf separation from the first frequency. The output from triangle templating has two peaks, one is a sharp peak at the input template signal's frequency, the second is a broader peak is placed near by as shown in Figure 4.20.

When increasing the frequency separation Δf between these two input frequencies,

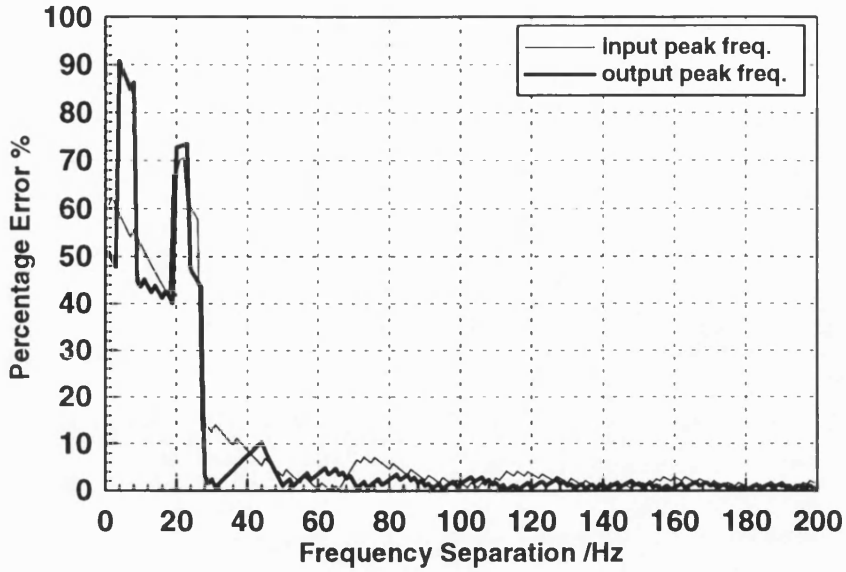

Figure 4.21: The percentage error of the second peak verse the accurate input second frequency from triangular templating algorithm

the output second peak position of output will change. Figure 4.21 is the percentage error of the output second peak frequency compare with the accurate input second frequency. The results show that the algorithm can resolve and accurately compute the two frequencies when their separation is greater than their 3dB bandwidth, corresponding to 36 Hz in this example. This may be adequate for some measurement studies where targets have sufficient separation, but is not adequate in all situations.

4.12 Reference Signal Subtraction Algorithm

The reference signal subtraction algorithm has been used to reduce the noise and clutter level, particularly the cross coupling between transmitter and receiver which is usually stronger than target return. The reference signal has been chosen either $\frac{\sin x}{x}$ signal or a practical measured data.

4.12.1 Using $\frac{\sin x}{x}$ as Reference Signal

An algorithm to subtract a reference signal $\frac{\sin x}{x}$ has been implemented, in order to reduce the effect of the direct coupling signal on the desired response.

The algorithm has been tested using data obtained from the system tests. In this test a $\frac{\sin x}{x}$ response with a main peak centred on the frequency of the direct coupling path was subtracted from the measured data. The variation in the amplitude of the sampled time domain signal, due to the amplitude response of the antennas, the UHF electronics, and the attenuation factor of the ground, provides a significant distortion to the frequency spectrum. Therefore $\frac{\sin x}{x}$ subtraction could not remove the cross coupling completely as shown in Figure 4.22. In this example, before the $\frac{\sin x}{x}$ subtraction, the spectrum peak position is around 520Hz. After the subtraction, there are two significant peaks. The target peak appears at higher frequency than the direct path. The direct path signal is only partially removed leaving a peak at a frequency less than the direct path frequency. This leads to an incorrect target position detection.

Hence the $\frac{\sin x}{x}$ subtraction algorithm has been tested using real data, but does not show satisfactory results.

4.12.2 Using a Practical Data as Reference Signal

The algorithm was also tested with a reference signal derived from a measurement. In the test bed shown in Figure 6.3, the reference signal was taken at a horizontal distance of 150cm where there is no target, while the target is at a position 390cm. The results are shown in Figure 4.23. In the unprocessed data the results show a number of peaks whereas in the processed response with the reference signal subtracted, a target can be indicated at around 240Hz. The processed signal shows a response similar to the expected $\frac{\sin x}{x}$ distribution.

This algorithm forms the basis of the target analysis algorithm. The measured results are provided in Chapter 6.

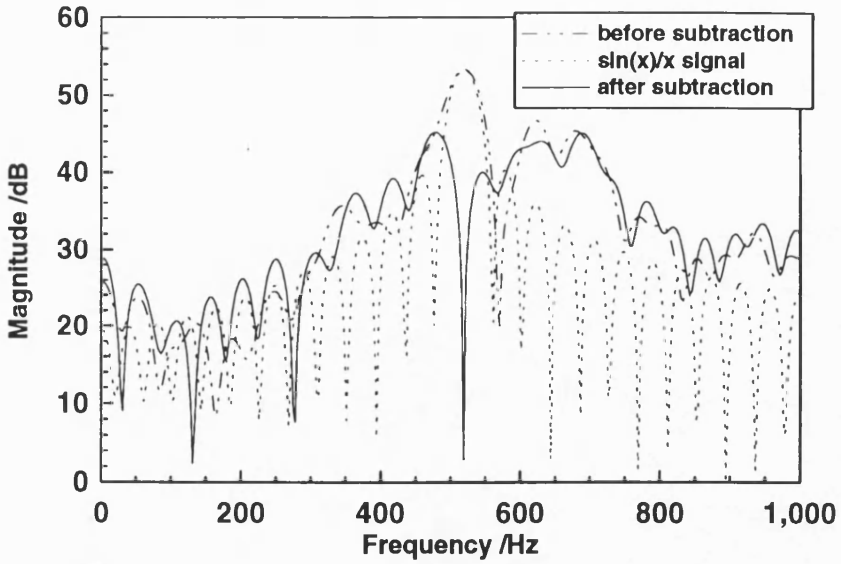

Figure 4.22: Subtraction with $\frac{\sin x}{x}$ from test data

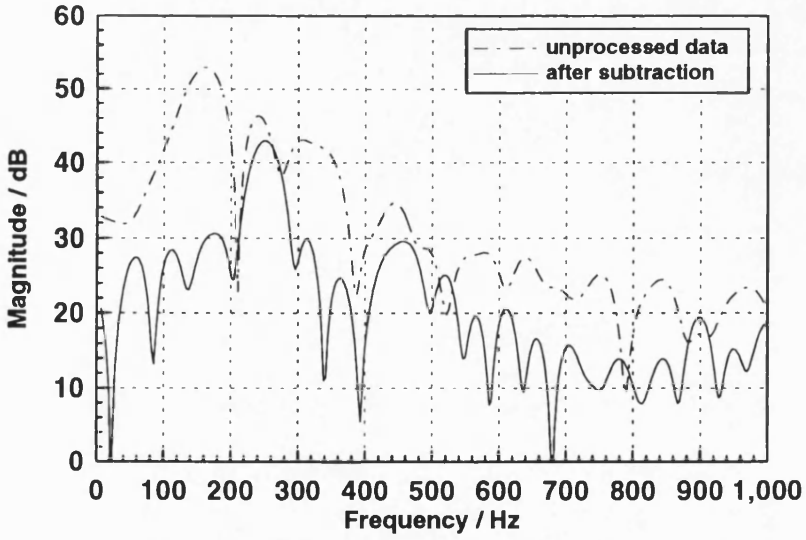

Figure 4.23: Subtraction with a reference signal from test data

4.13 Alternative Filter Algorithms

Three alternative filters have been studied to be used on the FMCW radar return signal in order to reduce the effect of noise and direct coupling.

4.13.1 Inverse Filter

The inverse filter [5] transfer function as seen in Equation 4.18 is a reciprocal of the input signal's spectrum multiplied by a time delay.

$$H(\omega) = \frac{1}{S(\omega)} \exp(-j\omega t_d) \tag{4.18}$$

Here t_d is the time delay which makes the filter realistic. Then the output signal as seen in Equation 4.19 is an integral of the input signal $sig(t)$ multiplied by the time reversed filter response $filter(t-\tau)$ and the output spectrum can be calculated by Equation 4.20. The output spectrum $I(\omega)$ should be 1,

$$resp(t) = \int_{-\infty}^{+\infty} sig(\tau)\ filter(t-\tau)\ d\tau \tag{4.19}$$

$$I(\omega) = S(\omega) \cdot H(\omega) = 1 \tag{4.20}$$

that means the output signal has Delta function response in time domain. The inverse filter is closely related to the previous investigations into the derivation of a suitable function to resolve the output of templating algorithm into a delta function.

The results from the inverse filter for a single frequency input signal is shown in Figure 4.24. The inverse filter transfer function is derived from a 92Hz sine wave burst. The output produced a triangular spectrum when the input frequency is coincident with the filter's set up frequency. When the signal and filter set up frequencies differ the output is a sharp response at the filter frequency and plus broader sidelobes near the signal frequency.

The result for a two frequency input signals situation is shown in Figure 4.25. When the separation between the two frequencies is increased, the output always has a sharp

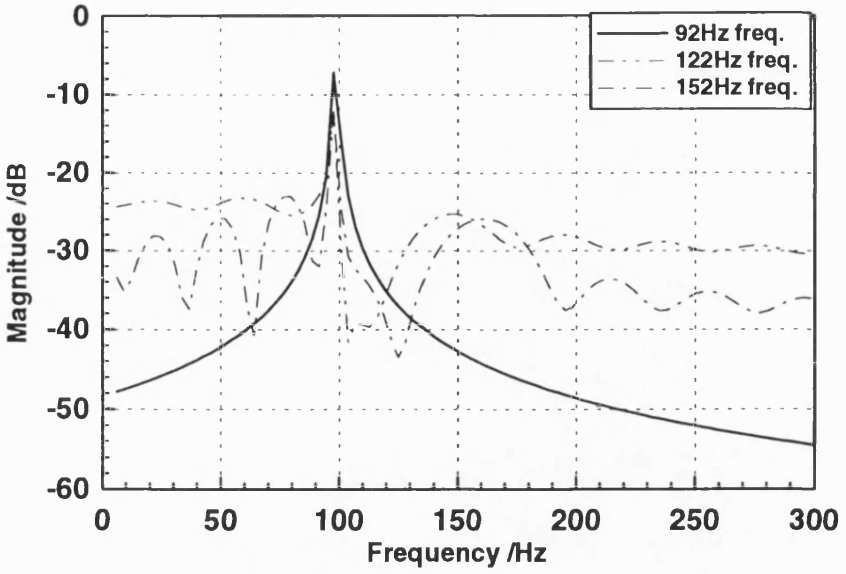

Figure 4.24: Inverse filter result for single frequency input at 92Hz, 122Hz and 152Hz. Filter set up for 92Hz input signal

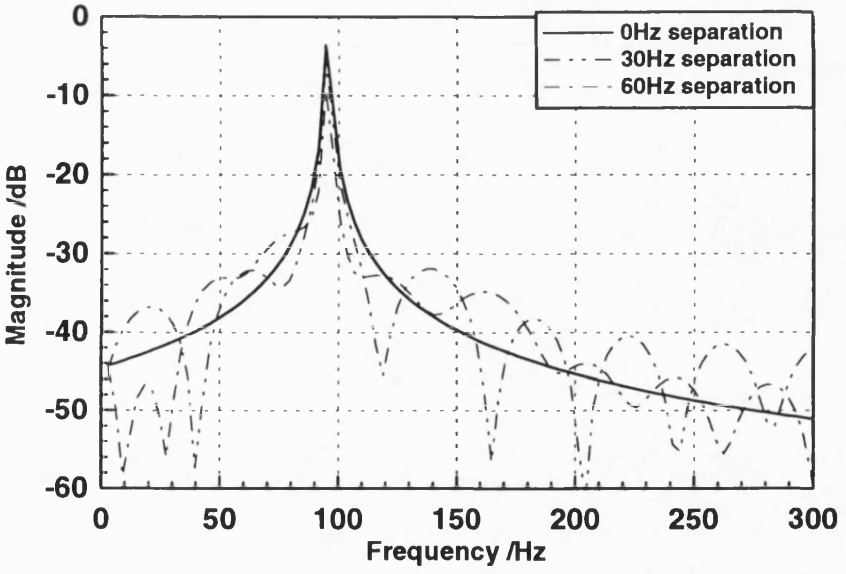

Figure 4.25: Inverse filter result for two input frequencies. Filter Set up frequency at 92Hz. Input signal frequencies are at 92Hz, 122Hz(— - - —); and at 92Hz, 152Hz(— - —)

peak at the filter set up frequency, and another peak position at the input signal frequency. The error in this peak compared to the input frequency increases as the separation between the two input signal frequency reduces. Therefore the use of the inverse filter in this manner is least useful for practical use as it always indicates a target at a frequency of 92Hz, rather that at the target frequency.

4.13.2 Matched Filter for White Noise

Matched filters [6] have been used in radar signal detection for many years to improve the signal-to-noise ratio. Usually the matched filter is applied in the time domain.

A matched filter is normally defined in terms of its impulse response, which always takes the forms of a time reversed version of the signal. Therefore such a filter is 'matched' to a particular signal waveshape—and to no other. The matched filter maximizes signal to noise ratio for a signal in the presence of white noise [6].

The transfer function is:

$$H(\omega) = G_a S^{\star}(\omega) \exp(-j\omega t_d)$$

where t_d is a time delay and $S(\omega)$ is the Fourier Transform of input signal $S(t)$.
G_a is constant equal to maximum filter gain(general taken to be unity) [7]. The matched filter transfer function is the complex conjugate of the signal transform with a linear phase shift introduced for physical realizability.

The conjugate of $S(\omega)$ means that the filter phase function differs from the signal phase function by only a minus sign. Thus the signal phase is perfectly compensated by the filter, and all frequency components add in phase, producing the maximum output at $t = t_d$. The output frequency distribution due to the signal $s(t)$ is

$$U(\omega) = H(\omega)S(\omega) = S^{\star}(\omega)S(\omega)\exp(-j\omega t_d) = |S(\omega)|^2 \exp(-j\omega t_d)$$

and is independent of the signal and filter phase function.

The filter introduces a phase shift into the noise components but does not change its random character, therefore the summing of these noise components remains random. The probability that the noise components at any given instant will sum in phase and produce a large output is minute. Hence the filter maximizes the signal to noise ratio.

Typical result from the matched filter are shown in Figure 4.26. This shows that the sidelobe is suppressed by about 7dB with respect to the main peak, thereby emphasising the main target response.

The results of the matched filter algorithm for processing real test data have been provided in Chapter 6.

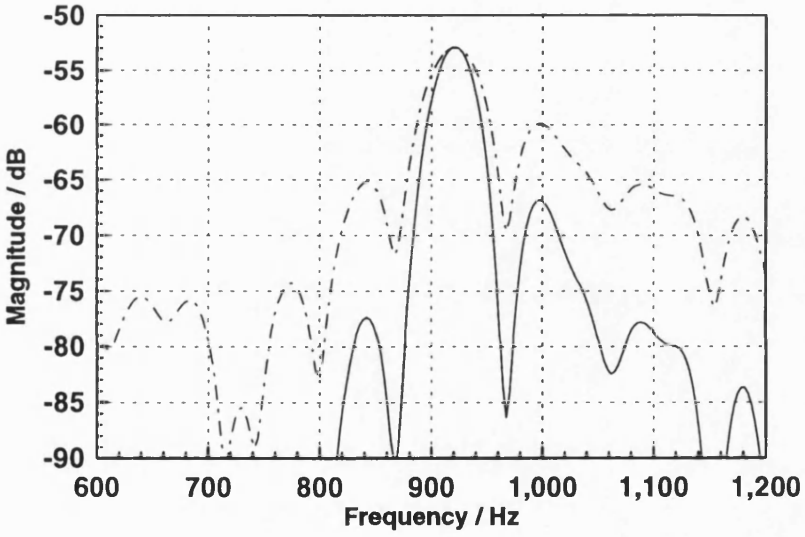

Figure 4.26: Matched filter results with measured data, (- - -) before filtering and (—) after filtering

4.13.3 Clutter Rejection Filter

Clutter is defined as unwanted return signals, such as cross coupling between transmitter and receiver in this project and reflections from minor targets. A clutter rejection

filter [5] has been used to reduce this kind of clutter which uses two filters cascaded together as seen in Figure 4.27. The input signal $x(t)$ is a signal $s_i(t)$ plus clutter $n_i(t)$.

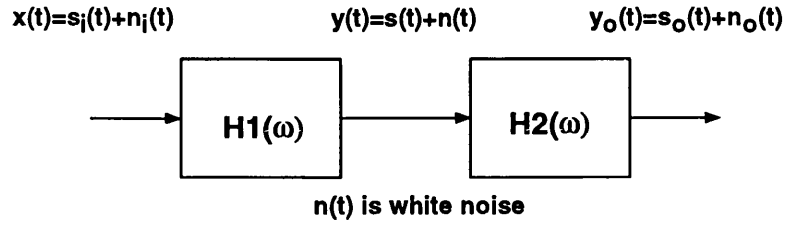

Figure 4.27: Matched filter for nonwhite noise

$N(\omega)$ is the clutter spectrum and then the power density spectrum $S_n(\omega)$ of the clutter is nonconstant.

$$S_n(\omega) = N(\omega)N^*(\omega) = |N(\omega)|^2$$

The first filter has the transfer function as

$$H_1(\omega) = K_1 \frac{1}{N(\omega)}$$

Which converts $N(\omega)$ to a constant power density spectrum $N_0/2$. The first filter is a inverse filter set up on $N(\omega)$. Then the output noise power density spectrum of the first filter becomes

$$S_n(\omega)K_1^2 \frac{1}{|N(\omega)|^2} = K_1^2$$

and the output signal of the first filter in the frequency domain is

$$H_1(\omega)S_i(\omega) = K_1 \frac{S_i(\omega)}{N(\omega)} = S(\omega)$$

Then we can detect signal under white noise $n(t)$ as described in previous section 4.13.2.

The optimum filter transfer function is then given by:

$$H_2(\omega) = K_2 S^*(\omega) \exp(-j\omega t_d) = K_1 K_2 \frac{S_i^*(\omega)}{N^*(\omega)} \exp(-j\omega t_d)$$

The overall transfer function is the cascade of $H_1(\omega)$ and $H_2(\omega)$ as:

$$H(\omega) = H_1(\omega)H_2(\omega) = K\frac{S_i^{\star}(\omega)}{S_n(\omega)}\exp(-j\omega t_d) \tag{4.21}$$

Therefore the transfer of the optimum filter for the signal corrupted by frequency-dependent noise is proportional to the complex conjugate of $S_i(\omega)$ and inversely proportional to the input clutter power density spectrum. This filter is described as the clutter rejection filter.

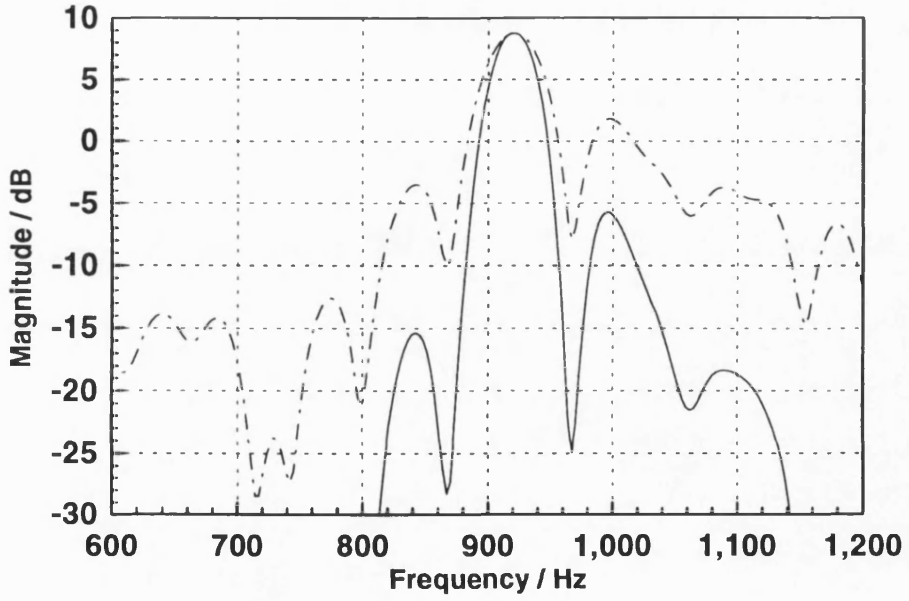

Figure 4.28: Clutter rejection filter for a tested data results, (- - -) before filtering and (—) after filtering

The results for real data from using clutter rejection filter are shown in Figure 4.28 and demonstrate that the spectral sidelobe is suppressed by about 7.8dB. In this example, the clutter rejection filter has been set up by using subtracted time domain test data, take FFT to get the conjugate spectrum of signal, divided by clutter power spectrum which is simulated by summing over a band frequencies signal which spread from 300Hz to 1200Hz and interval 30Hz.

The results of a clutter rejection filter applied on the real test data are given in

4.14 Synthetic Aperture Algorithm for FMCW Radar

The synthetic aperture technique is another well established technique which has been used on the pulse radar system for high resolution area mapping [8]. In 1994, Yamaguchi [9] reported using the synthetic aperture technique on an FMCW radar to improve the azimuth resolution of the image of an object buried in snow.

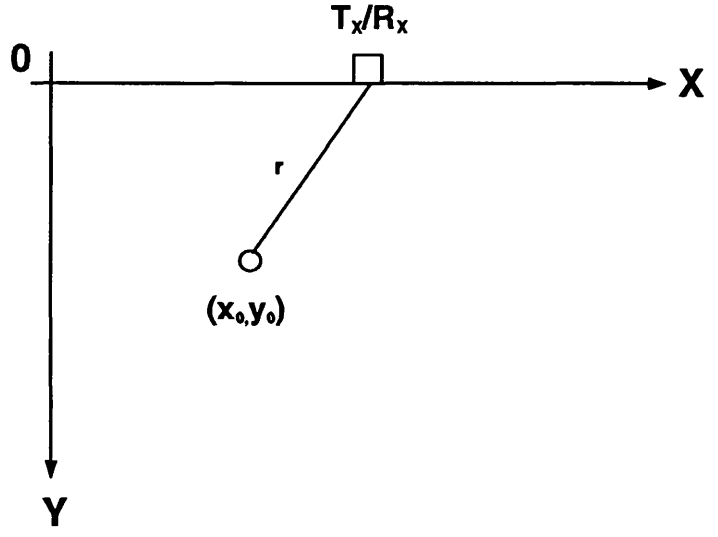

Figure 4.29: Position of point target and transmitter/receiver antenna

The principle of this application is based on the signal phase information. Suppose a single point target at (x_0, y_0) in the x,y coordinate as shown in Figure 4.29. Transmitter and receiver are at the same position and the distance to target is r. The transmitter emits a frequency modulated wave and a time delayed return signal has been received and mixed. Recall from Chapter 3, equation 3.11, the receiver mixer signal:

$$S(t) = Bg\cos\left(2\pi f_0\tau_d + \frac{2\pi\Delta f\tau_d}{T_s}t\right)$$

Where $g = g(x_0, y_0)$ is target distribution function. f_0 is the lower transmitted frequency, Δf is sweep frequency, τ_d is the time delay due to propagation, T_s is sweep time.

The Fourier Transform of the receiver mixer signal with respect to time $0 \leq t \leq T_s$ for the positive frequency domain is

$$S(f) = Bg \exp(2\pi f_0 \tau_d) \exp(j\pi f_d T_s - j\pi f T_s) \frac{\sin((\pi f_d - \pi f)T_s)}{(\pi f_d - \pi f)T_s} \tag{4.22}$$

Where

$$f_d = \frac{\Delta f}{T_s} \tau_d \tag{4.23}$$

is difference frequency.

the distance to the target can be approximated by:

$$r \simeq y_0 + \frac{(x - x_0)^2}{2y_0} \tag{4.24}$$

The time delay τ_d is therefore:

$$\tau_d = \frac{2n}{c} r \simeq \frac{2n}{c} \left(y_0 + \frac{(x - x_0)^2}{2y_0} \right)$$

n is refractive index.

Let $r \simeq y_0$ and substitute equation in 4.23 gives approximation for f_d,

$$f_d \simeq \frac{2n}{c} \frac{\Delta f}{T_s} y_0$$

Therefore:

$$\frac{\sin((\pi f_d - \pi f)T_s)}{(\pi f_d - \pi f)T_s} = \frac{\sin(\beta(y - y_0))}{\beta(y - y_0)}$$

Where

$$\beta = \frac{2\pi n \Delta f}{c}$$

Then Equation 4.22 becomes,

$$\begin{aligned} S(f) &\simeq S(x, y) \\ &= Bg(x_0, y_0) \exp(\frac{j4\pi n}{c} f_0 (y_0 + \frac{(x - x_0)^2}{2y_0})) \exp(-j\frac{2\pi n}{c} \Delta f (y - y_0)) \frac{\sin(\beta(y - y_0))}{\beta(y - y_0)} \end{aligned}$$

Using $h_1(x-x_0,y_0)$, $h_2(y-y_0)$, $f(y-y_0)$ substitute in the above equation:

$$h_1(x-x_0,y_0)=\exp\left[\frac{j4\pi n}{c}f_0(y_0+\frac{(x-x_0)^2}{2y_0})\right]$$

$$h_2(y-y_0)=\exp\left(-j\frac{2\pi n}{c}\Delta f(y-y_0)\right)$$

$$f(y-y_0)=\frac{\sin(\beta(y-y_0))}{\beta(y-y_0)}$$

Here $f(y-y_0)$ is the range function in the y direction. $h_1(x-x_0,y_0)$, $h_2(y-y_0)$ are the phase functions. Then

$$U(x,y)=Bg(x_0,y_0)h_1(x-x_0,y_0)h_2(y-y_0)f(y-y_0)$$

$U(x,y)$ is the space variable function. For a two dimensional distributions target the above equation can be modified as:

$$U(x,y)=B\int_0^{\infty}\int_{-\infty}^{\infty}f(y-y_0)g(x_0,y_0)h_1(x-x_0,y_0)h_2(y-y_0)dx_0dy_0$$

At $y=y_0$:

$$h2(y-y_0)=1$$

$$f(y-y_0)=1$$

Then

$$U(x,y_0)=B\int_{-\infty}^{\infty}g(x_0,y_0)h_1(x_0-x,y_0)dx$$

$$g(x_0,y_0)=\int_0^{L}U(x,y_0)h_1^{\star}(x_0-x,y_0)dx \tag{4.25}$$

where L is the scan width in the azimuth direction. This equation establishes the basis for the synthetic aperture FMCW radar principle. The radar image can be obtained by changing x_0,y_0 and calculating Equation 4.25 or calculating by Fourier Transform.

Synthetic aperture algorithms for processing simulated and real test data have been carried out by C programs to calculate the integral of Equation 4.25 directly. These results have been provided in Chapter 5 and Chapter 6. In these program the calcu-

lation of target distance is used the exact equation 4.26 rather than the approximated equation 4.24.

$$r = \sqrt{y_0^2 + \left(\frac{D}{2} - (x - x_0)\right)^2} + \sqrt{y_0^2 + \left(\frac{D}{2} + (x - x_0)\right)^2} \tag{4.26}$$

where D is the separation between T_X to R_X as shown in Figure 4.4. When the target is shallower, the approximated equation has significant error, so it can't be used in calculating synthetic aperture. The simulated data synthetic aperture results show a improved horizontal resolution. The effect of varying refractive index and cross coupling level on the synthetic aperture processing has also been provided in Chapter 5 and 6.

4.15 Conclusion

This chapter has reviewed the target analysis model development and provided the mathematical detail of FFT algorithm and convolution algorithm.

The safe digging depth formula have been derived and the quantisation error caused by FFT resolution has been studied and some methods to reduce quantisation error have been proposed.

The measurement unit movement algorithm has been provided by using peak information from individual channel spectra and convolved spectra.

Other algorithms to improve detection resolution have been investigated. Window function applied on the spectrum can suppress the spectrum sidelobes but broadens the main peak. This decreases the ability to separate two close targets. This method is not suitable for the real system.

Target templating algorithms have been studied by using $\frac{\sin x}{x}$ as template function and derived template functions to give delta or triangle output signal. The results have shown that templating with $\frac{\sin x}{x}$ will still produce the typical $\frac{\sin x}{x}$ output, but does not sharpen the output peak. Triangle templating can produce a very sharp peak but its application is limited for the case where the separation of two target is less than their $3dB$ bandwidth.

A reference signal subtraction method has been studied and the results show that using real tested data as reference can remove the majority of the clutter, but using $\frac{\sin x}{x}$ as reference did not. The results of reference signal subtraction algorithm applied on the real data have been provided in Chapter 6.

Different filter algorithms have been studied. Inverse filter has similar results with triangle templating, it is not suitable for practical use. Matched filter for white noise and clutter rejection filter have been derived. The results show some benefits in suppressing spectrum sidelobe and narrowing the main lobe from matched filter and clutter rejection filter, the results and discussion of these filter algorithm applied on the real test data have been given in Chapter 6.

The principles of synthetic aperture algorithm applied on FMCW radar has been reviewed. The simulated and practical results have been provided in later Chapters.

References

[1] William H. *Numerical Recipes in C.* Cambridge University Press, 1992.

[2] Stearns K F. *Digital Signal Analysis.* Hayden Book Company, Inc., 1975.

[3] Martin J D. *Signal & Processing a Foundation Course.* Pitman Publishing, 1991.

[4] Dahlquist G. *Numberical Methods.* Prentice-Hall, Inc, 1974.

[5] Difranco J V. *Radar Detection.* Artech House, Inc., 1980.

[6] Blinchikoff H J and Zverev A I. *Filtering in the Time and Frequency Domains.* John Wiley & Sons, Inc., 1975.

[7] Skolnik M I. *Introduction to Radar Systems.* Mcgraw-Hill, Inc, 1962.

[8] Osumi N and Ueno K. Synthetic aperture approach to underground pulse-radar imaging. In Musha T et al., editor, *International Symposium on Noise and Clutter Rejection in Radars and Imaging Sensors (INSCR)*, volume 1, pages 667–672. IECE, 1984. Author(s) with Nippon Telegraph and Telephone, Japan.

[9] Yamaguchi Y et al. Synthetic aperture fm-cw radar applied to the detection of objects buried in snowpack. In *IEEE Transactions on Geoscience and Remote Sensing*, volume GE-32(1), pages 11–18, January 1994. Author(s) with Niigata University, Japan.

Chapter 5

Simulation Model Results

5.1 Outline

This chapter summarises the safe digging depth and unit movement results obtained from the signal processing mathematical model. The cases examined are for a single target, and twin targets of different sizes and depths. These are placed in uniform, layered and trenched media.

Work on the signal processing mathematical model has also included the development of a number of tests that can be used to study the resolution performance of various target analysis algorithms.

5.2 Signal Processing Mathematical Model

Mathematical modelling of the signal processing provides some prediction of how the system will react to realistic situations.

The procedures used in the simulation software are as shown in Figure 5.1. User defined target position in (x-y) coordinates are fixed, and the measurement unit's position shifted along the x axis from left to right. For each measurement point, the software

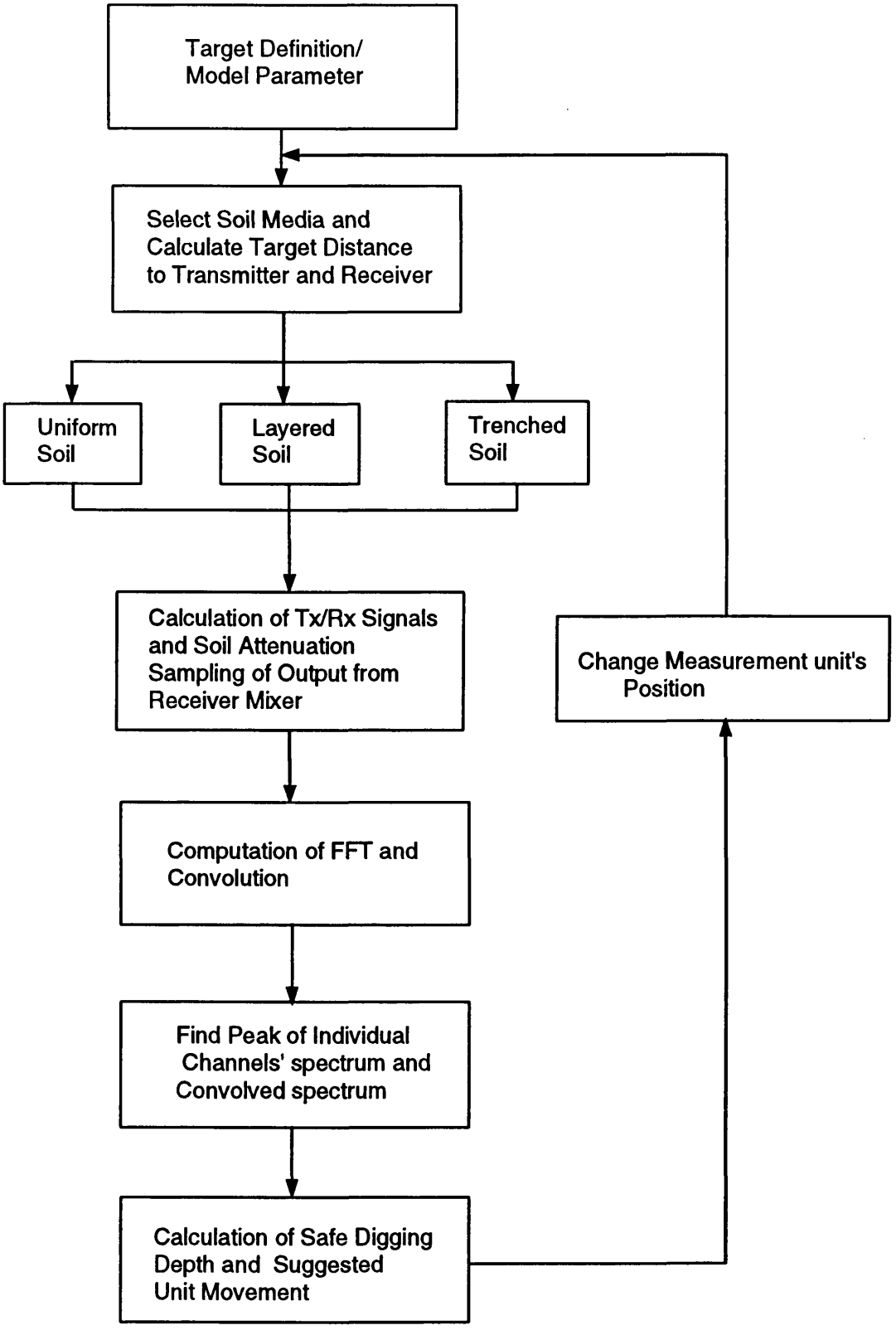

Figure 5.1: Signal processing mathematical model procedure

calculates the target distance to each pair of transmitter and receiver antennas in the user selected infill media: that is uniform, layered and trenched. The software computes the transmitter and receiver signals and infill attenuation, then mixes the transmitter and receiver signals to produce the audio-band difference frequency which is then sampled. The FFT algorithm is applied and convolution is taken on the pair of channel returns. Using the peak information of individual channels and convolved spectrum, the safe digging depth(SDD) and the required unit movement to position it above the target are calculated.

The program then changes the measurement unit's position and repeats the above steps to calculate the safe digging depth and unit movement for the next point.

The mathematical model has been written in Microsoft QuickBasic and has been compiled as an executable file which can be run on any IBM compatible personal computer.

The simulations of representative target situations use the following values for the system parameters:

Target Simulation	
Sweep Range	250MHz to 750MHz
Sweep Time	5 ms
Frequency Difference per ns Delay	100 Hz/ns
Repetition Time	327.68 ms
Frequency Component Spacing	3.052 Hz
No. of Time Samples	2048
Sampling Frequency	6250 Hz

Target Analysis	
FFT Resolution	3.052 Hz
Maximum Unaliased Frequency	3125 Hz

5.3 Simulations of Representative Target Situations

The results show the computed unit movement and the safe digging depth for each case considered. It should be noted that the unit movement arrows are constantly shown to the operator, whereas the safe digging depth is only indicated when the unit is positioned directly above a target.

5.3.1 Single Target

The results for a single 3″ diameter target 0.7m deep, 2.5m offset are shown in Figure 5.2 for uniform, layered and trenched media. The results indicate a smooth variation in safe digging depth for movements around the centerline of the target at 2.5m offset. The trenched media in this case provides a sharper indication of target position than the uniform or layered media. The trenched media also indicates a shallower safe digging depth (0.608m) than the other media types while the safe digging depth for uniform and layered media are 0.625m and 0.632m respectively.

5.3.2 Two Targets

Two Identical Targets at the Same Depth

The results for two identical 3″ diameter targets, buried with 2.25m and 2.75m offset and 0.5m below the surface are shown in Figure 5.3 for uniform, layered and trenched media. The results indicate that the unit computes a correct safe digging depth when the movement arrows indicate that the unit is directly over a target. A "ghost" target is also indicated and is positioned symmetrically between the actual targets at an offset of 2.5m. The trenched media indicates a safe digging depth of 0.4m while the safe digging depth for uniform and layered media are 0.38m and 0.42m respectively. The trenched media also indicates a broader "ghost" target response than the layered media, with the uniform media appearing to minimise the distance that the unit is centred over the "ghost" target whilst maximising the distance the unit is centred over the real targets. The trenched and layered targets however introduce horizontal offsets in the target

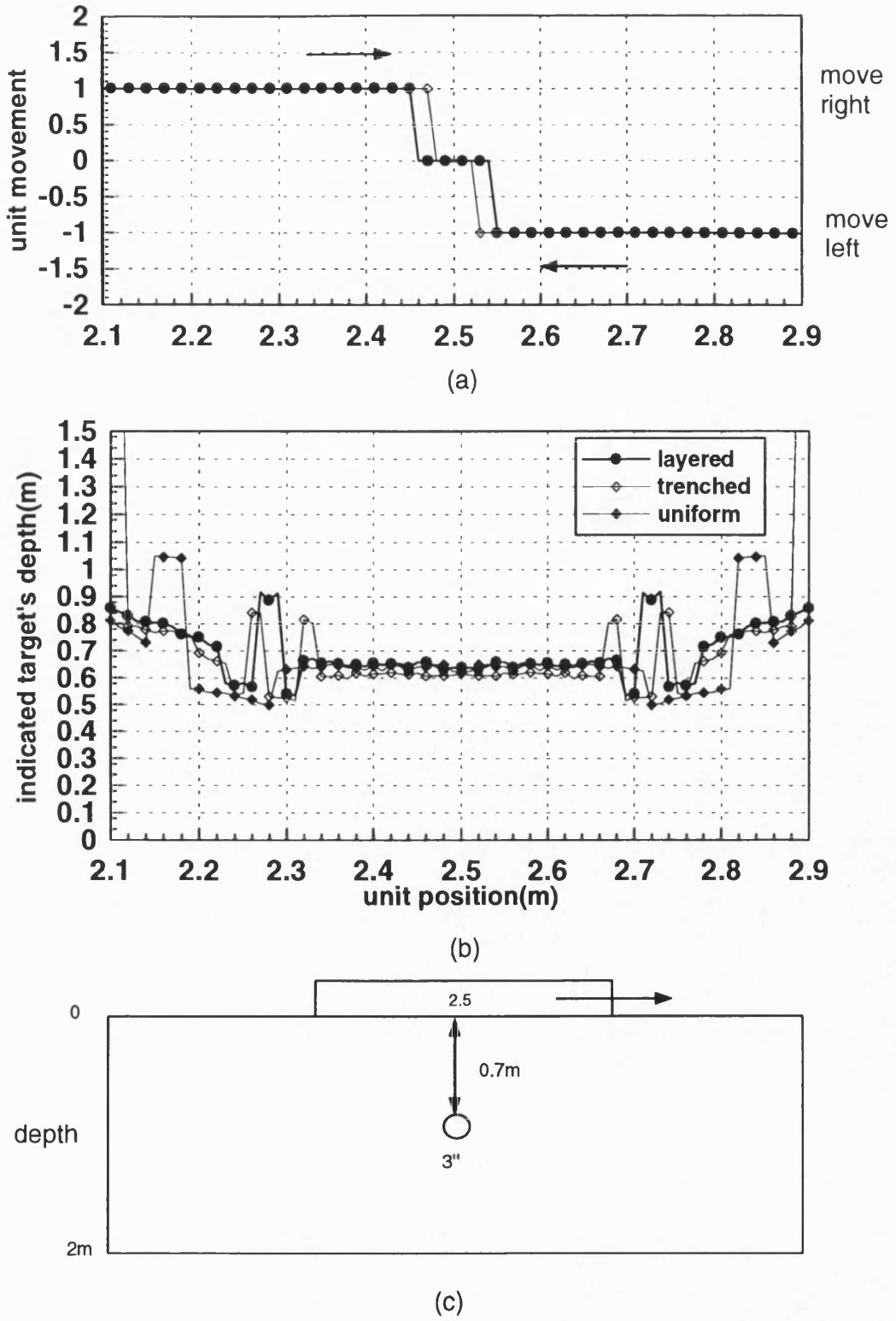

Figure 5.2: (a) Indicated movement of unit; (b) Indicated target depth; and (c) Actual depth; versus unit position for a 3″ single target 0.7m deep at a 2.5m offset in uniform, layered and trenched media (refer to Figure 3.9)

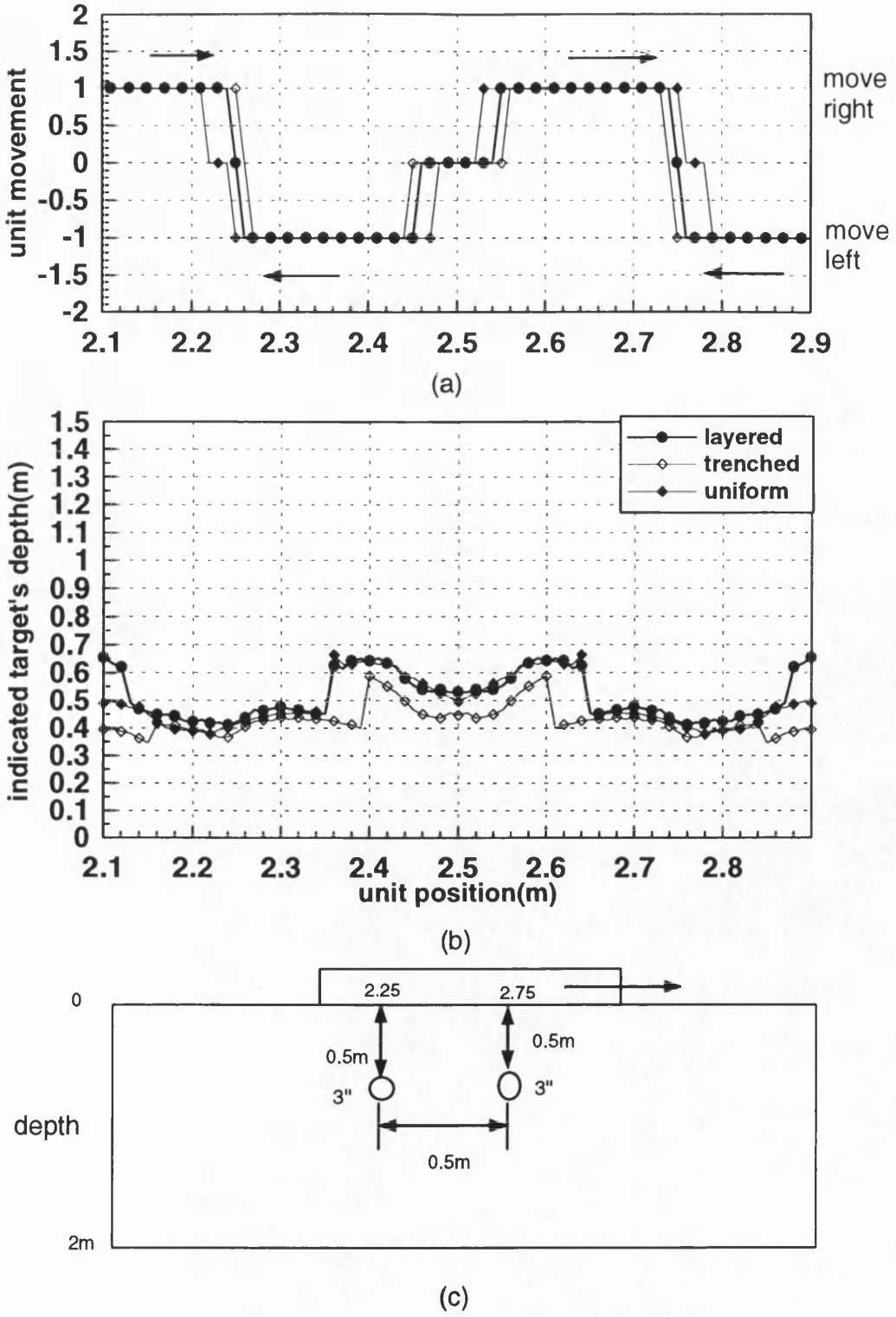

Figure 5.3: (a) Indicated movement of unit; (b) Indicated target depth; and (c) Actual depth; versus unit position for two 3″ targets 0.5m deep with offsets of 2.25m and 2.75m in uniform, layered and trenched media (refer to Figure 3.9)

positions. In all the cases the unit operator would identify the "ghost" target at 2.5m since the unit movement arrows would always indicate that the unit should be moved towards one of the real targets.

Two Identical Targets at Different Depths

The results for two identical 3″ diameter, 2.25m and 2.75m offset targets at depths of 0.5m and 1.0m are shown in Figure 5.4 for uniform, layered and trenched media. The results indicate that the safe digging depth for the shallowest target can be calculated correctly in the presence of the deeper target. The results again show a variation in the horizontal position of the shallowest target, with the uniform media providing the broadest horizontal distance that the system indicates a target is on the unit centerline. The trenched media also again shows the largest underestimate in safe digging depth, providing a safe digging depth of 0.407m - 0.414m.

Two Different Targets at Different Depths with a Large, Shallow Target

The results for a 3″ diameter, 2.25m offset target 1.0m below the surface and a 6″ diameter, 2.75m offset target 0.5m below the surface are shown in Figure 5.5 for uniform, layered and trenched media. The results indicate that the unit correctly determines the safe digging depth for the shallow object, however, the unit is not sufficiently sensitive to detect the smaller object at a depth of 1.0m. The variations in unit movement are again similar to those effects seen with two identical targets at different depths.

Two Different Targets at Different Depths with a Small, Shallow Target

The results for a 6″ diameter, 2.25m offset target 1.0m below the surface and a 3″ diameter, 2.75m offset target 0.5m below the surface are shown in Figure 5.6 for uniform, layered and trenched media. The results indicate that the unit correctly determines the safe digging depth for the shallowest object, however, the unit is also able to detect the deeper, larger object. The movement arrows in this case always indicate that the operator should move the unit to centre it above the shallow target. The uniform media

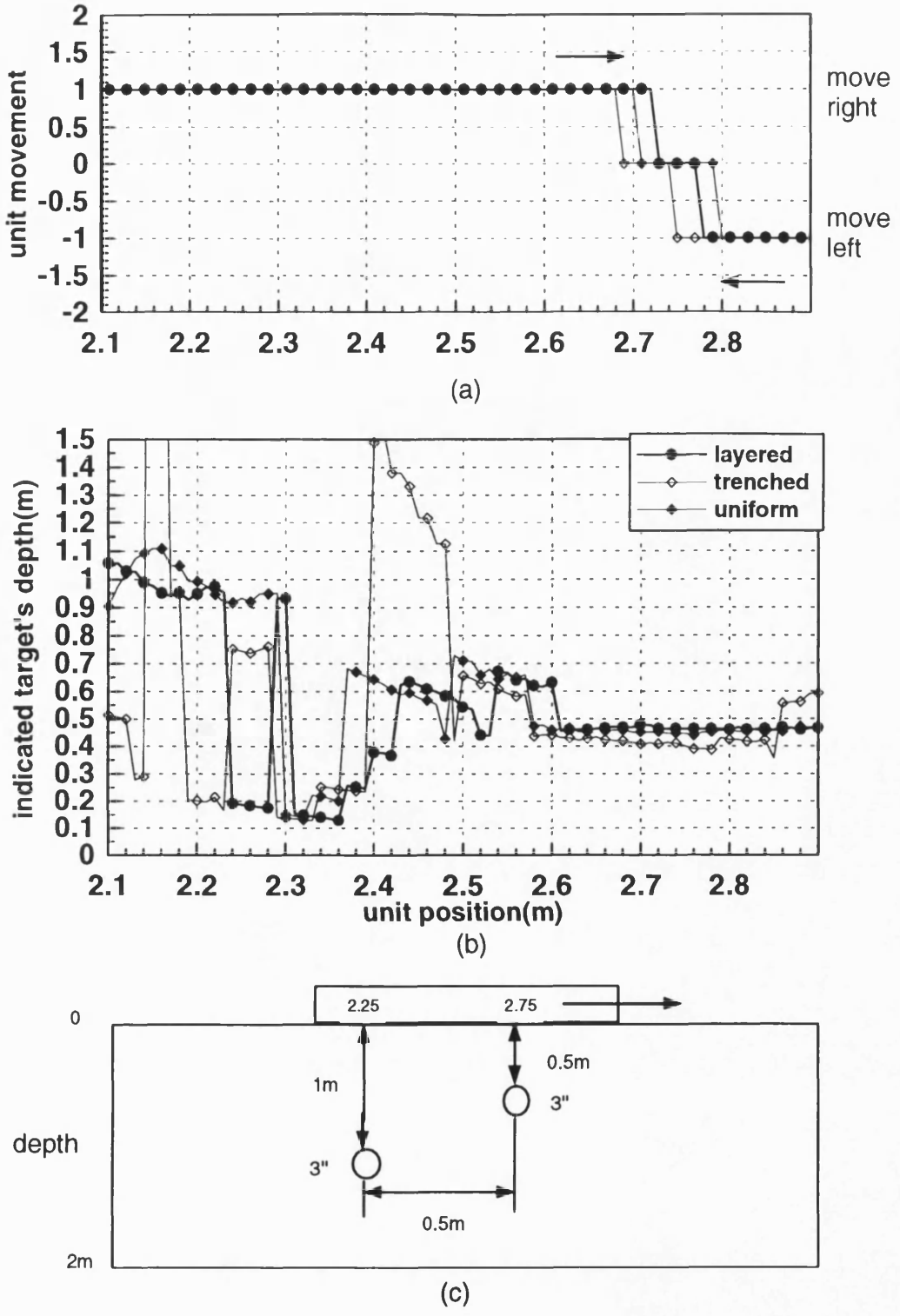

Figure 5.4: (a) Indicated movement of unit; (b) Indicated target depth; and (c) Actual depth; versus unit position for and a 3″ targets 1.0m Deep with a 2.25m Offset and a 3″ targets 0.5m Deep with a 2.75m Offset in uniform, layered and trenched media (refer to Figure 3.9)

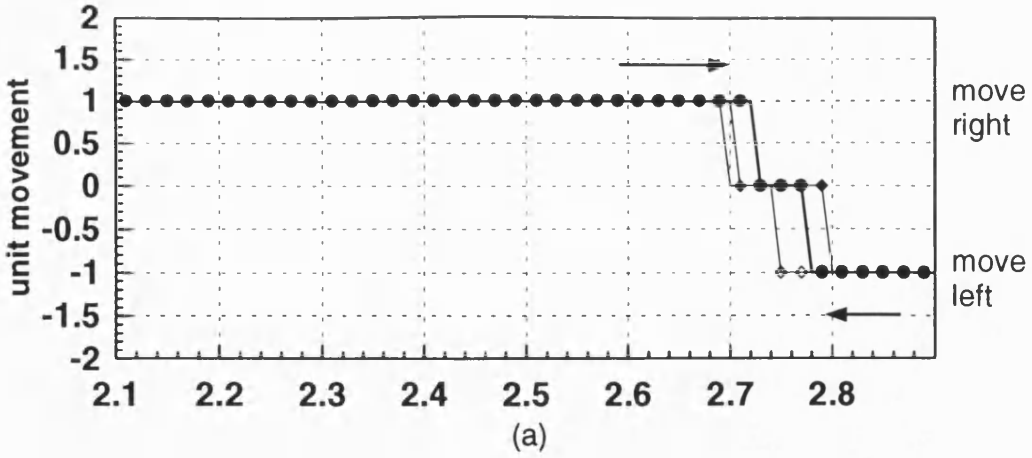

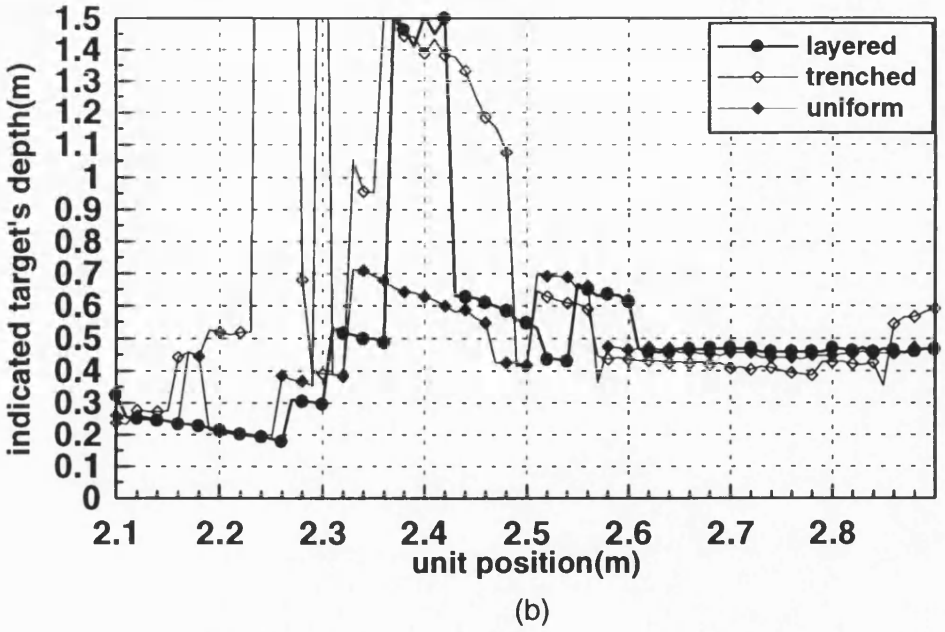

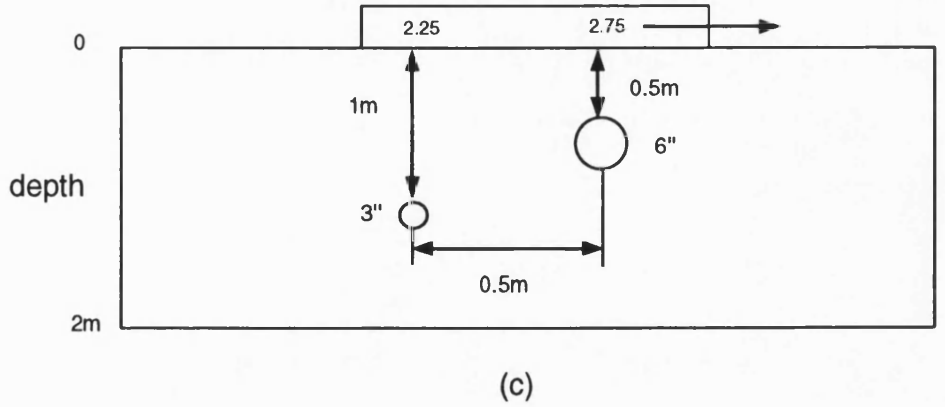

Figure 5.5: (a) Indicated movement of unit; (b) Indicated target depth; and (c) Actual depth; versus unit position for and a 3″ targets 1.0m deep with a 2.25m offset and a 6″ targets 0.5m deep with a 2.75m offset in uniform, layered and trenched media (refer to Figure 3.9)

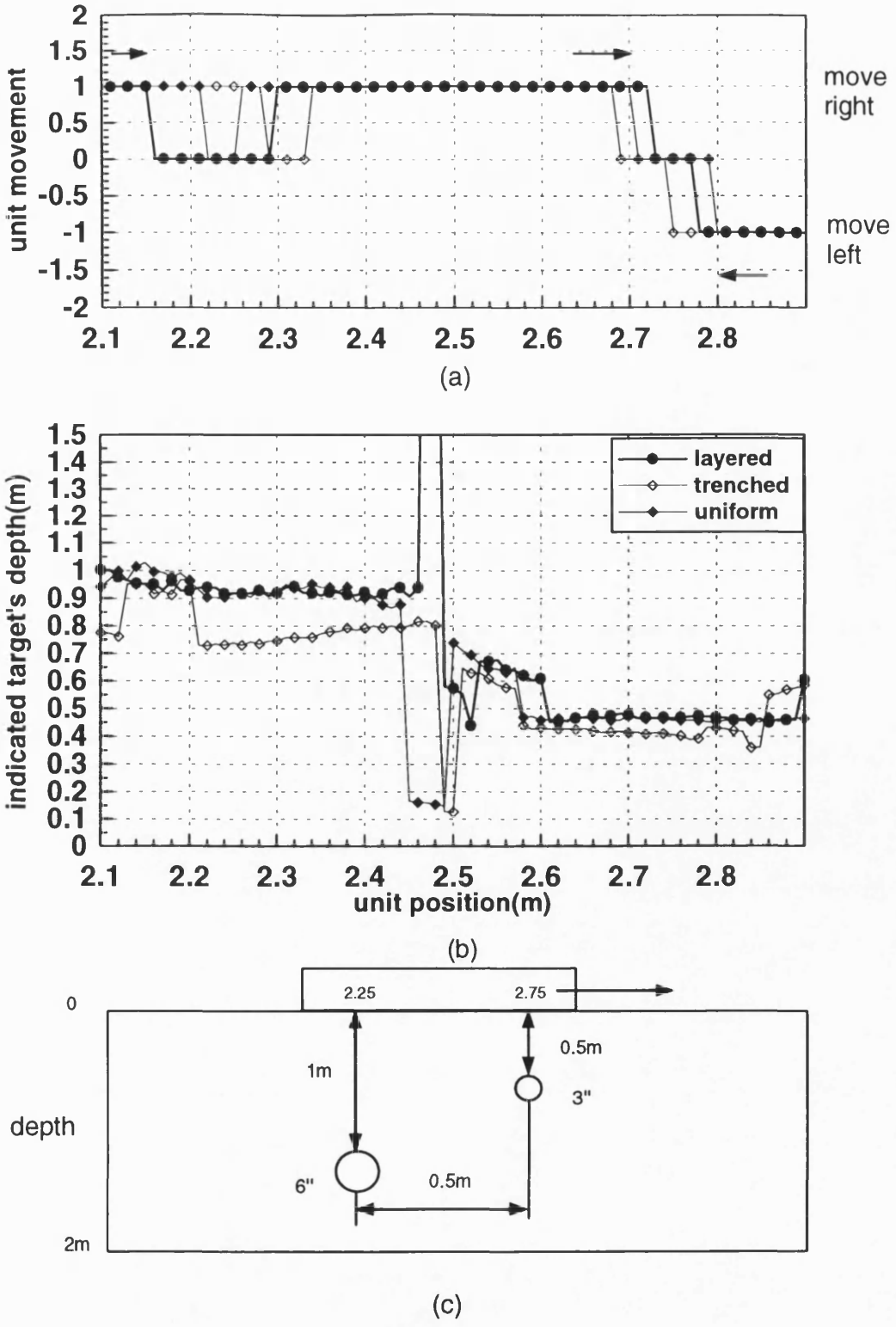

Figure 5.6: (a) Indicated movement of unit; (b) Indicated target depth; and (c) Actual depth; versus unit position for and a 6" targets 1.0m deep with a 2.25m offset and a 3" targets 0.5m deep with a 2.75m offset in uniform, layered and trenched media (refer to Figure 3.9)

results also indicate the broadest range of horizontal distances that the unit is centred over the shallow target, although the sharpest response is found over the secondary, interfering target. The trenched media provides the greatest horizontal shift in the target centre position.

5.3.3 Summary of Results for Uniform, Layered and Trenched Media

The accuracy of the unit movement and safe digging depth calculations has been summarised in the following tables. The target cases refer to the target configurations for uniform, layered and trenched media shown in Figure 5.7, 5.8, 5.9. Table 5.1, 5.2, 5.3 provides the comparison of safe digging depth and actual depth, comparison of indicated position and actual position for targets in uniform, layered and trenched soil respectively.

The target simulation and analysis results indicate a number of trends in the safe digging depth and unit movement calculations. The unit movement results indicate that for uniform media, in general, the unit is positioned within 4cm of the target centerline. The layered media results indicate the unit should be positioned within 2cm of the target centerline. The trenched media results show similar results to the layered media case, but with a 2cm offset both sides. The higher accuracy of the layered media is due to the focussing effects of the dielectric profile. The offset in the trenched media results can be attributed to the vertical discontinuity in the infill which will affect the horizontal position calculation due to differential delay.

The safe digging depth calculations consistently provide a safe depth indication. However the difference between actual and computed depth varies, as expected, between target cases. Trenched media simulations have shown the largest difference since the refractive index profile used provides the largest variation between the direct path, and the ray path between the unit and the target. In all the tests, the unit provided a safe digging depth which was less than the actual depth of the target.

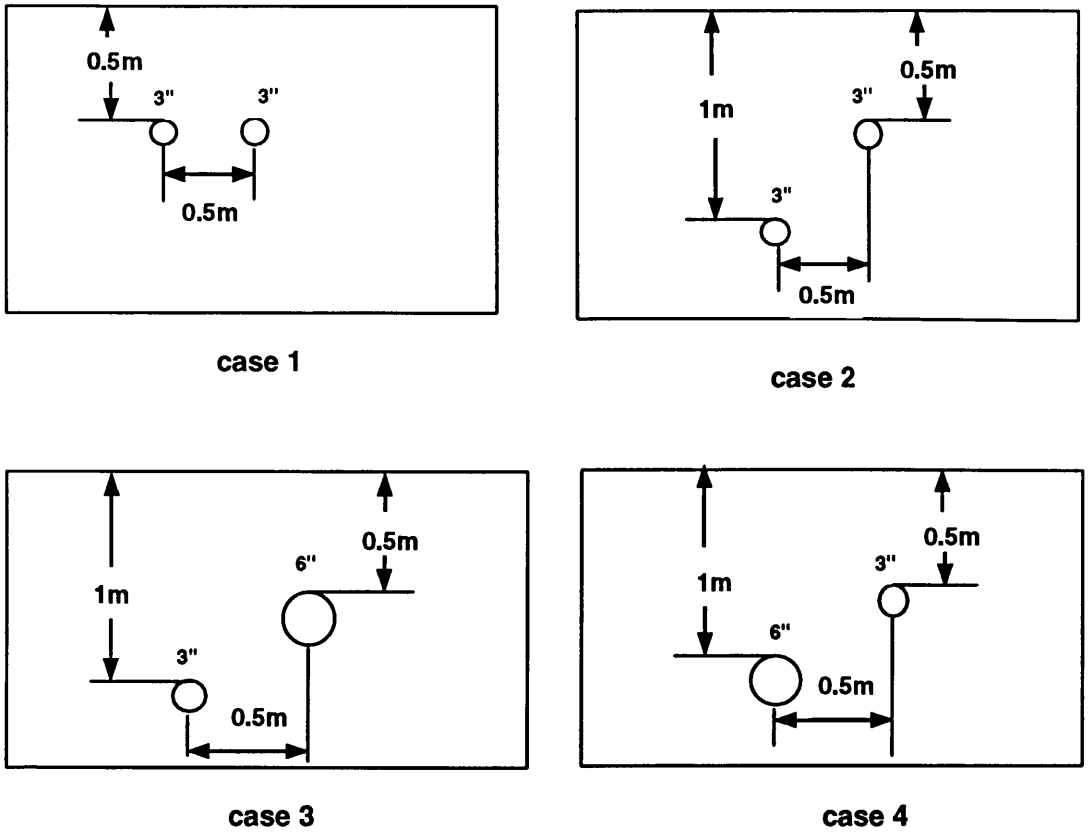

Figure 5.7: Target configurations used in the testing of the target analysis algorithms for uniform soil

	Safe Digging Depth (metres)	Actual Depth (metres)	Difference (metres)
Single target	0.625 - 0.649	0.7	0.075 - 0.051
Two targets, Case 1	0.377 - 0.400	0.5	0.123 - 0.100
Two targets, Case 2	0.439 - 0.456	0.5	0.061 - 0.044
Two targets, Case 3	0.435 - 0.456	0.5	0.065 - 0.044
Two targets, Case 4	0.451 - 0.463	0.5	0.049 - 0.037

	Indicated Position (metres)	Actual Position (metres)	Difference (metres)
Single target	2.46 - 2.54	2.5	-0.04 - +0.04
Two targets, Case 1	2.22 - 2.24	2.25	-0.03 - -0.01
Two targets, Case 2	2.71 - 2.79	2.75	-0.04 - +0.04
Two targets, Case 3	2.71 - 2.79	2.75	-0.04 - +0.04
Two targets, Case 4	2.71 - 2.79	2.75	-0.04 - +0.04

Table 5.1: Comparison of safe digging depth and actual depth and comparison of indicated position and actual position for targets in uniform soil

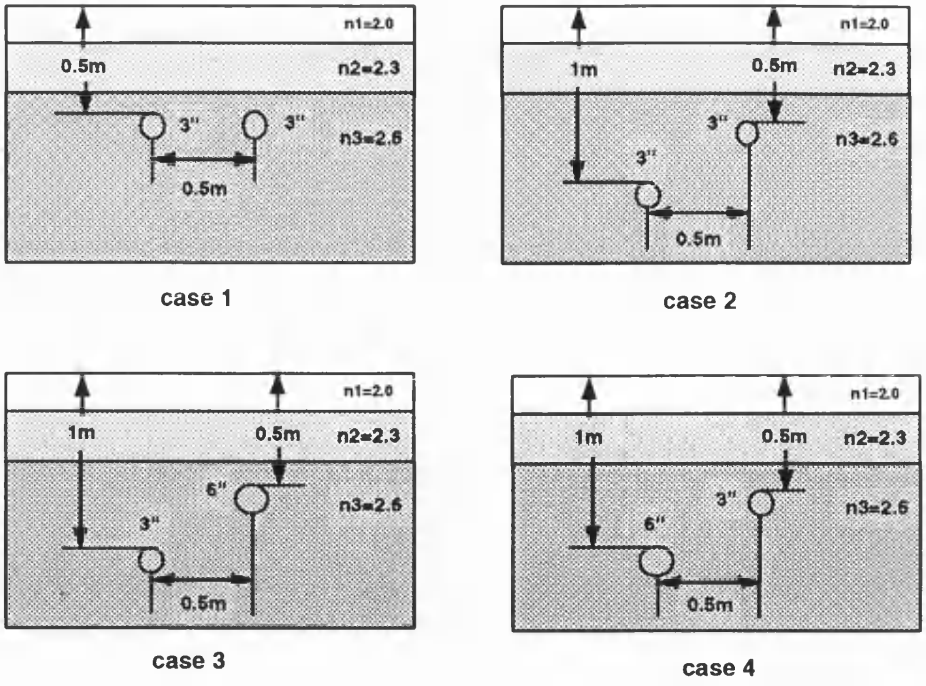

Figure 5.8: Target configurations used in the testing of the target analysis algorithms for layered Soil

	Safe Digging Depth (metres)	Actual Depth (metres)	Difference (metres)
Single target	0.632 - 0.658	0.7	0.068 - 0.042
Two targets, Case 1	0.423	0.5	0.077
Two targets, Case 2	0.462	0.5	0.038
Two targets, Case 3	0.458	0.5	0.042
Two targets, Case 4	0.466 - 0.471	0.5	0.034 - 0.029

	Indicated Position (metres)	Actual Position (metres)	Difference (metres)
Single target	2.46 - 2.54	2.5	-0.04 - +0.04
Two targets, Case 1	2.25	2.25	0.00
Two targets, Case 2	2.73 - 2.77	2.75	-0.02 - +0.02
Two targets, Case 3	2.73 - 2.77	2.75	-0.02 - +0.02
Two targets, Case 4	2.73 - 2.77	2.75	-0.02 - +0.02

Table 5.2: Comparison of safe digging depth and actual depth and comparison of indicated position and actual position for targets in layered soil

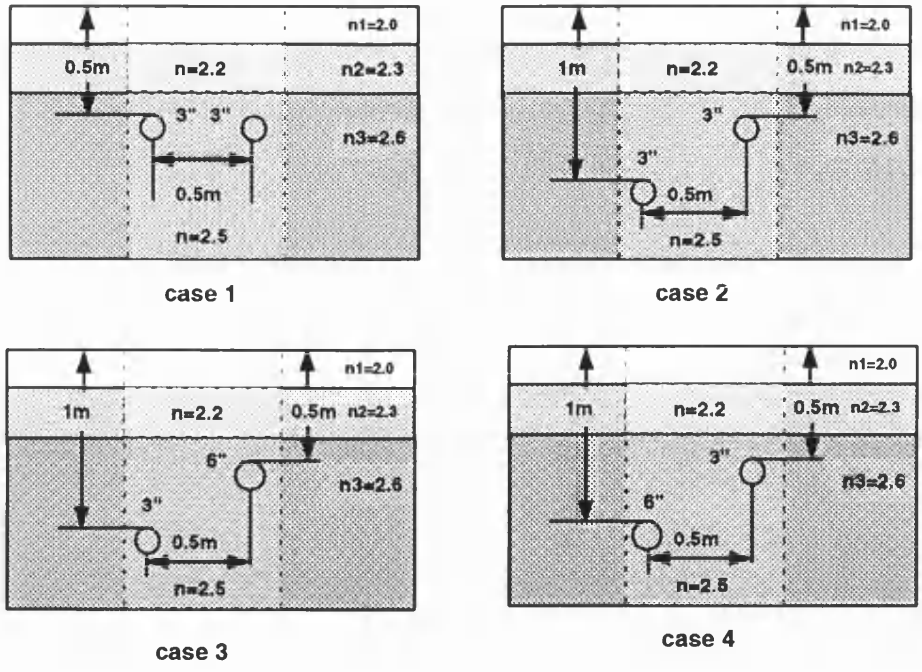

Figure 5.9: Target configurations used in the testing of the target analysis algorithms for trenched soil

	Safe Digging Depth (metres)	Actual Depth (metres)	Difference (metres)
Single target	0.608 - 0.617	0.7	0.092 - 0.083
Two targets, Case 1	0.405	0.5	0.095
Two targets, Case 2	0.407 - 0.414	0.5	0.093 - 0.086
Two targets, Case 3	0.404 - 0.412	0.5	0.096 - 0.088
Two targets, Case 4	0.407 - 0.418	0.5	0.093 - 0.082

	Indicated Position (metres)	Actual Position (metres)	Difference (metres)
Single target	2.48 - 2.52	2.5	-0.02 - +0.02
Two targets, Case 1	2.26	2.25	+0.01
Two targets, Case 2	2.69 - 2.74	2.73	-0.06 - -0.01
Two targets, Case 3	2.70 - 2.74	2.73	-0.05 - -0.01
Two targets, Case 4	2.69 - 2.74	2.73	-0.06 - -0.01

Table 5.3: Comparison of safe digging depth and actual depth and comparison of indicated position and actual position for targets in trenched soil

The differences are affected by two other factors, in addition to the increase in time delay due to the ray path in the media. The threshold value which is used to provide a consistently shallow depth reading will account for a given depth difference. The interaction of target responses will also combine with the use of a threshold value to produce an additional error. This is illustrated by two identical targets at the same depth (Case 1) where target interaction is significant, and leads to the largest differences between actual and computed target depth for each media type.

5.4 Target Analysis Algorithm Resolution Studies

The aim of this work has been to formulate a number of simulation tests that can be used to determine the horizontal and vertical resolutions of the target analysis algorithms, hence providing a check on the algorithm performance.

5.4.1 Horizontal Resolution Study

The results discussed in the previous section have shown that for two identical targets at the same depth, a "ghost" target is indicated in addition to the actual targets. The computed depth of the "ghost" target will influence the system performance if it registers a significant shallow target as the separation of the real targets is varied.

An investigation was therefore carried out into the computed depth of the "ghost" and actual targets as the separation between the identical targets was varied between 1cm and 1.1 metres in uniform soil. Figure 5.10 shows the variation in the computed safe digging depth for both the actual and "ghost" targets. Each pair of points is obtained from a computation similar to that shown in Figure 5.3, with the safe digging depths plotted when the unit is centred over a "target". The symmetrical nature of the study means that the computed safe digging depths for the two real targets are identical.

The investigation also enables the resolution of the target analysis algorithm to be studied, with the determination of the separation below which the two separate targets cannot be resolved.

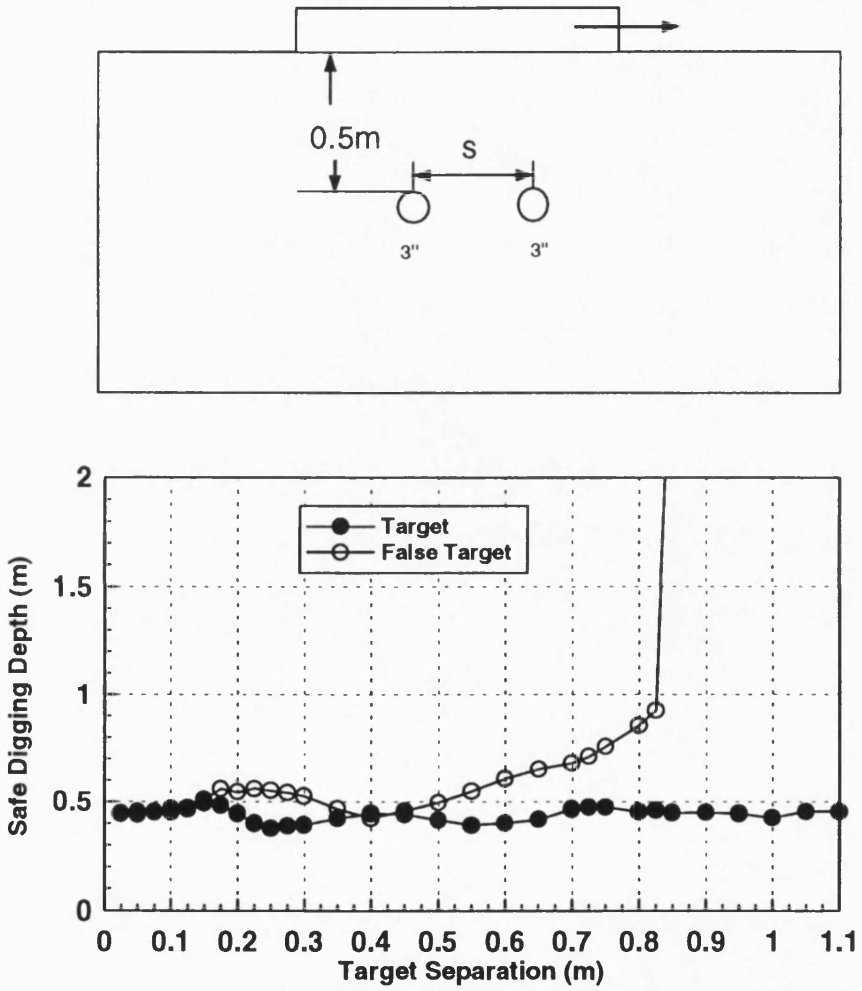

Figure 5.10: Computed safe digging depth of the real targets (•) and "ghost" target (○) versus target separation for two 3″ targets at a depth of 0.5m in uniform soil

The results of the study show that the computed safe digging depth of the "ghost" target is consistently greater than the safe digging depth of the real target. The depth of the "ghost" target rapidly increases as the separation of the targets increases and the target interaction decreases.

The safe digging depths of the real targets should ideally be constant across the range of separations, however the results show that there is a variation of up to 15cm with the targets at 0.5m. This is due to the interaction of the two target responses and the timing quantisation errors, which have been discussed in Chapter 4, Section 4.6. In the case of very small separations less than 0.2m the "ghost" and real target safe digging depths converge indicating that the resolution limit of the algorithm is being approached. The resolution limit was determined from the data as a horizontal separation of 15cm.

5.4.2 Vertical Resolution Study

A further study has also been carried out into the vertical resolution of the target analysis algorithms using the test situation shown in Figure 5.11. The aim of this test is to quantify the effect of the deeper target on the computed safe digging depth of the target at 0.5m.

The results indicate that for all target separations the algorithm correctly computes the safe digging depth, however the interaction between the targets results in a variation of up to 10cm in safe digging depths for target separations under 15cm. Although for very small target separations (less than 5cm) the variation is considerably smaller accepting that this scenario is theoretical and would not occur in practice.

5.4.3 Offset Vertical Resolution Study

The aim of this study is to quantify the effect of target interaction when there are multiple targets of different sizes at different depth.

The results illustrate a small variation in the safe digging depth of the shallowest target at 0.5m for a large range of separations. The target analysis algorithms consis-

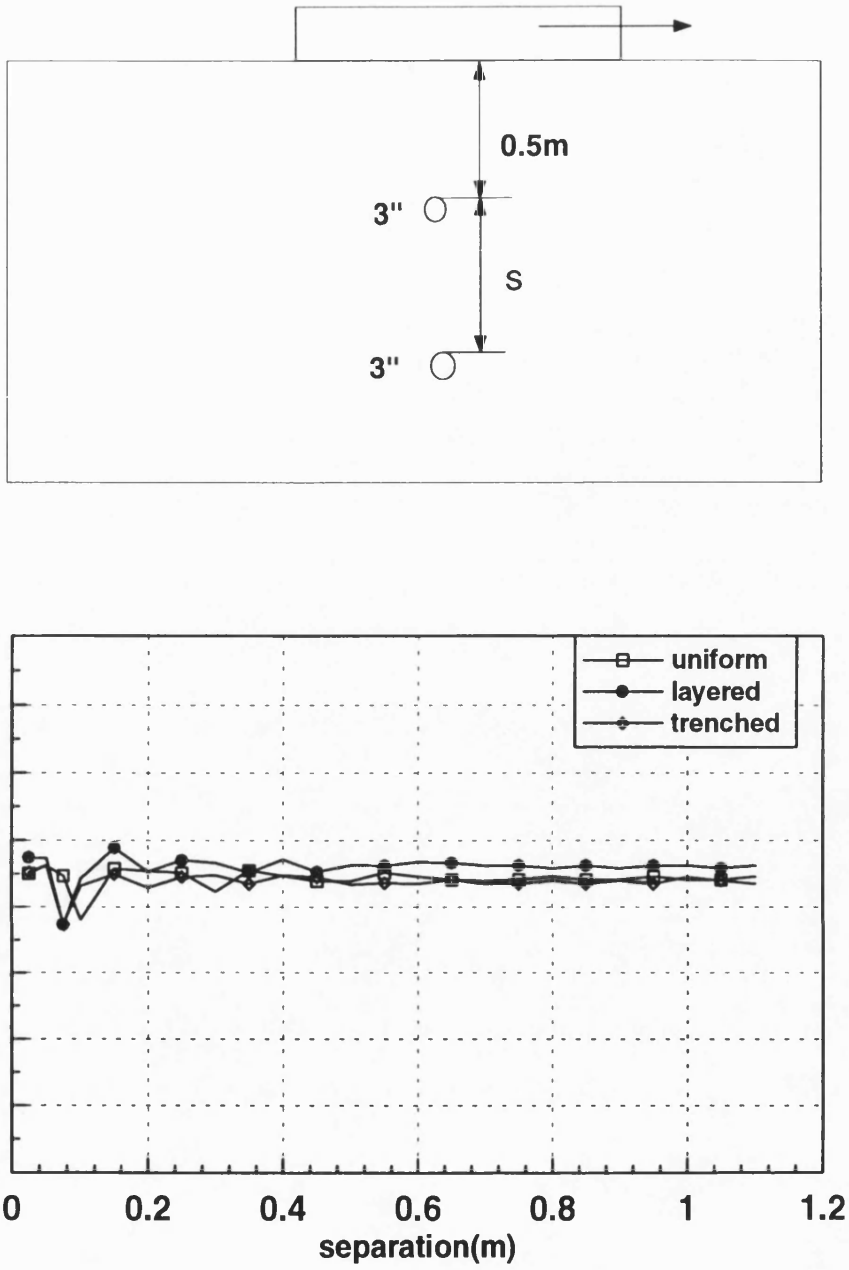

Figure 5.11: Computed safe digging depth versus vertical target separation for targets in uniform (□), layered (•) and trenched(◇) Media

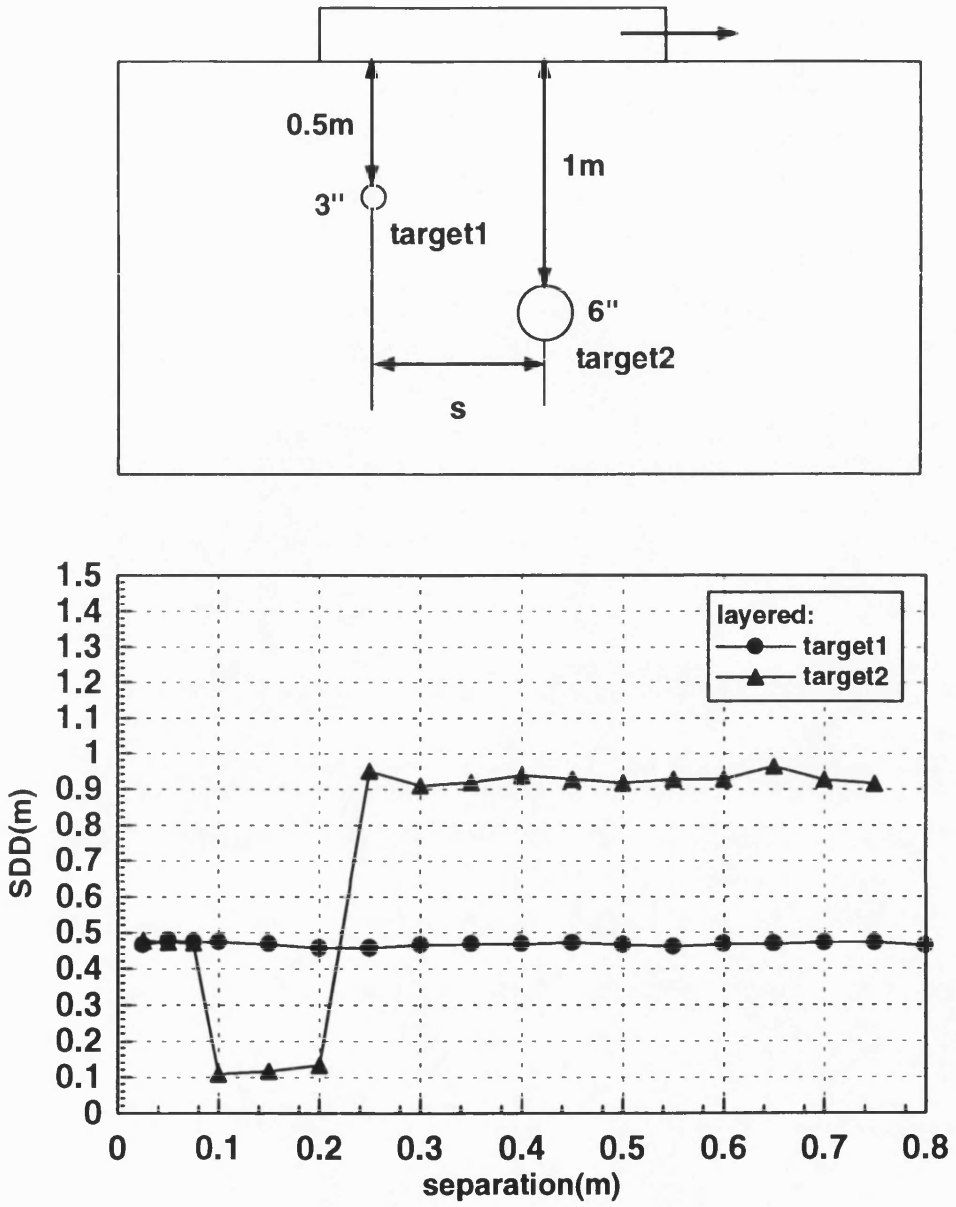

Figure 5.12: Computed safe digging depth versus horizontal target separation for twin targets in layered media

tently centre the unit over the shallowest target. The algorithm also detects the deeper, larger target, as illustrated in Figure 5.6, with a correct depth computed for separations above 0.25m. For separations below 8cm the resolution limit of the system is reached with a target safe digging depth being calculated at of 0.46m.

5.5 2D Scan Simulations

5.5.1 Simulation of measured data

The previous section gives the one dimensional results. This section will provides two dimensional simulation results which were produced using the Mathcad program. The program simulates the use of the five head system to detect single target buried in sand at 0.24m depth and 250cm offset. The simulation parameters are as following:

Sampling frequency	6250Hz
Sampling number	2048 points
Sweep range	250MHz to 750MHz
Sweep time	0.024s.
Refractive Index	2.75
Attenuation Index	0.03

The 2D scan map key is 5dB per step for 12 steps representing 60dB range. The light the intensity, the greater the amplitude of FFT data. The direct coupling between T_A to R_A and T_A to R'_A will have an effect on detecting target, especially the shallower target as seen in Figure 5.13, 5.14, 5.15. These show the target 2D map for different direct coupling levels. Figure 5.13 has the direct coupling value -30dB and -50dB from T_A to R_A and from T_A to R'_A. Figure 5.14 has the value -60dB and -80dB, while Figure 5.15 represents direct coupling -180dB and -200dB. From these figures it can be seen that, the clarity of the target image is improves as the direct coupling level reduces. Figure 5.15 show the ideal case.

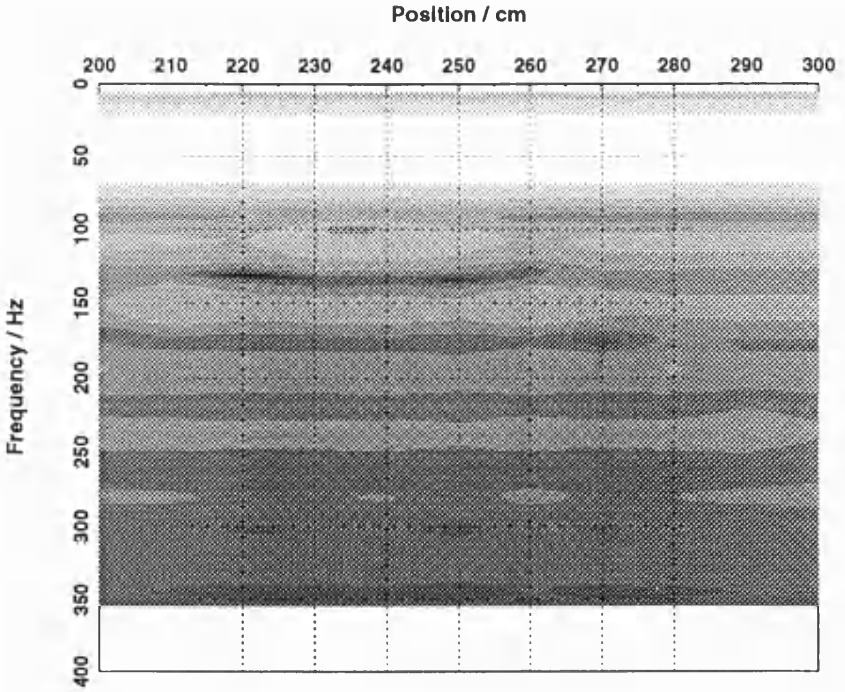

(a)

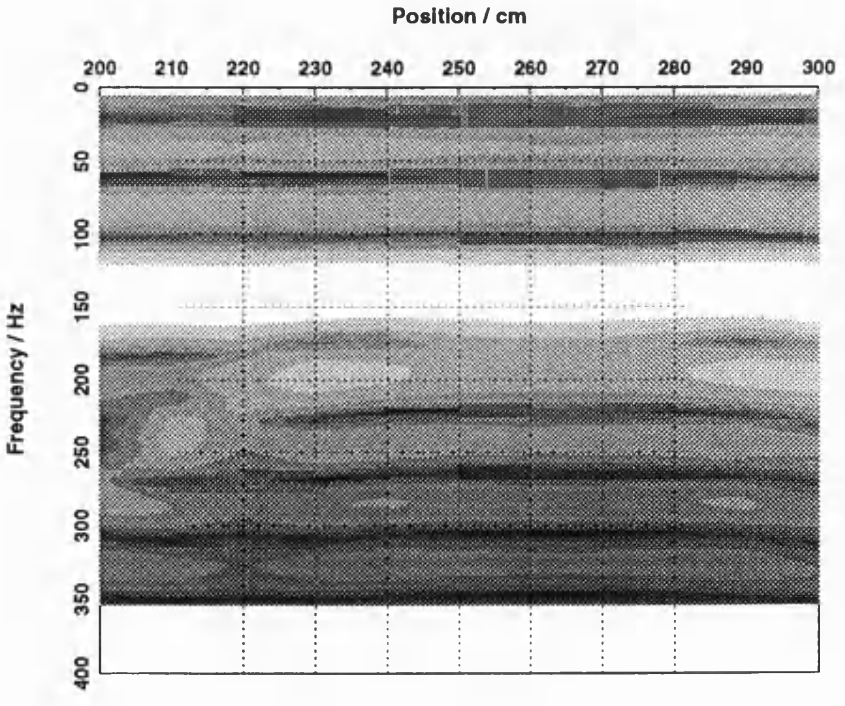

(b)

Figure 5.13: 2D scan simulation result for (a) Channel 1 with direct coupling -30dB and (b) Channel 3 with direct coupling -50dB

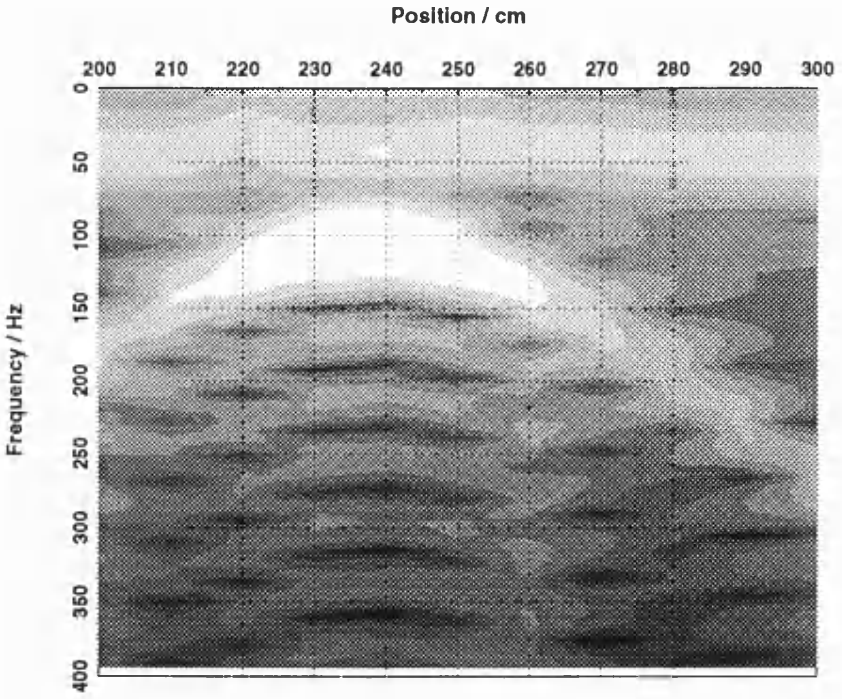

(a)

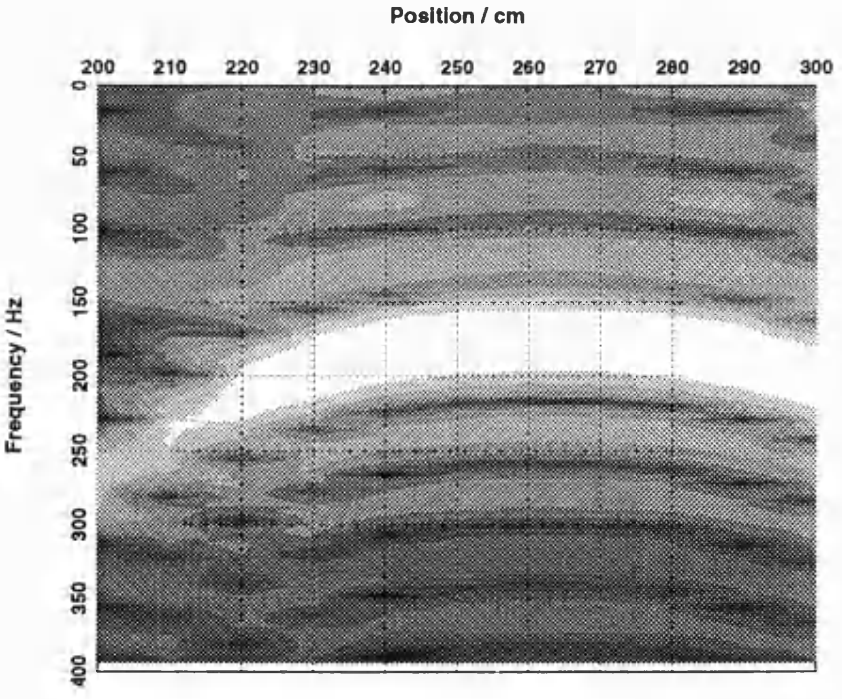

(b)

Figure 5.14: 2D scan simulation result for (a) Channel 1 with direct coupling -60dB and (b) Channel 3 with direct coupling -80dB

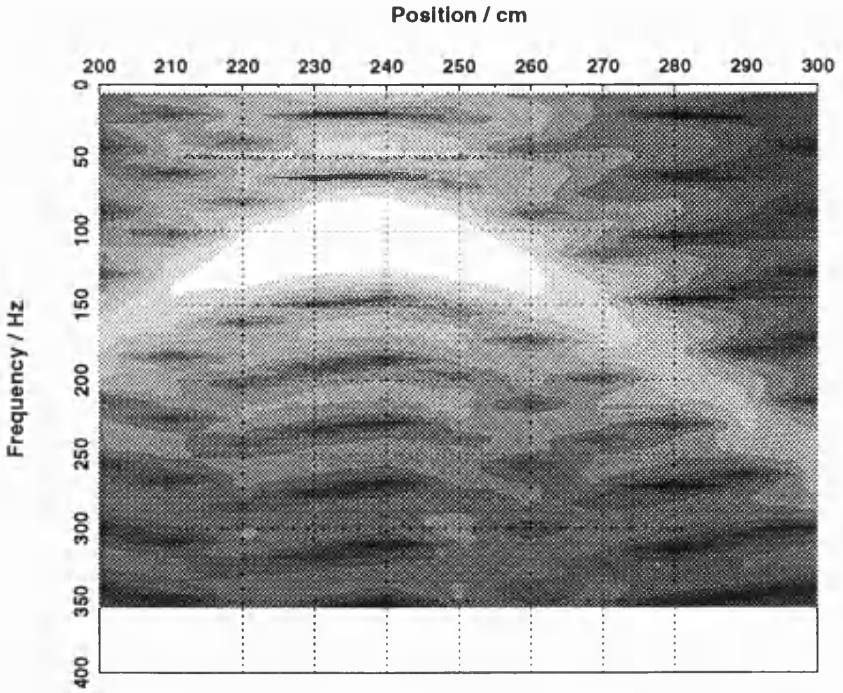

(a)

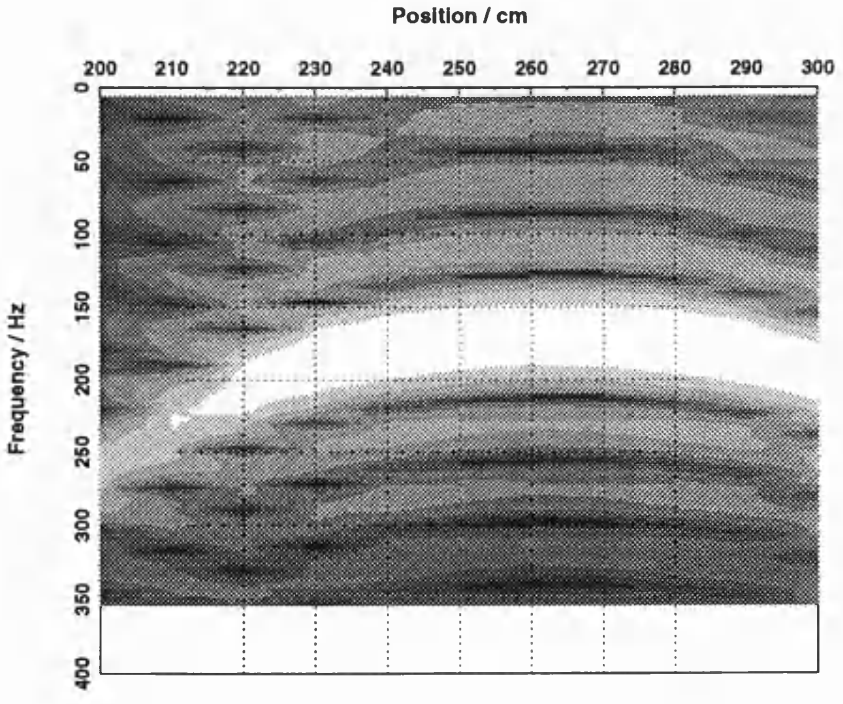

(b)

Figure 5.15: 2D scan simulation result for (a) Channel 1 with direct coupling -180dB and (b) Channel 3 with direct coupling -200dB

5.5.2 Simulation Synthetic Aperture image

The principles of synthetic aperture algorithm for FMCW radar has been provided in Chapter 4. Figure 5.16, 5.17, 5.18 show the results from application of the synthetic aperture algorithm to the simulated data. The results show that target image resolution in the azimuth direction has been improved clearly by the synthetic aperture algorithm. The results show when the direct coupling is stronger than the target response, the synthetic aperture algorithm can not provide a high resolution target image. Results have also been provided by using different refractive index for the ideal very low direct coupling case. Figure 5.19 with the refractive index changed 20% show that the synthetic aperture image resolution has been reduced.

5.6 Conclusion

A number of representative target situations have been investigated using the signal processing mathematical model and have consistently shown that the unit will be centred over the shallowest object, and the safe digging depth is reliably calculated in all the cases.

Horizontal and vertical resolution studies have also been carried out using the signal processing mathematical model. These have indicated that the current horizontal resolution is set at 15cm and the vertical resolution is set as 4cm for a pair of 3″ diameter targets.

It has also been seen that the synthetic aperture algorithm can effectively improve target image resolution in azimuth direction for the simulated data when the direct coupling level is lower than target response. Errors in the assumed refractive index can also effect the result of the synthetic aperture algorithm by reducing resolution somewhat.

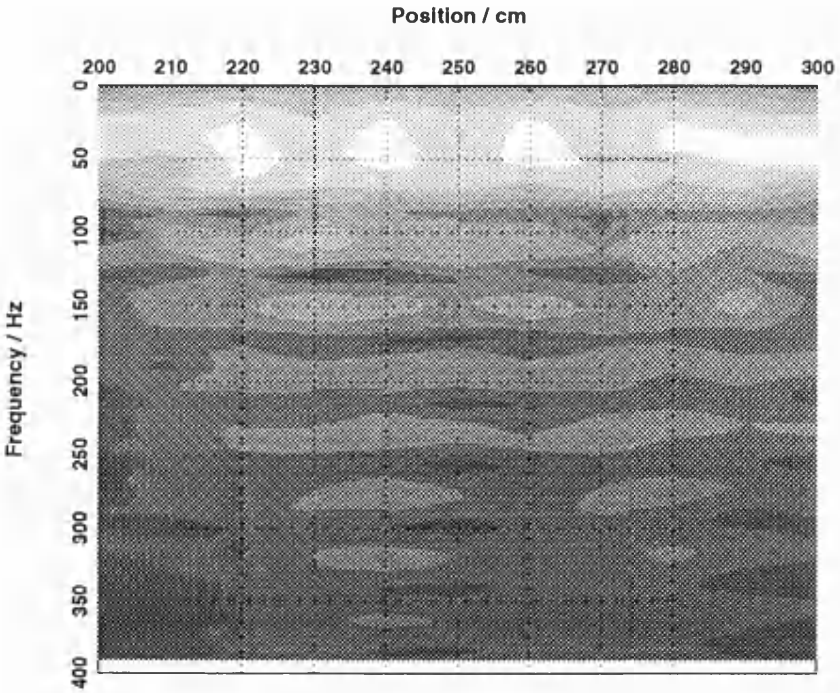

(a)

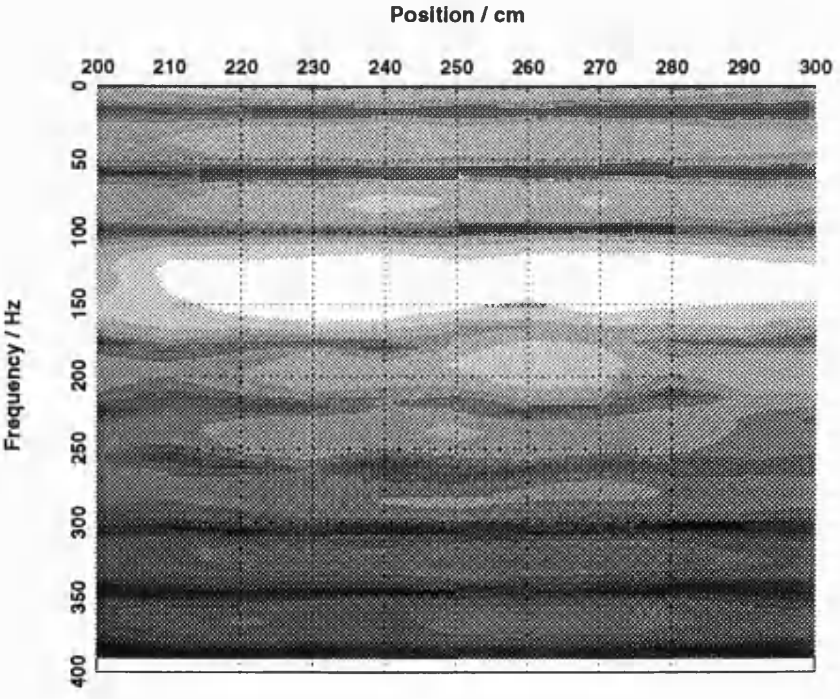

(b)

Figure 5.16: Synthetic aperture algorithm applied on simulated data for (a) Channel 1 with direct coupling -30dB and (b) Channel 3 with direct coupling -50dB

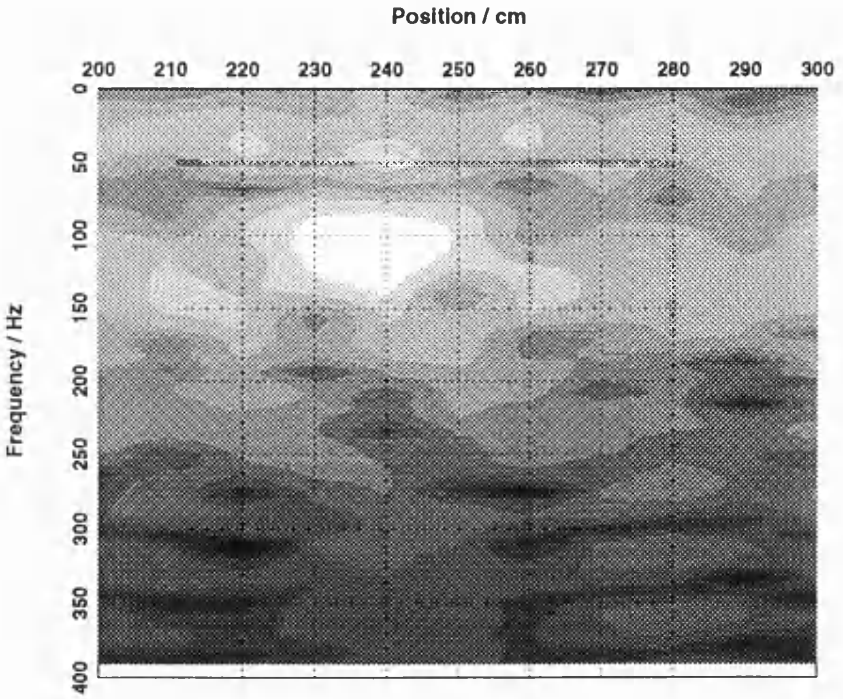

(a)

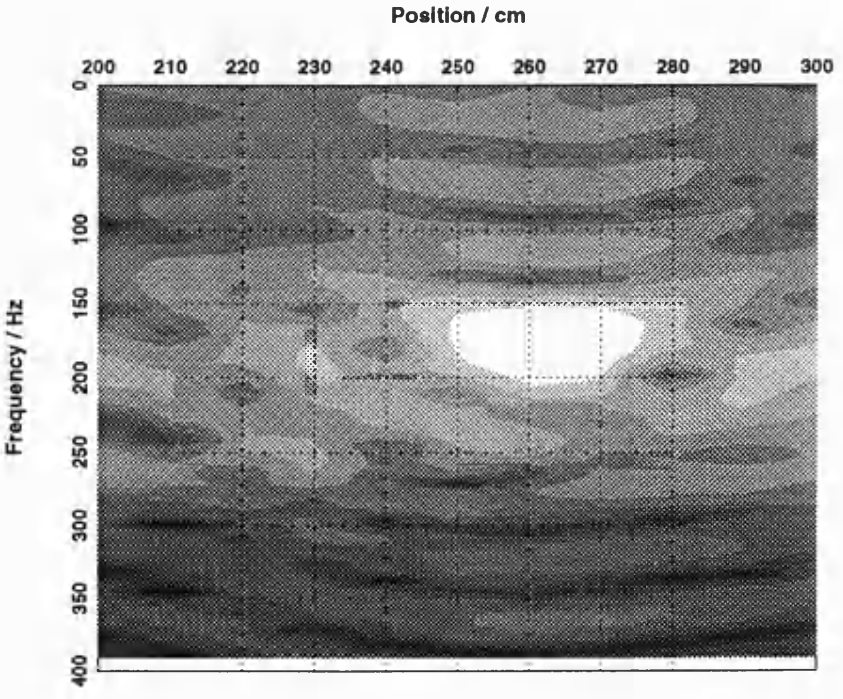

(b)

Figure 5.17: Synthetic aperture algorithm applied on simulated data for (a) Channel 1 with direct coupling -60dB and (b) Channel 3 with direct coupling -80dB

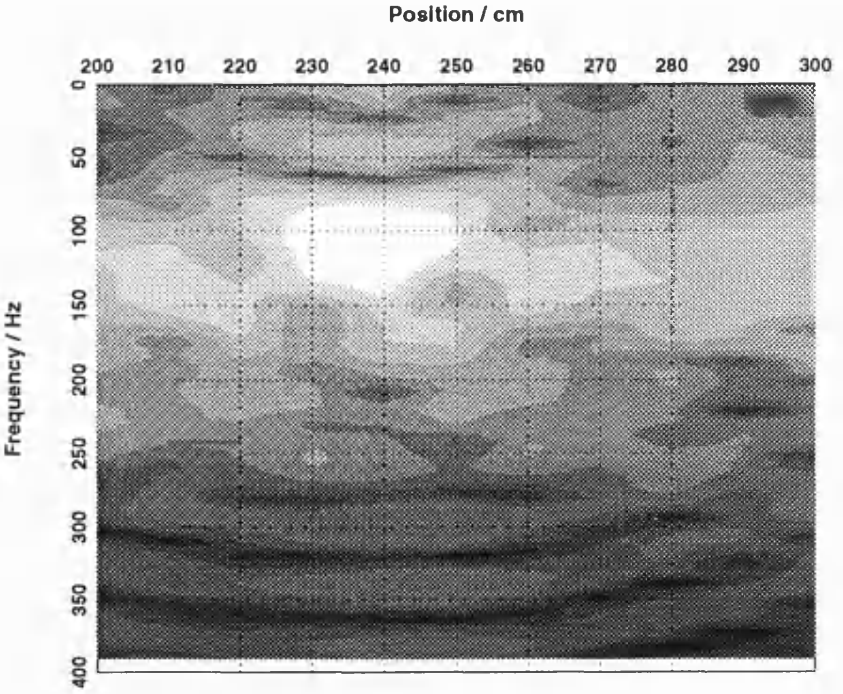

(a)

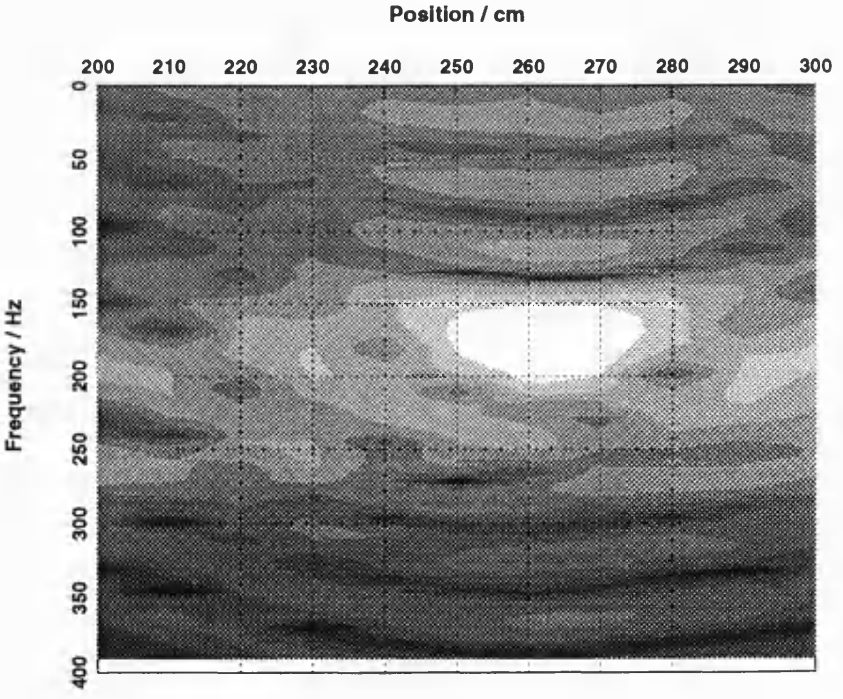

(b)

Figure 5.18: Synthetic aperture algorithm applied on simulated data for (a) Channel 1 with direct coupling -180dB and (b) Channel 3 with direct coupling -200dB

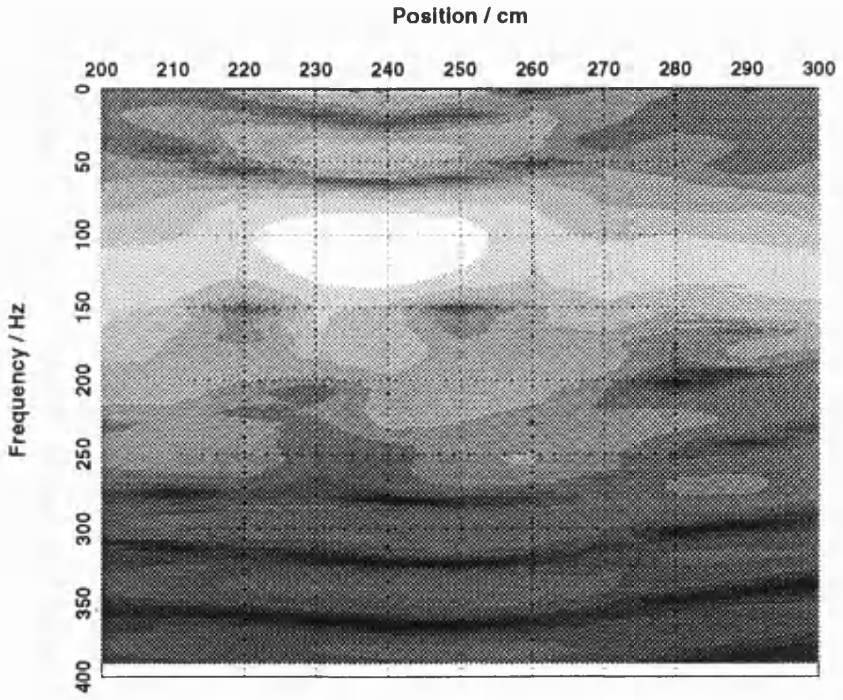

(a)

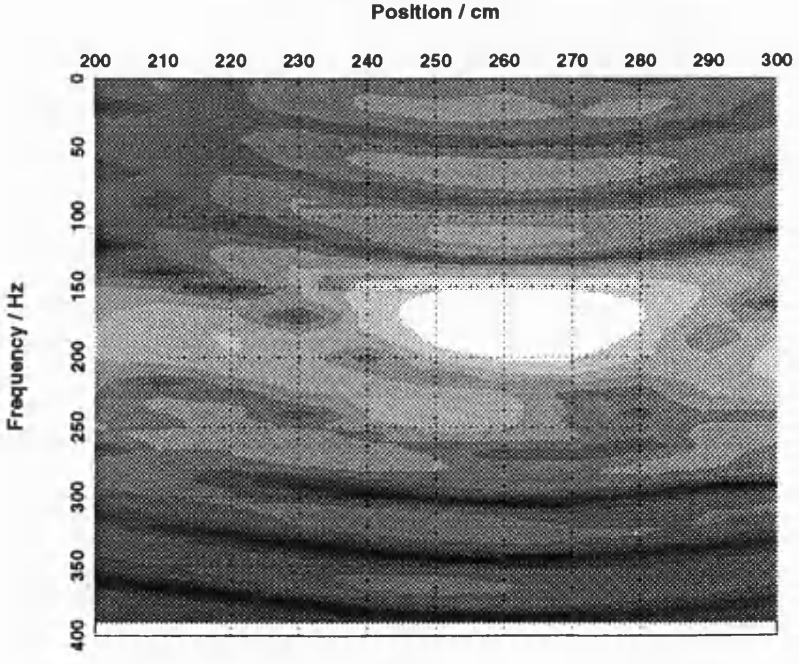

(b)

Figure 5.19: Synthetic aperture algorithm applied on simulated data for (a) Channel 1 with direct coupling -180dB and (b) Channel 3 with direct coupling -200dB for refractive index changed 20%

Chapter 6

Experimental Results from Analysis Model

6.1 Outline

This chapter describes the experimental system software and provides experimental results from tests using the FMCW radar prototype over a test site. The chapter gives results from applying a set of matched filters and clutter rejection filters to the real data.

6.2 Implementation of the Target Analysis Algorithm

The target analysis algorithms have been developed using Microsoft QuickBasic as a module within the signal processing mathematical model. In order to maintain compatibility with the software used to control the UHF sub-system electronics, these algorithms have been implemented in Borland Turbo C^{++} Version 3.0.

The algorithm receives information from the data acquisition and control algorithm in three formats.

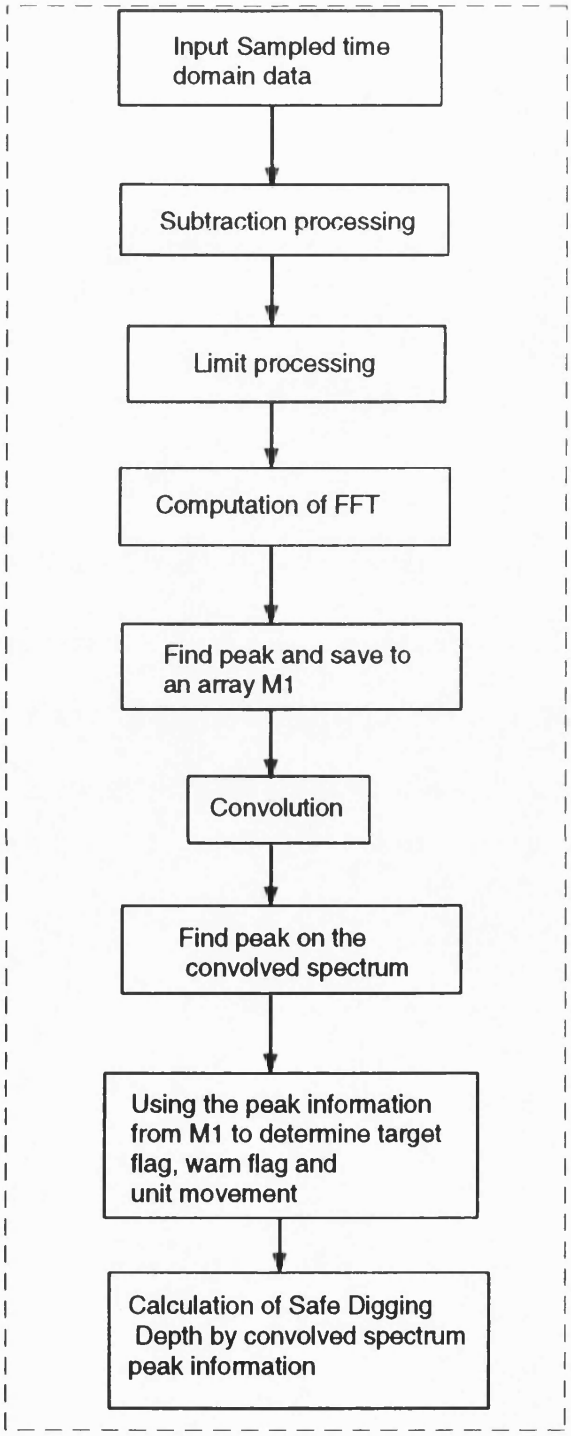

Figure 6.1: Target analysis algorithms for experimental system

The data acquisition parameters concerning the number of input channels, the maximum number of input samples and the sampling rate are incorporated into the target analysis algorithms explicitly using the `#define` command in C, since these parameters are fixed by the control system hardware, they are unlikely to change frequently.

The data acquisition control file which is used to provide the details of the UHF frequency sweep range, number of input samples, and modulation schemes for the UHF electronics is read in as a data file. It is envisaged that this information may be modified by the target analysis algorithms at a later date to further improve the resolution of the system.

The sampled output of the receiver channels is currently passed as a file between the data acquisition and control algorithms and the target analysis algorithm, for testing purposes. The complete integration of these algorithms will enable this information to be eventually passed as a data array to speed the calculation of the safe digging depth.

The algorithms have been developed for the experimental system such that the number of channels is set in the software, hence removing the need to modify the algorithms as the number of channels is increased on the experimental system.

The experimental target analysis model has been modified to suit practical use and the procedure is shown in Figure 6.1.

The analysis algorithms use two stage processing strategy where the presence of a target is first determined using frequency and amplitude thresholding as shown in Figure 6.2. The thresholding value in the data file has been chosen from several real tested data sets which worked for all the cases.

The program produces two important indications, the target flag and the warning flag. If response is below the curve shown in Figure 6.2, indicated that there is no significant target, the target flag=0. If it is above, the target flag=1 or 2. The target flag is set to 2, if the calculated depth is below a limiting value. The limit is specified from a data file and is set to 15cm. The SDD algorithm has been found to have problems with accuracy of shallow targets, as shown in Section 4.5.

The warning flag will have non-zero output when the calculated SDD and effective

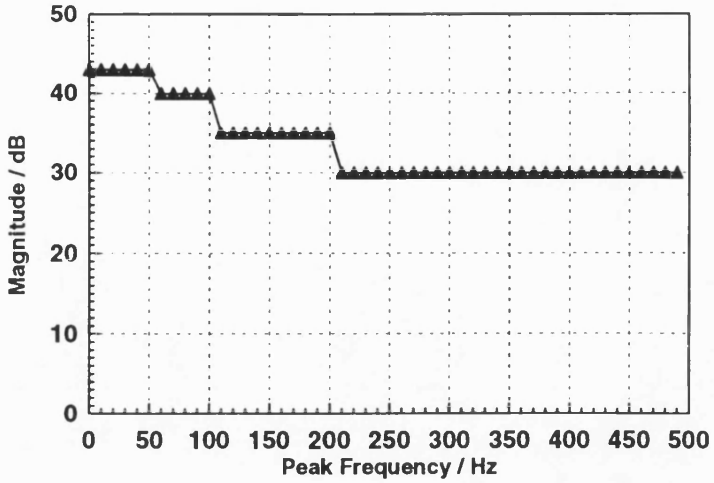

Figure 6.2: Target flag thresholding

refractive index are above preset limits. These are set by a data file. When these tests do not apply the warning flag is zero. Warning flag has five different values which depend on whether the value of safe digging depth and refractive index are within limits.

6.3 Test Site and Experimental System Parameters

6.3.1 Test Site

A experimental test cell has been constructed at the University. This enabled system testing to be undertaken in a uniform medium, with the ability to bury single and multiple targets at varying depth and enabling the operation of the depth measurement system to be verified. The site is 3 metres wide by 5 metres long, excavated to a depth of 2.8 metres and filled with sharp sand. The site has been levelled and the trolley used to transport the depth measurement system modified to lower the antenna head over a large height range.

The test site is shown in Figure 6.3. For the main series of tests, three targets have been buried in the tests site. Target one and target two are 5cm diameter power cables,

30cm depth and located at positions 290cm and 390cm. Target three is a 1.4cm diameter distribution cable at 10cm depth and located at position 330cm. The following results are all from this target configuration except those shown in Section 6.4 for which two targets have been used.

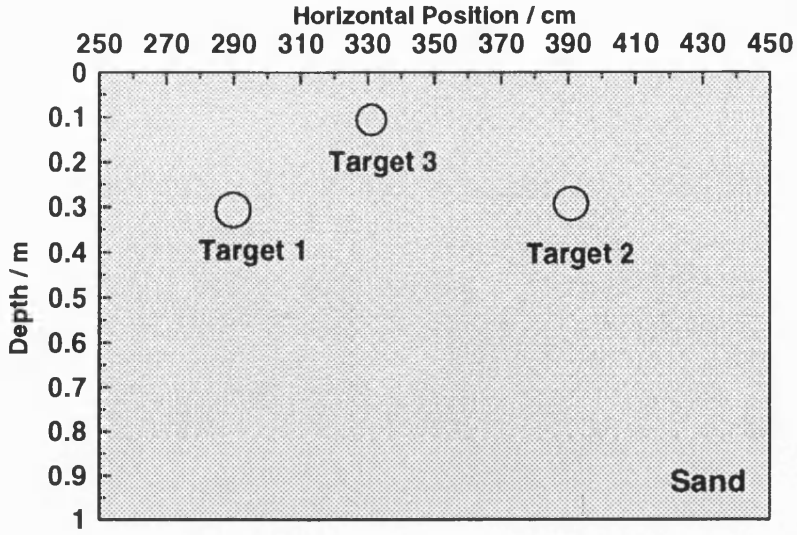

Figure 6.3: Test site for experimental system

6.3.2 Experimental System Parameters

The experimental system parameters for using on the tests are as below:

Sweep Range	250MHz to 750MHz
Sweep Time	0.024s
Repetition Time	0.131s
Sampling Frequency	6250Hz
Sampling Number	2048

6.4 Two Targets Test Results

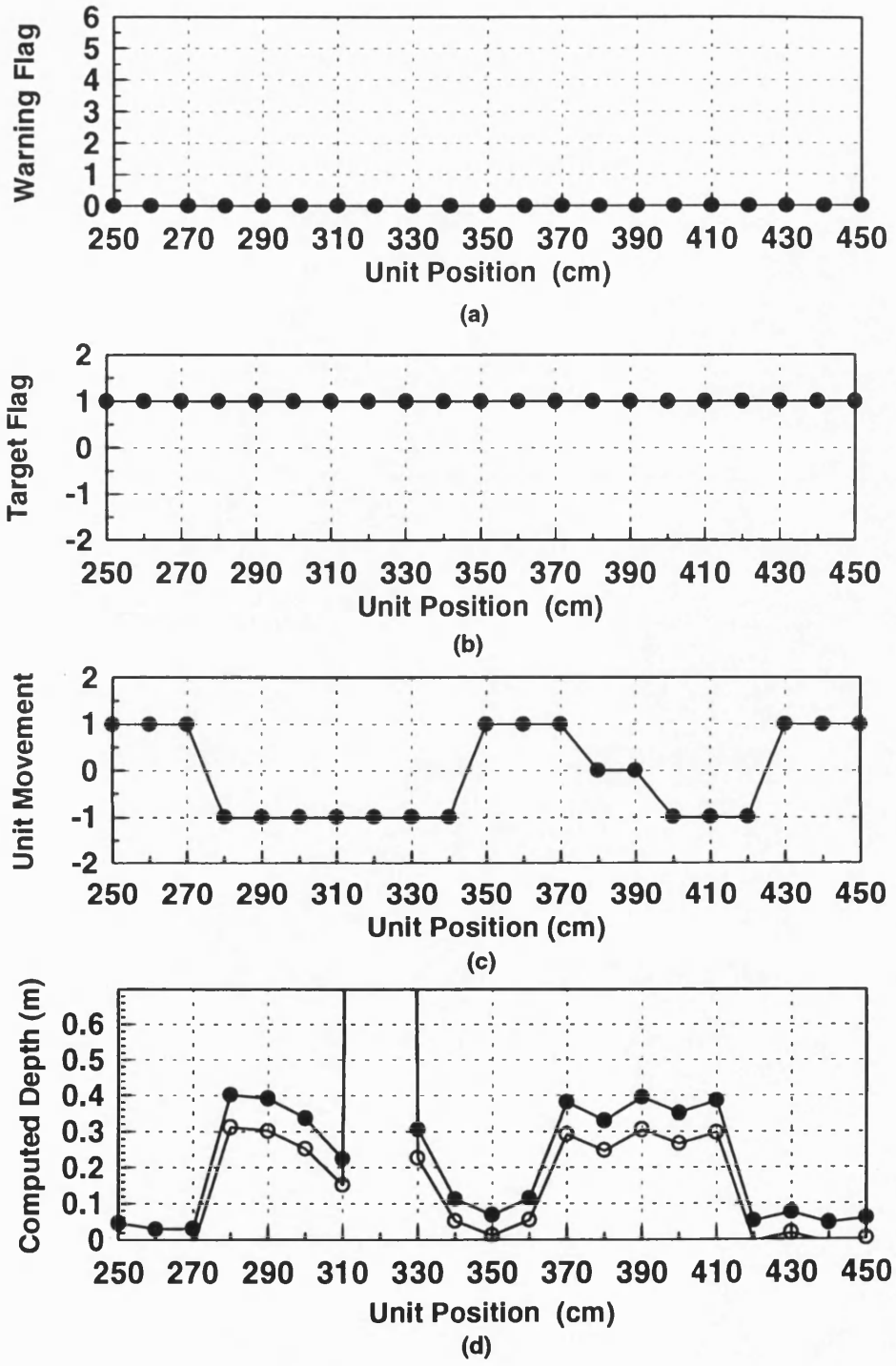

Figure 6.4: Two targets test results for (a) warning flag, (b) target flag, (c) unit movement indication and (d) safe digging depth

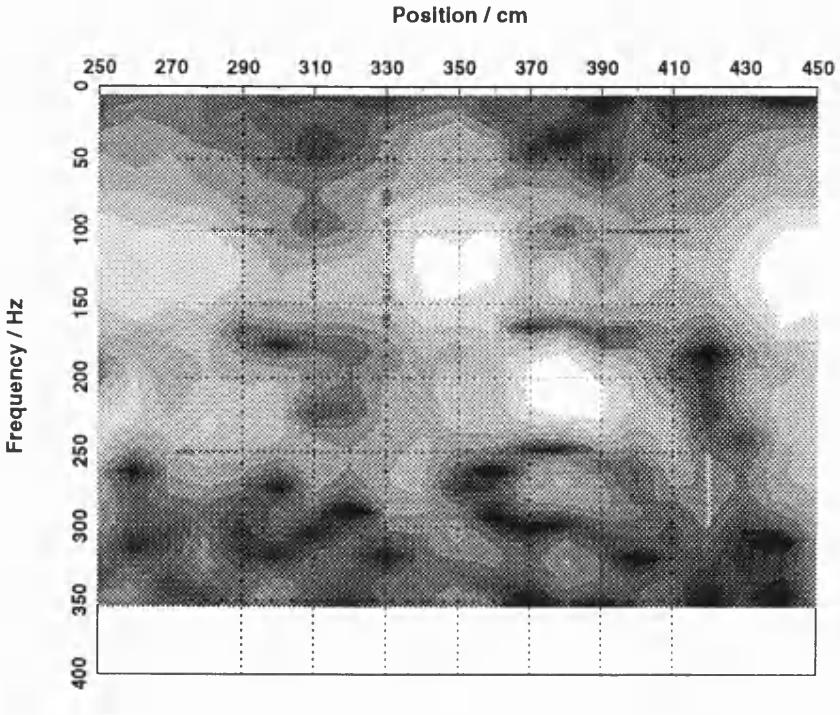

Figure 6.5: 2D scan two targets test result for channel 1

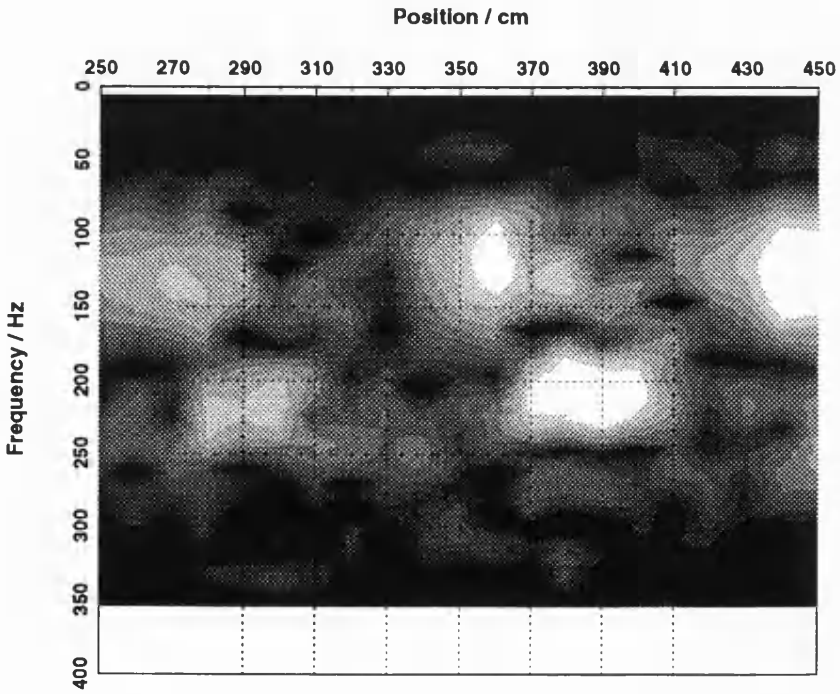

Figure 6.6: 2D scan two targets case result of channel 1 and channel 2 convolution

The first series of experimental tests used two targets, as shown in Figure 6.3. Target1 and target 2 are at depths of 30cm and are positioned at 290cm and 390cm offset. Figure 6.4 shows the states of the warning flag, target flag, unit movement and SDD results. These provide a clear indication that one target is between 270cm to 280cm and another target between 370cm to 400cm, while the unit movement tells operator move away between 340cm to 350cm and 420cm to 430cm. SDD results show two curves, the white circle curve shows the result after 10% thresholding applied on the original result which shows targets depth are around 30cm. The warning flag indicates the all results are reliable and target flag=1 means there are targets underground.

The 2D plot for channel 1 and the convolved result of channel 1 and channel 2 have also been provided in Figure 6.5 and Figure 6.6. The channel 1 result shows that there is a strong target appeared between 180Hz to 230Hz with horizontal position between 380cm to 420cm. Another target appears as a weak reflection between 200Hz to 250Hz with horizontal position 270cm to 300cm. Note the strong reflections between 100Hz to 150Hz are direct coupling which has been removed mostly by reference signal subtraction algorithm, but still remain some strong crosscoupling. The convolved result shows clearer images of two targets around 290cm and 390cm horizontal position although there are still some direct coupling left.

6.5 Original Test Results

The test results from original target analysis algorithm, which only use the reference signal subtraction algorithm, are shown in Figure 6.7 and 6.8. The reference signal has been taken at 150cm offset on the test site before scan test. Figure 6.7 gives the warning flag, target flag and unit movement results. Figure 6.8 gives safe digging depth and refractive index results. The warning flag is always zero which means that the measured results are reliable. The target flag shows the presence of a shallow target from $325cm$ to $335cm$, and other targets are also indicated for all other positions.

Unit movement results show three arrow direction changes from right to left(+1 to -1) along the scan test. Unit movement indication tells operator to center a targets

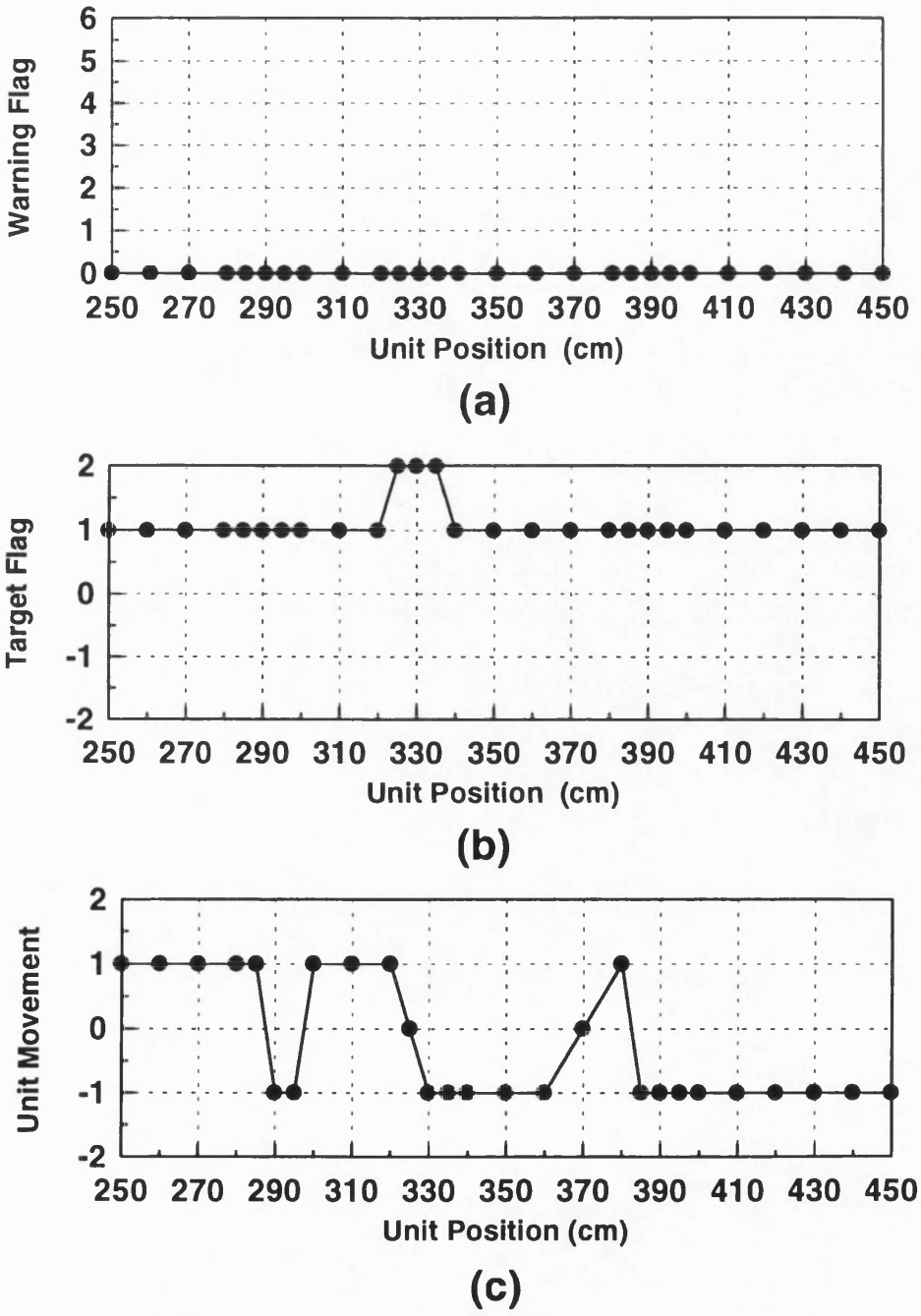

Figure 6.7: (a) Warning flag, (b) Target flag, and (c) Unit movement results from subtraction algorithm

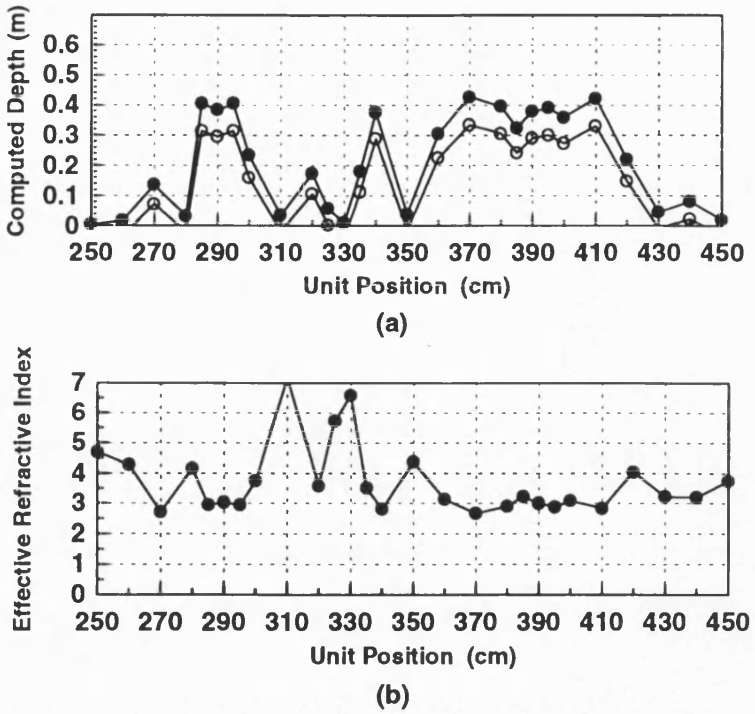

Figure 6.8: (a) Safe Digging Depth, and (b) Refractive index Results from subtraction algorithm

between 285cm to 290cm, 320cm to 330cm and between 380cm to 385cm. The unit movement tells the operator to move away from targets between 295cm to 300cm and between 360cm to 380 which are ghost targets as seen in Section 5.4.

The SDD results are approximately 0.3m for target one and 0.25m for target two. Target three's depth was shown to be unreliable because it is a shallow target whose depth is measured as shallower than 15cm. In Figure 6.8, the white circle curve show the SDD results after 10% thresholding. Refractive index results show about 2.9 which is closer to the sand refractive index 2.75.

The 2D plots shown in the next few pages use twelve uniform quasi-gray scales to cover the normalized magnitude in the spectrum with white indicating strong reflection and black means 36dB below the strongest reflection.

Figure 6.9 show the unprocessed 2D plot for channel one. Unprocessed data show very strong direct coupling between transmitter and receiver from 130Hz to 180Hz. The targets image is very weak and difficult to distinguish. After subtraction of the reference

data set, the results shown in Figure 6.10 reveal that there are two light spots, hence target two and target three are around 310 to 330cm, 380 to 390cm offset. Target one's image is weaker than the others, but it is still visible.

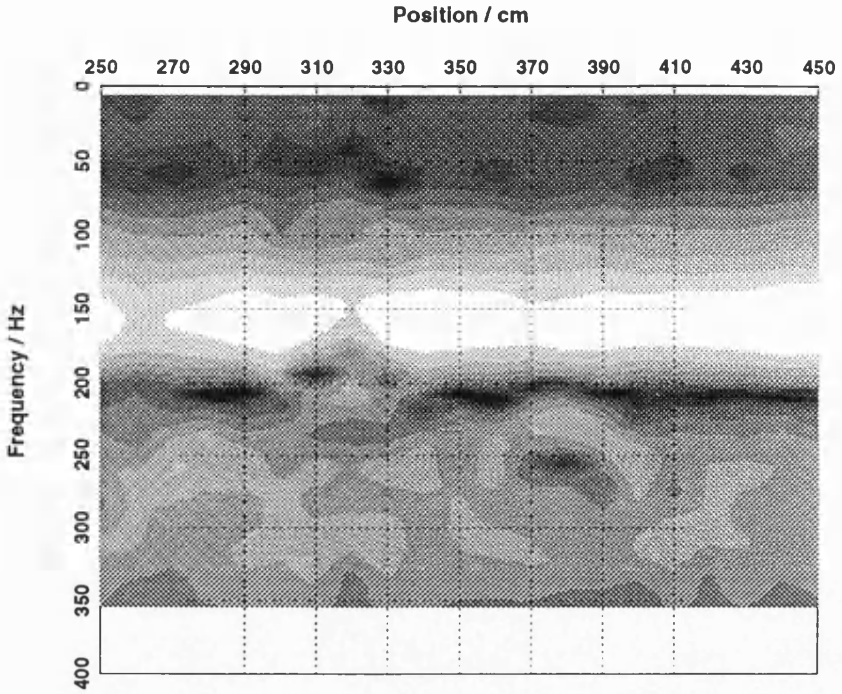

Figure 6.9: Unprocessed 2D scan plot for channel 1, twelve uniform quasi-gray scales

Clearly the subtraction algorithm can remove much of the clutter and produce clear target images. In addition the resulting data processing produces the satisfactory unit movement, target flag warning flags and the SDD calculation.

6.6 Limiter Algorithm Results

Two limiter algorithms have been tested. One uses an amplitude limiter on the subtracted data and the other one uses a limiter on the raw data.

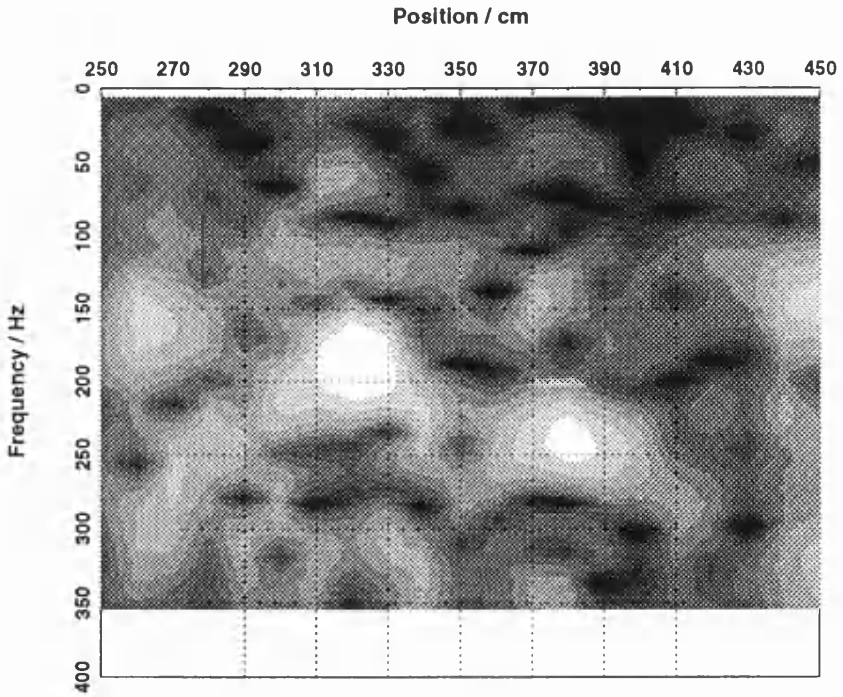

Figure 6.10: Subtracted 2D scan plot for channel 1, twelve uniform quasi-gray scales

6.6.1 Limiter Algorithm Applied on the Subtracted Data

This algorithm is an improved target analysis algorithm which is based on the original analysis algorithm. It differs by way of the addition of a limiter subroutine on the time domain data after reference position data is subtracted. The limit subroutine processes the subtracted time domain data as following steps:

- Multiply the time domain data by a large value C
- Compare with a limit value A
- If the result is greater than A then set the output equal to A. If less than $-A$ set to $-A$, if between the limits A and $-A$ then there is no change.

This process is applied to each sample of the time domain data. The limiter algorithm can remove the amplitude modulation(AM) on the time domain data, hence remove part of the AM components from the spectrum and improve the resolution for detecting targets.

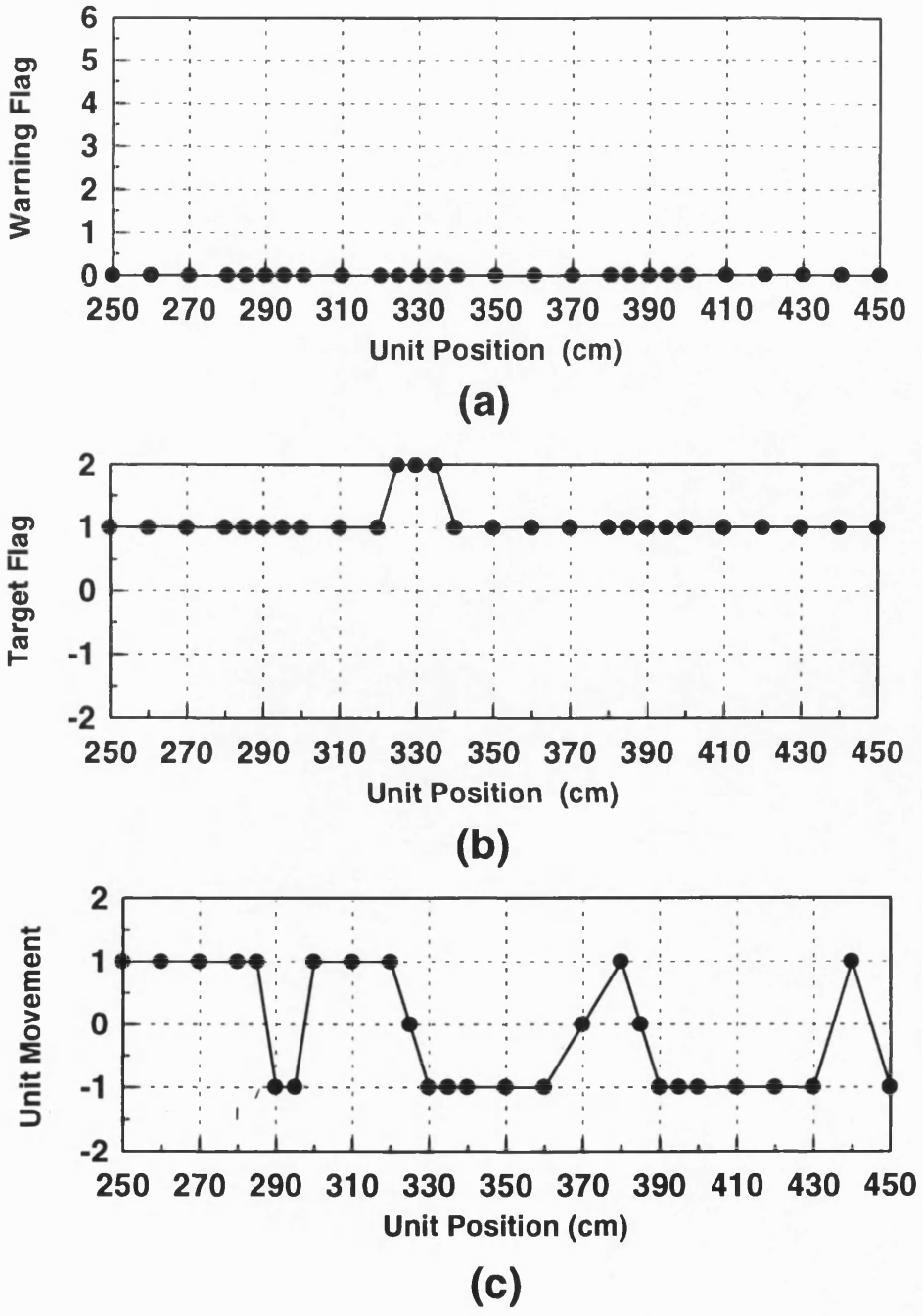

Figure 6.11: Limiter algorithm results for (a) Warning flag (b) Target flag and (c) Unit movement

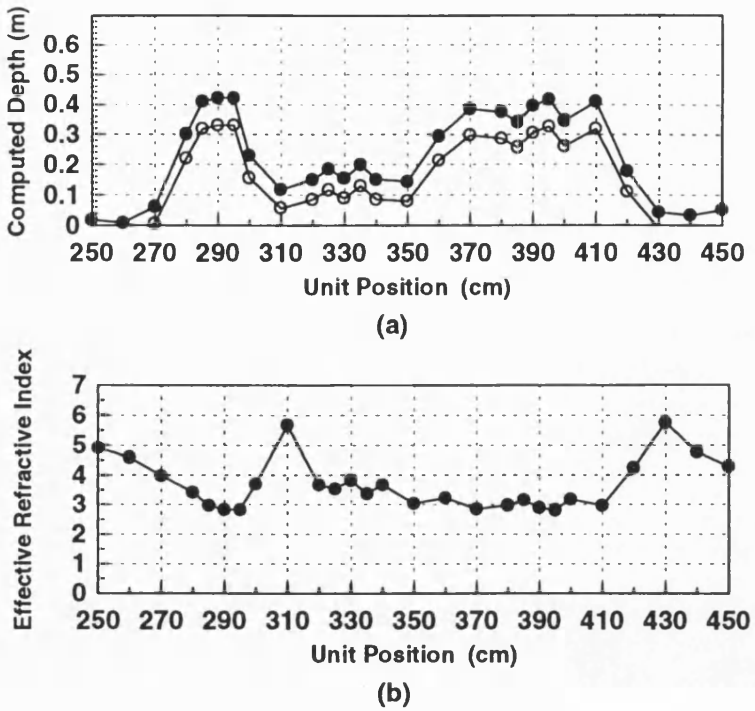

Figure 6.12: Limiter algorithm results for (a) Safe Digging Depth, and (b) Refractive Index

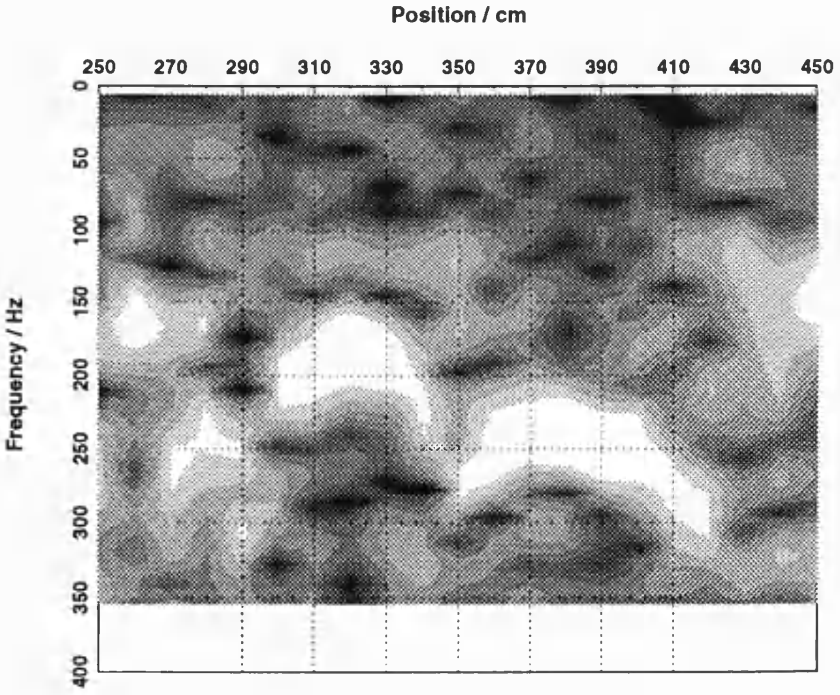

Figure 6.13: Limiter algorithm 2D scan plot for channel 1, twelve uniform quasi-gray scales

Using the limiter algorithm can enhance the ability to detect targets. Figure 6.11 and 6.12 results show there are targets at 325 and 385 offset with another target between 285 to 290 offset, the SDD result for target one, two and three are approximately 0.31m, 0.27m and 0.1m, respectively. The shallowest target's depth can therefore be calculated correctly by using the limiter algorithm. Also the SDD and refractive index results show smooth and less erratic curve comparing with original results as shown in Fig. 6.8, and the unit movement indication results show the more accurate centering the target between 380cm to 390cm at 385cm. The 2D scan shown in Figure 6.13 shows clearer images of these three targets than was achieved without the limiter. The images for target two and target three show a curve which is close to the parabola shape which is the ideal target response as predicted in Chapter 5.

6.6.2 Limiter Algorithm Applied on the Raw Data

This limiter algorithm was also applied to the limiter to the raw tested data, followed by $\frac{\sin(x)}{x}$ subtraction. This algorithm first uses the limiter subroutine on the raw input time domain data, then subtracts a $\frac{\sin(x)}{x}$ signal which has been set to the same phase and magnitude of the raw spectrum peak. This algorithm has the advantage of needing no reference signal. The results show that most cross coupling can be removed if the cross coupling is stronger than target response. Figure 6.14 is the result from channel 1 which shows that most of the cross coupling signal has been reduced and that the two targets are visible, but the results from channel three as seen in Figure 6.15 did not show as much improvement. This was because the direct coupling frequency of channel three was close to the target signal frequency and hence resulted in the wrong position subtraction. Using this approach, the safe digging depth calculated from convolved data becomes unreliable. In earlier work the electronic system included a hardware limiter in the circuit after the detection mixer and limited the raw data [1]. It appears from these results therefore that it is better to limit the data after subtracting reference data.

6.7 A Set of Matched Filters Algorithm Results

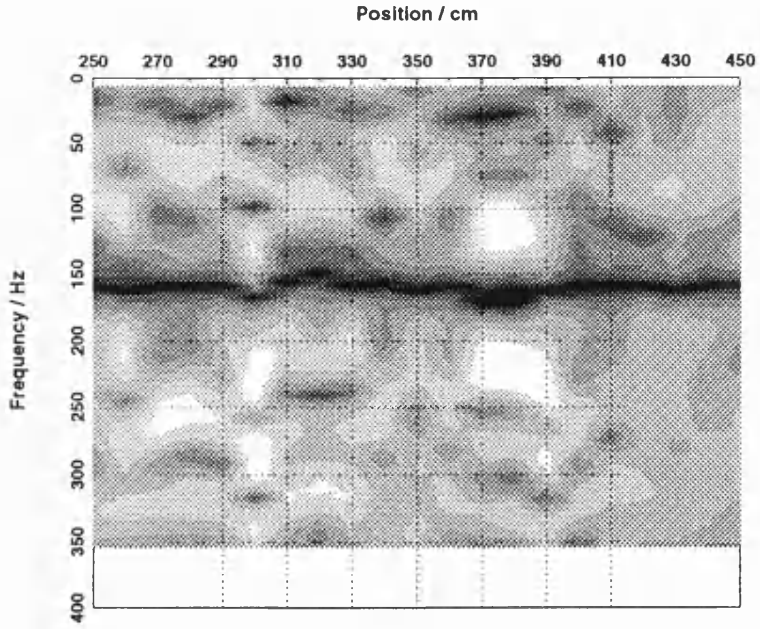

Figure 6.14: Limit followed by $\frac{\sin(x)}{x}$ *subtraction algorithm 2D scan plot for channel 1, twelve uniform quasi-gray scales*

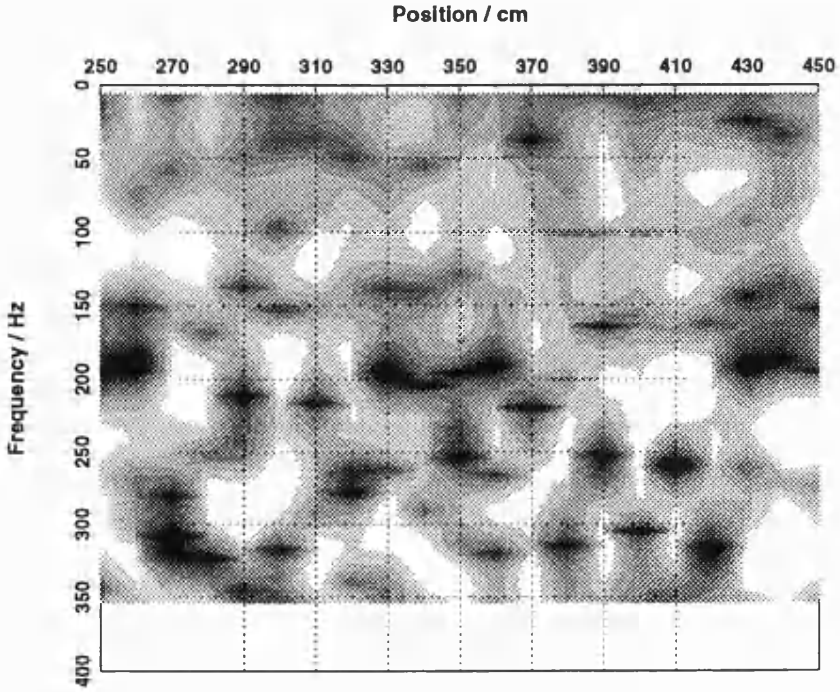

Figure 6.15: Limit followed by $\frac{\sin(x)}{x}$ *subtraction algorithm 2D scan plot for channel 3, twelve uniform quasi-gray scales*

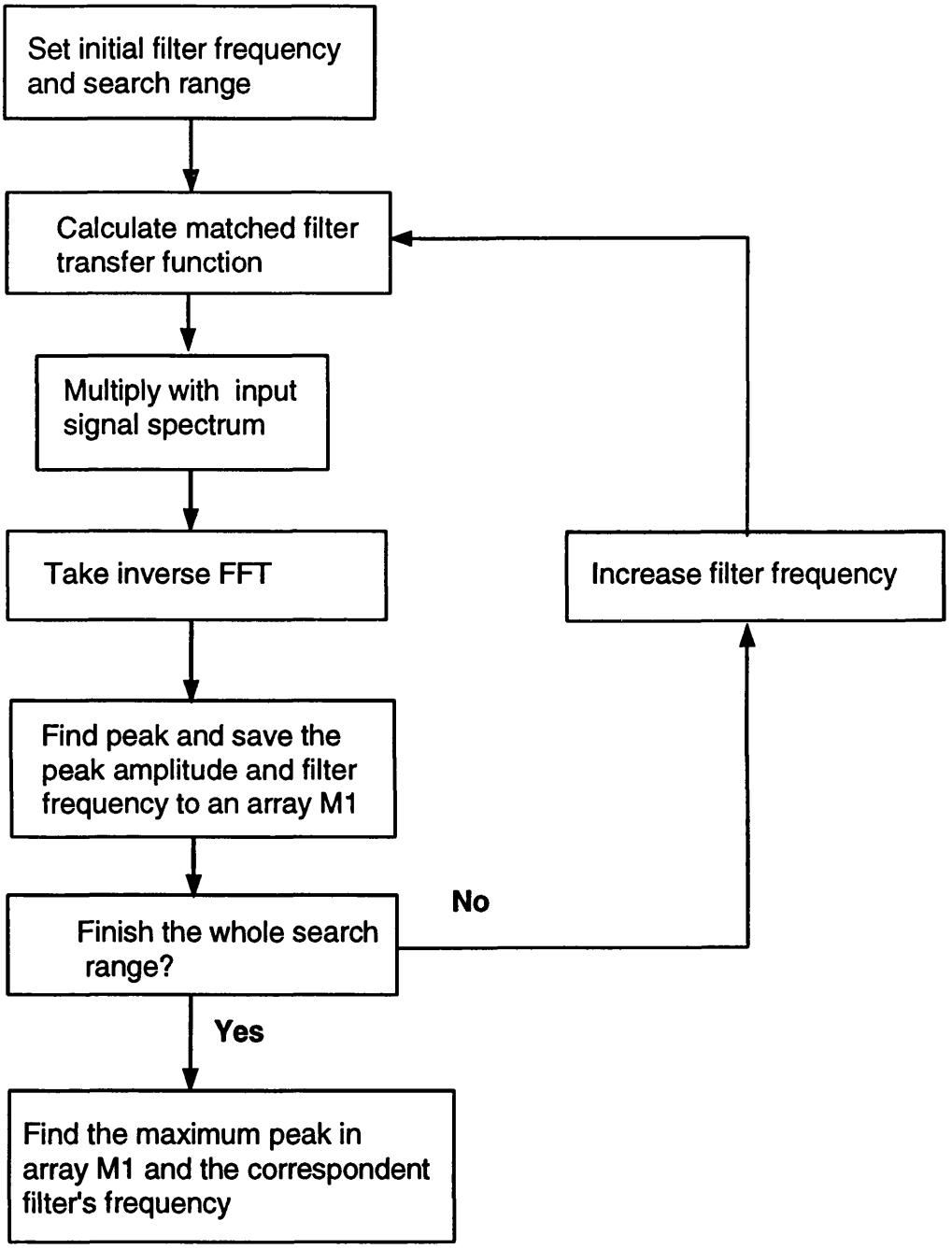

Figure 6.16: A set of matched filter algorithm

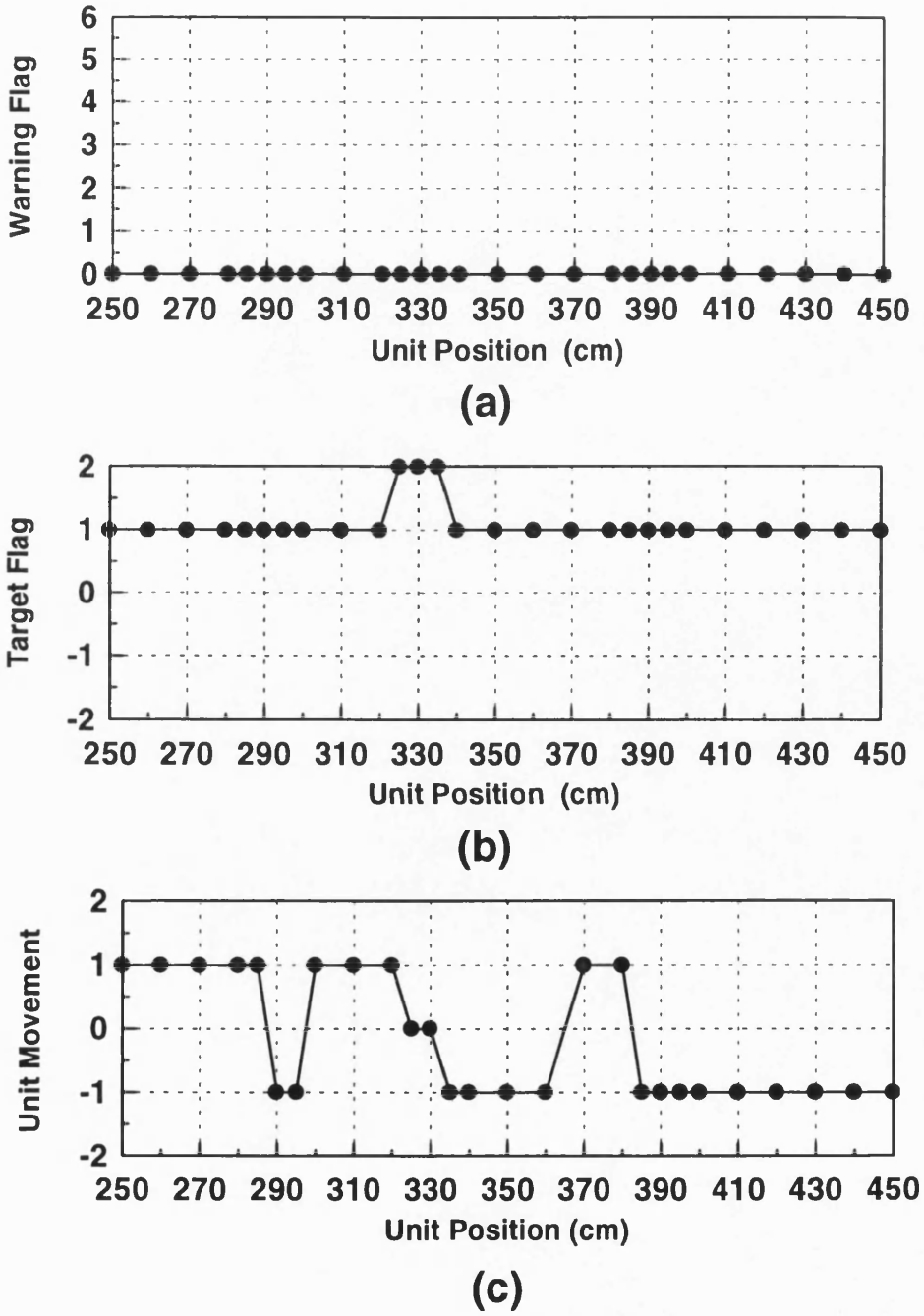

Figure 6.17: (a) Warning flag, (b) Target flag, and (c) Unit movement results from a set of matched filter algorithm

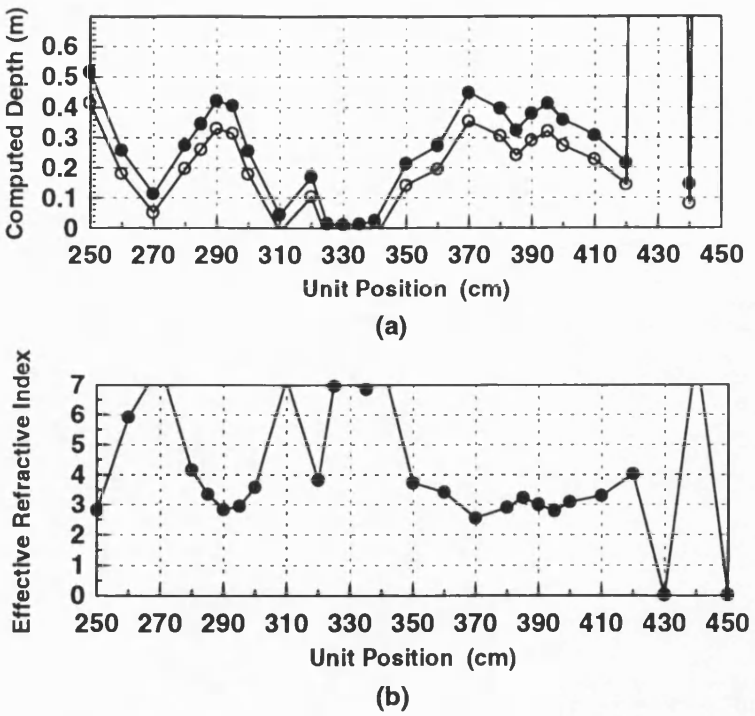

Figure 6.18: (a) Safe Digging Depth, and (b) Refractive index results from a set of matched filter algorithm

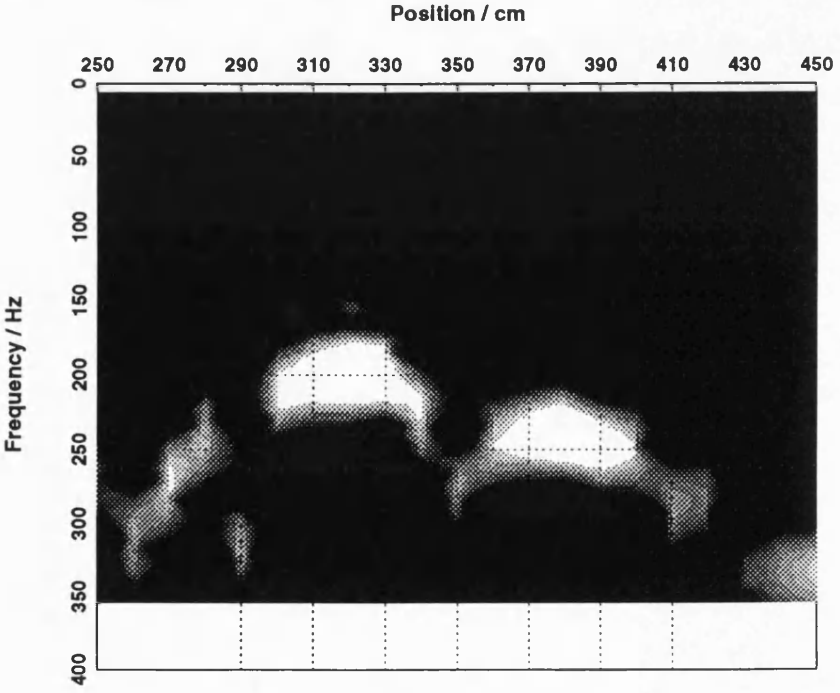

Figure 6.19: A set of matched filter algorithm 2D scan plot for channel 1, twelve uniform quasi-gray scales

The matched filter algorithm principles was described in chapter 4. For the experimental use, a set of matched filter algorithm has been developed as seen in Figure 6.16.

This algorithm uses a varying frequency matched filter to determine input signal frequency. If the filter's frequency is equal to the input signal frequency, the output of filter processing will produce the maximum peak. According to this method, after the whole band has been searched, the filter frequency of the maximum peak will be the target frequency. The results are shown in Figures 6.17, 6.18, and 6.19 which are similar to the subtraction results, but the images are better than the subtraction results as was shown in Figure 6.10. The sidelobes have been suppressed and the images show strong contrast. Unfortunately the drawback of this algorithm is the long processing time required which is of the order of 3 minutes for each test point.

6.8 A Set of Clutter Rejection Filter Algorithm Results

The principles of clutter rejection filter have also been described in chapter 4.

A set of clutter rejection filter algorithms have been developed for processing the real data as shown in Figure 6.20. The algorithm is similar to the set of matched filter algorithm. It adds the clutter simulation part which produces clutter by summing over a band of uniform sine wave burst. The other procedures are similar to those used for the set of matched filter algorithm. In these examples the clutter signal frequencies are from 300Hz to 1200Hz with 30Hz interval.

The results, shown in Figures 6.21, 6.22, and 6.23 reveal that both the 1D and 2D results have been improved comparing with the basic results as shown in Figure 6.10. The processing time of this algorithm is about 3.2 minutes for each test point which limits its application in real time processing.

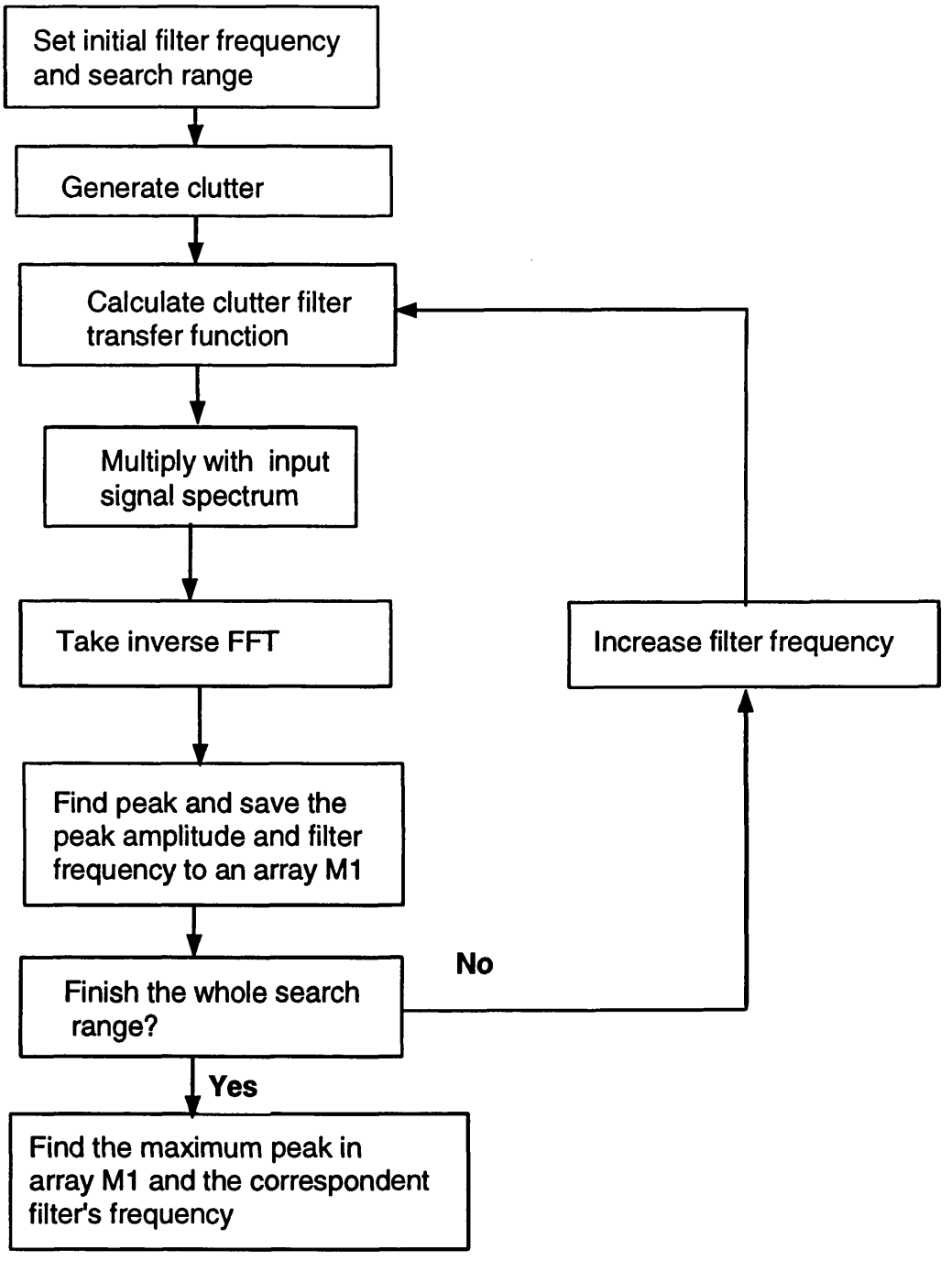

Figure 6.20: A set of clutter rejection filter algorithm

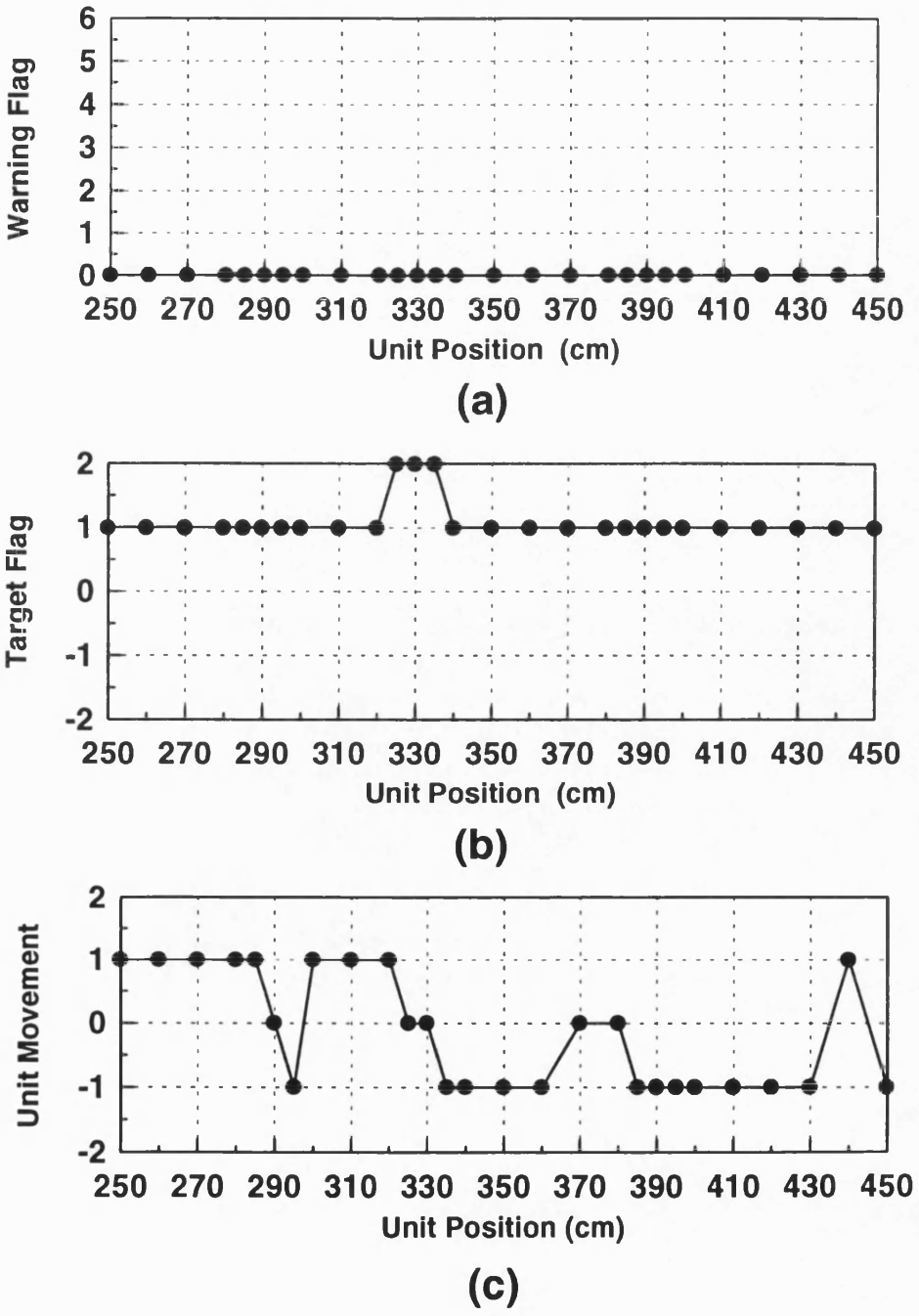

Figure 6.21: (a) Warning flag, (b) Target flag and (c) Unit movement results from clutter rejection filter

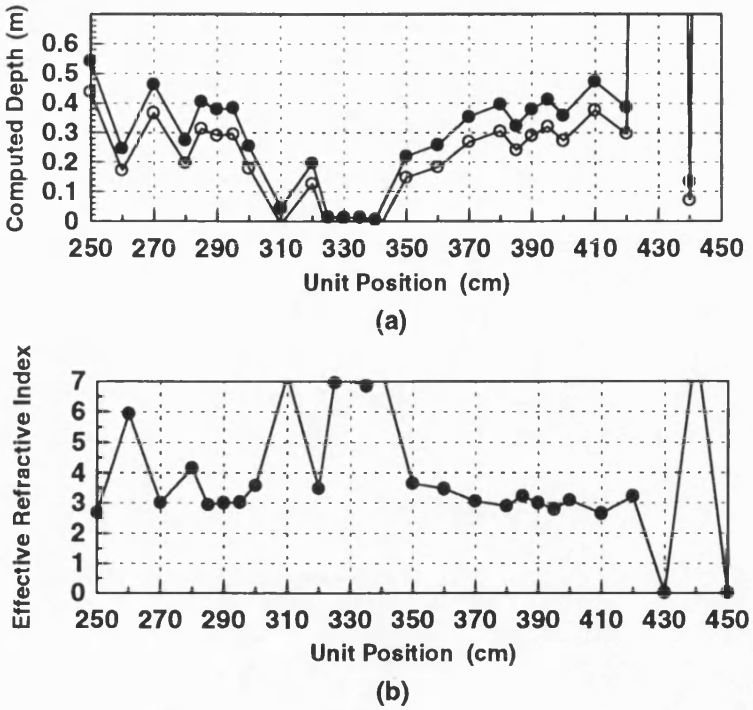

Figure 6.22: (a) Safe Digging Depth and (b) Refractive index results from clutter rejection filter

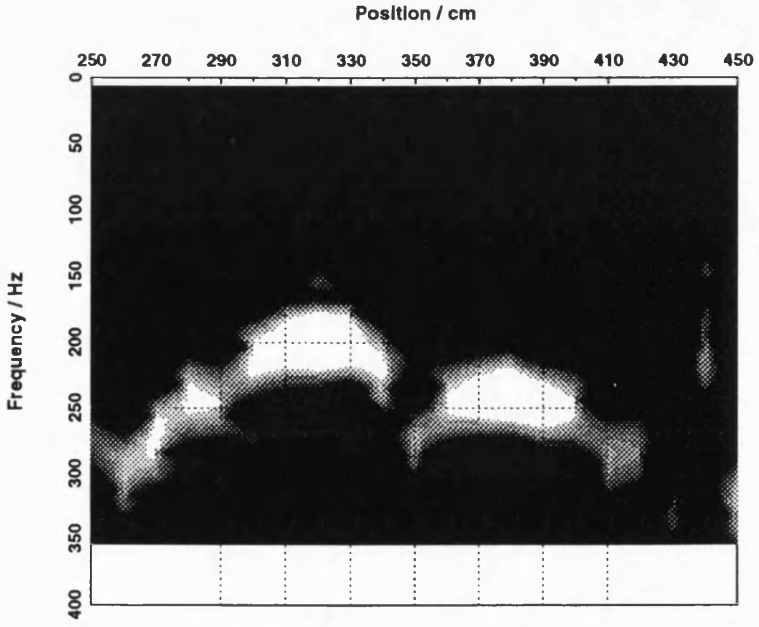

Figure 6.23: A set of clutter rejection filter algorithm 2D scan plot, twelve uniform quasi-gray scales

6.9 Synthetic Aperture Algorithm Results for Real Test Data

Synthetic aperture algorithm applied on the simulated data show a improved azimuth resolution as was seen in Chapter 5. The cross coupling level and variations of the refractive index affect the resolution of the synthetic aperture processing. Figure 6.24 shows the result from the synthetic aperture algorithm applied to the real subtracted test data with refractive index 2.75. Figure 6.25 shows the result with refractive index increased by 15%. These reveal that the refractive index has a strong effect on the synthetic aperture calculation when applied to real data. In real situations the refractive index is not known, and is difficult to predict to the accuracy required for this calculation. Indeed, past workers [2] took many measurements of the refractive index of snowpack material before applying synthetic aperture calculations.

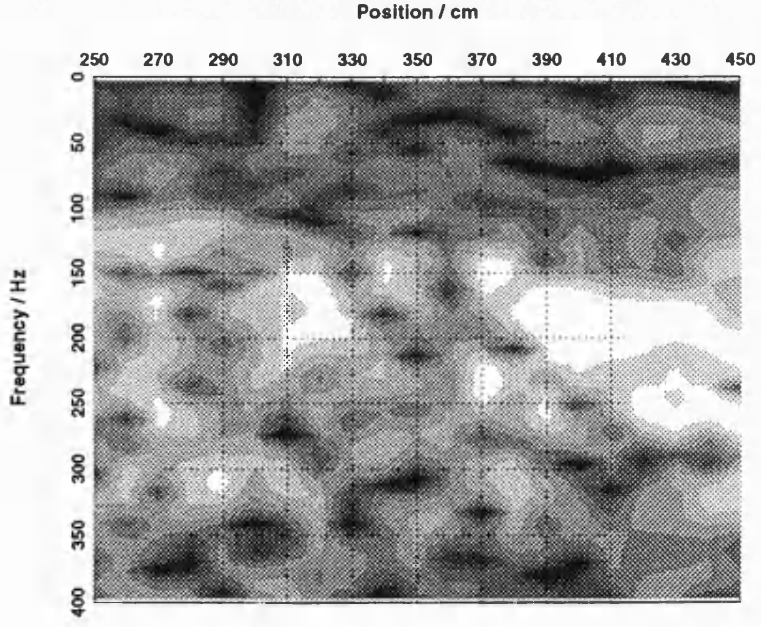

Figure 6.24: Synthetic aperture algorithm applied on the real subtracted data for channel 1 with refractive index 2.75, twelve uniform quasi-gray scales

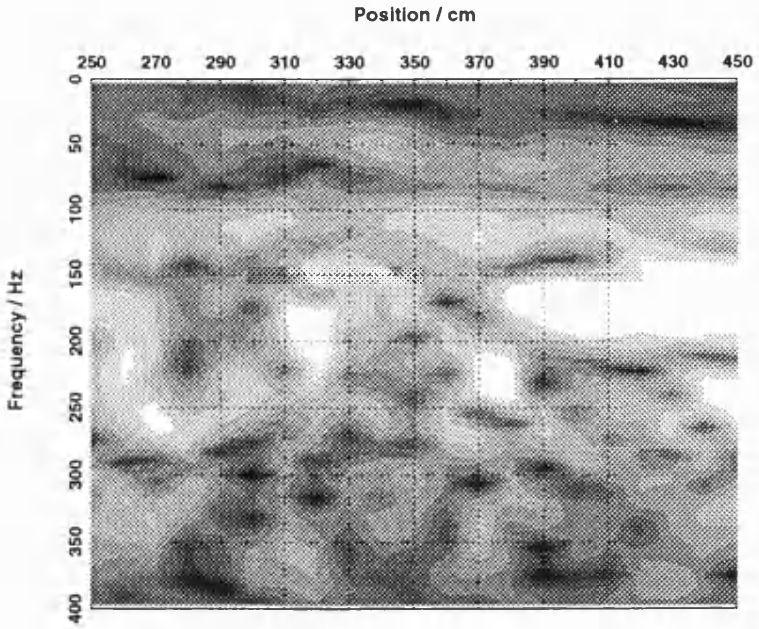

Figure 6.25: Synthetic aperture algorithm applied on the real subtracted data for channel 1 with 15% increased refractive index of Figure 6.24, twelve uniform quasi-gray scales

6.10 Conclusion

The experimental FMCW radar prototype system has been successfully tested using a sand filled test site in which three targets were buried at 290 offset, depth 30cm, 330 offset, depth 10cm and 390 offset, depth 30cm. For this multi-target situation using developed target analysis algorithm can detect these three targets' position and gives the correct depth reading for the outer two targets. For the middle shallow target, the original algorithm can indicate that a shallow target has been found, but its depth value could not be solved correctly. Using the limiter algorithm could ensure both the shallow or deep targets' depth can be calculated correctly and clear 2D target images produced.

This experimental target analysis only takes about ten seconds to measure one test point. The output is simple to understand and it is therefore, suitable for practical use. The 2D image information is useful for post-studying.

A set of matched filter algorithms can improve the image resolution, but it takes about 3 minutes to test each measurement point. This method can therefore only be used for post-processing.

A set of clutter rejection filter algorithms can also improve both the safe digging depth and unit movement results and the images, but the running time for each measured point is approximately 3.2 minutes which is makes it unsuitable for practical use.

The synthetic aperture algorithm for real data did not produce a clearing improved set of target images because of the unknown refractive index and limited scan times.

References

[1] Yamaguchi Y et al. Human body detection in wet snowpack by an FMCW radar. *IEEE Transactions on Geoscience and Remote Sensing*, GE-30(1):186–189, January 1992. Author(s) with University of Niigata, Japan.

[2] Yamaguchi Y et al. Synthetic aperture fm-cw radar applied to the detection of objects buried in snowpack. In *IEEE Transactions on Geoscience and Remote Sensing*, volume GE-32(1), pages 11–18, January 1994. Author(s) with Niigata University, Japan.

Chapter 7

Conclusion and Further Work

7.1 Outline

This chapter reviews the work undertaken to model and process FMCW ground penetrating radar signal. The review highlights novel aspects of the research and results from the simulation model and experimental system.

7.2 Review of Research Work

The introductory chapter of the thesis outlined the application of ground penetrating radar, its system and signal processing method, gave the background information about this research work and the outline of this thesis.

The literature review examined several signal processing techniques used by other researchers and indicated that the signal processing task for this research work is to produce analysis software suitable for real-time processing that is also easy to operate in a practical environment.

7.2.1 Signal Processing Mathematical Model Development

The purpose of the signal processing mathematical model for FMCW ground penetrating radar is to provide some predication of how the system will react to realistic situations. The model has been established and tested successfully by using some simulated target environments and parameters.

The signal processing mathematical model has been divided into two main parts: the radar system and target simulation model, and the target analysis model. The first part includes a UHF system model and a propagation model which calculates the transmitter, receiver, mixer signals in uniform, layered and trenched media. It uses a ray tracing algorithm, and outputs sampled time domain data.

The target analysis model processes the sampled time domain signal, takes the FFT of the data and convolves the separate receiver channel responses. From this it calculates the safe digging depth and determines the unit movement direction. This model employs convolution and triangulation measurement techniques to compute a safe digging depth above a buried target. These two techniques are novel aspects concerning target depth detection.

The convolution measurement technique convolves the data from two channels data in order to suppress the off-center target response and enhance the response of the target directly below the unit. The triangulation measurement technique enables the safe digging depth for a target to be computed when the refractive index of the soil is unknown.

The work on the signal processing mathematical model has developed the target algorithms to be used in the experimental system. This has been carried out by testing the algorithms using the target simulation software to verify the algorithm performance in uniform, layered and trenched media.

The simulation results show that safe digging depth can be calculated correctly when the target is directly under the unit centre for uniform, layered and trenched infill for both single and multiple target situations.

This mathematical model's resolution has been studied for horizontal, vertical and

offset vertical two targets situations. The results show that for twin targets at same depth, a "ghost" target can appear in their middle whose depth reading will be greater than the SDD of a real target when the twin targets' separation is greater than 0.4m. The unit movement direction arrows always tell the operator to move away from the "ghost" target when unit is around the "ghost" target. Conversely for real targets the operator will center over the target.

For twin targets buried at same horizontal position but at different depth, the resolution results show that the model correctly computes the safe digging depth when the target vertical separation is greater than 15cm.

For two different targets at different depths, the larger target being deeper, the results show that the SDD for the shallower target can be calculated correctly for all the target separations. The algorithm also detects the deeper, larger target with a correct depth computed for vertical separations above 0.25m.

This software was written in Microsoft QuickBasic. The total running time for measuring one point is approximately 48 seconds using a 486 DX50 computer. The total size of the model software is 150 KB.

7.2.2 SDD Quantisation Error

Using triangulation techniques to calculate target depth can eliminate the unknown refractive index of the infill, but due to the sampled data from UHF system the quantisation error could not be avoided. This quantisation error has an effect on the accuracy of the safe digging depth calculation.

The quantisation error has been studied in detail using Mathcad software. The effect of quantisation error on SDD can be reduced by increasing the resolution of the FFT and increasing the base line of the triangulation measurement. These two approaches have been investigated and the results show an improvement in the quantisation error performance. However after considering the practical limit of the specification of a one metre length unit, and the noise effect by increasing FFT resolution, the current system uses the 2D separation between R_A and R'_A and 2048 point FFT. This may be improved

on in the further work.

7.2.3 Investigation of Algorithms to Improve System Resolution

The work has been done to investigate some algorithms to process real tested data to improve system resolution.

The initial system tests show a very strong direct coupling between transmitter and receiver which makes it very difficult to detect a target. Several methods have been studied to remove or reduce the cross coupling and enhance the system ability to detect target under clutter.

Window functions have been examined on the sampled time domain data, and the results show a reduction of the sidelobes and a broadening of the main peak. However two relatively close main peaks merge into one and accuracy is then lost.

The output of target templating using $\frac{\sin x}{x}$ as template function left the spectrum shape unchanged and did not sharpen the peak. Triangular templating can produce the sharp peak but always at the frequency from which the template function was derived rather than the target frequency.

The reference signal subtraction method was the best for removing the direct coupling signal, and was tested using measured data. The subtraction of a reference $\frac{\sin x}{x}$ signal did not reduce the clutter effectively because the real signal has been distorted due to the frequency response of the UHF system, the variation in media attenuation with frequency and the reduced bandwidth of the antenna system.

The limiter algorithm has been tested on the subtracted data and shows improved results because the limiter remove amplitude modulation from the spectrum. It was seen to work best after reference signal subtraction, rather than before.

Several filter algorithms have been reviewed and developed. The inverse filter has a similar action to the triangle templating which is not suitable for practical use. Matched filters for white noise and nonwhite noise have also been studied. The results show that both filters can suppress sidelobes.

A set of matched filter and clutter rejection filter algorithms have been developed which use a varying frequency filter to filter the input signal. The output has a maximum peak when the filter's frequency equals the input signal's frequency. The filter searches the whole frequency band and determines the input signal's frequency. This is the target difference frequency, which is used to calculate SDD and unit movement.

A synthetic aperture algorithm has also been studied and tested. The results show the improved azimuth resolution of simulated data, but for the real data the synthetic aperture algorithm did not produce clear image because of the unknown refractive index. The index needs to be known to better than 15% for the synthetic aperture algorithm to be effective.

7.2.4 Experimental Results

The experimental FMCW prototype radar system has been produced and tested successfully by using the developed target analysis software on a sand filled test site.

Several tests have been made on the test site with three buried targets. The results show that the experimental system target analysis software can find targets and calculate their depth correctly. The 2D plots show very clear targets images.

Considering the requirements of this FMCW radar prototype, the target analysis software now includes reference signal subtraction, limiter algorithm, convolution, target flag and warning flag output and the calculation of safe digging depth and unit movement. Sophisticated filter and synthetic aperture algorithms can be used for post-processing to study 2D target images.

The target analysis software has been written in Borland C which has been integrated with UHF control and data acquisition software. The running time for measuring one point is about ten seconds, and provides the target safe digging depth, unit movement direction, target flag and warning flag. These are considered to be relatively easy to understand by most operators.

7.3 Further Work

The signal processing work on FMCW ground penetrating radar has been completed for this stage. Further work should be directed to achieve an improved FMCW GPR system for commercial use.

From the results provided in previous chapters, the cross coupling between transmitter and receiver is still a critical problem. One way to reduce the direct coupling is to change the antenna system, and another way is to seek for a software solution.

The frequency modulation profile of the current system is fixed using saw-tooth sweep. In the future, the signal processing system could process the target spectra and provide control signals to the UHF system to select other modulation waveforms. These could minimize the sidelobes of the target spectrum and obtain the optimal target response for calculating target safe digging depth.

Using different transmitter and receiver configurations to reduce quantisation could improve resolution of SDD.

A clutter rejection filter algorithm can improve system resolution, but the long processing time is not suitable for real-time processing. Further work can modify the program to reduce the running time and enable it to be used on the real time test.

The synthetic aperture algorithm for real application could also be studied further to obtain improved target images.

Appendix A

Safe Digging Depth Calculation Derivation

A.1 Derivation of Safe Digging Depth Calculation for a Known Refractive Index

Denoting the distance between T_A and R_A and R'_A as R_1 and R_2 respectively as shown in Figure A.1. D is the separation between transmitter and receiver using the cosine rule:

$$(R_1 - d)^2 = D^2 + d^2 - 2dD\cos(180 - \theta) \quad \text{(A.1)}$$

$$(R_2 - (R_1 - d))^2 = d^2 + (2D)^2 - 2d(2D)\cos\theta \quad \text{(A.2)}$$

Eliminating the term in $2dD$, we can get the following equation:

$$2(R_1 - d)^2 + (R_2 - (R_1 - d))^2 = 3d^2 + 6D^2$$

Solving this equation, the distance d and angle θ can be represented as below:

$$d = \frac{3R_1^2 - 2R_1R_2 + R_2^2 - 6D^2}{2(3R_1 - R_2)} \quad \text{(A.3)}$$

$$\cos(\theta) = \frac{1}{D}\left(\frac{R_1^2 - D^2}{2d} - R_1\right) \tag{A.4}$$

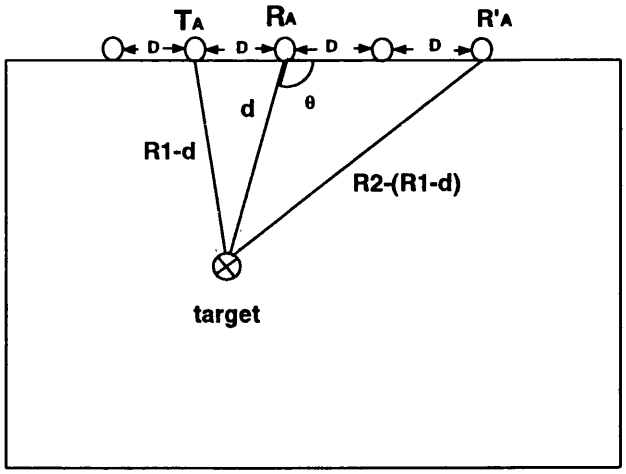

Figure A.1: SDD derivation profile

A.2 Derivation of Safe Digging Depth Calculation for an Unknown Refractive Index

Denoting the time delay between T_A and R_A, and R'_A as τ_1 and τ_2 respectively. Since $\tau = \frac{n}{c}R$, Where n is the unknown refractive index, c is the speed of light, then, τ_1, τ_2 can be expressed as following:

$$\tau_1 = \frac{n}{c}R_1 \tag{A.5}$$

$$\tau_2 = \frac{n}{c}R_2 \tag{A.6}$$

Divide Equation A.5 and A.6, we can cancel the unknown refractive index:

$$\frac{\tau_1}{\tau_2} = \frac{R_1}{R_2}$$

Because distance R_1 and R_2 can be represented as target depth d and the separation of transmitter and receiver D (Figure A.2):

$$R_1 = d + \sqrt{d^2 + D^2} \tag{A.7}$$

$$R_2 = \sqrt{d^2 + D^2} + \sqrt{d^2 + (2D)^2} \tag{A.8}$$

R_1, R_2 are convoluted data. Replacing R_1 and R_2 in Equation A.2 and uses $T = \frac{\tau_1}{\tau 2}$:

$$\frac{\tau_1}{\tau_2} = \frac{d + \sqrt{d^2 + D^2}}{\sqrt{d^2 + D^2} + \sqrt{d^2 + (2D)^2}} \tag{A.9}$$

Solving this equation, the target depth can be expressed as below:

$$d = \frac{D}{2} \frac{3T^2 + 2T - 1}{\sqrt{2T^2 - 3T^3 + T}} \tag{A.10}$$

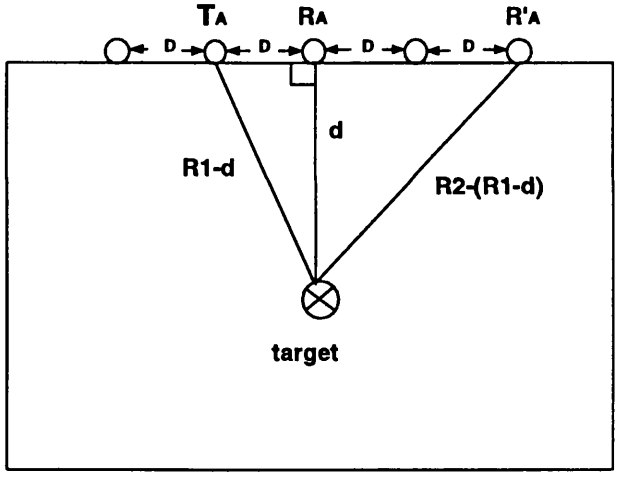

Figure A.2: SDD derivation profile for target directly below the unit center

Appendix B

Secant Method to Solve a Non-linear Equation

The Secant method has been used to solve a non-linear equation([1], [2]). It is a approximate of the Newton-Raphson method. This method use $\frac{f_n - f_{n-1}}{x_n - x_{n-1}}$ to replace the derivative $f'(x_n)$.

$$x_{n+1} = x_n - \frac{x_n - x_{n-1}}{f_n - f_{n-1}} f_n \tag{B.1}$$

The geometrically meaning of this method is that x_{n+1} is determined as the abscissa of the point of intersection between the secant through (x_{n-1}, f_{n-1}) and (x_n, f_n) and the x-axis.

The Secant method flowchart is shown in Figure B.1. Where the variables are as following:

x_1, x_2, a	variables
Δx	increment
$FNF()$	function
f_1, f_2, f_a	function value
ε	output tolerance

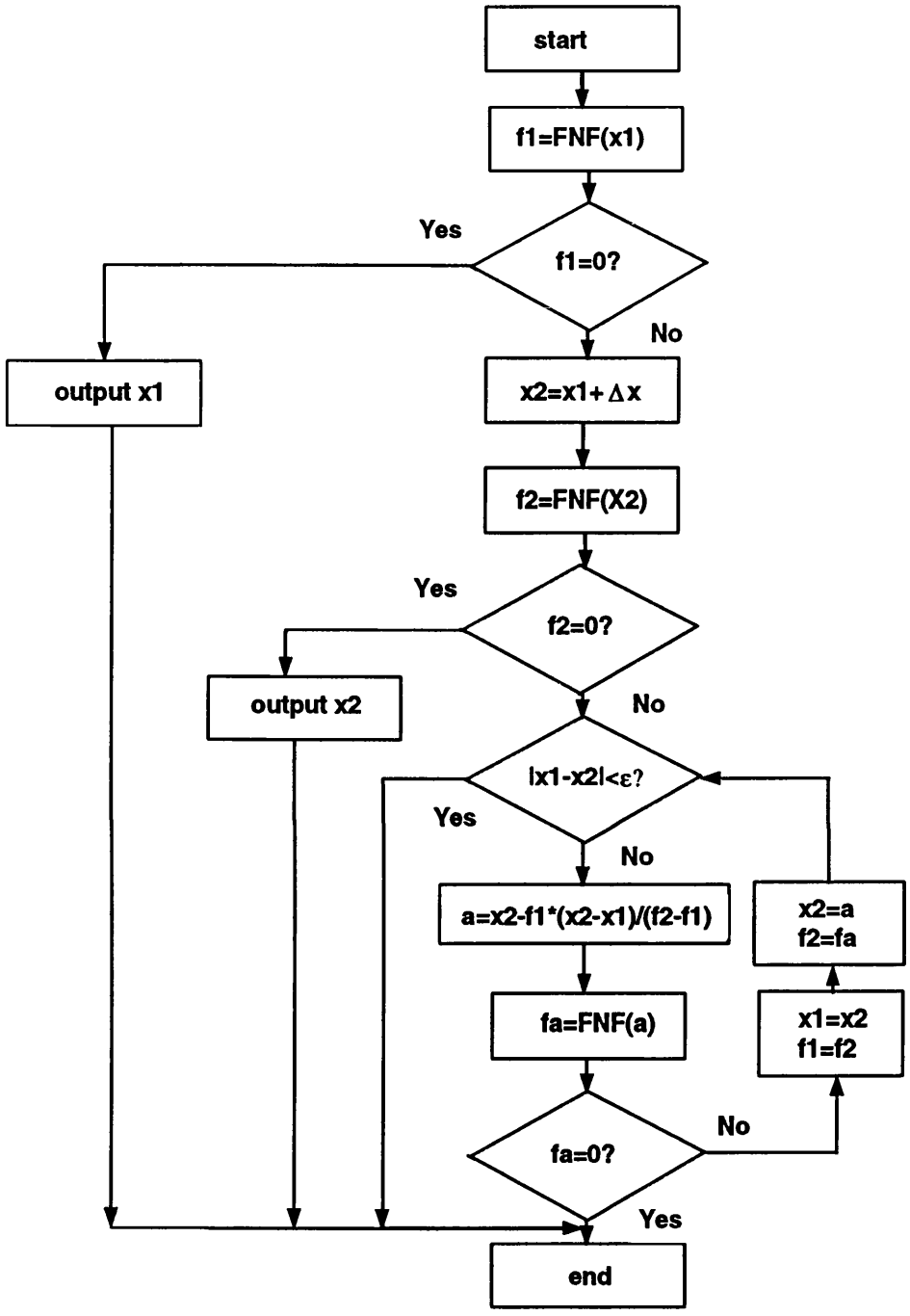

Figure B.1: Secant Method Flowchart

References

[1] Dahlquist G. *Numberical Methods.* Prentice-Hall, Inc, 1974.

[2] Lafara R L. *Computer Methods for Science and Engineering.* c, 1973.

Appendix C

Target Path Function in Layered Media

C.1 Target in the Second Layer

Figure C.1

$$FNP_{21} = \sqrt{l_1^2 + (y_1 - y_{un})^2} \tag{C.1}$$

$$FNP_{22} = \sqrt{(x_{ta} - l_1)^2 + (y_{ta} - y_1)^2} \tag{C.2}$$

$$FNF(y_1) = n_1(y_1 - y_{un})FNP_{22} - n_{21}(y_{ta} - y_1)FNP_{21} \tag{C.3}$$

C.2 Target in the Third Layer

Figure C.2

$$FNT_1 = \sqrt{n_{31}^2(l_1^2 + (y_1 - y_{un})^2 - n_1^2(y_1 - y_{un})^2} \tag{C.4}$$

$$y_2 = y_{ta} - \frac{(x_{ta} - l_1 - l_2)n_1(y_1 - y_{un})}{FNT_1} \tag{C.5}$$

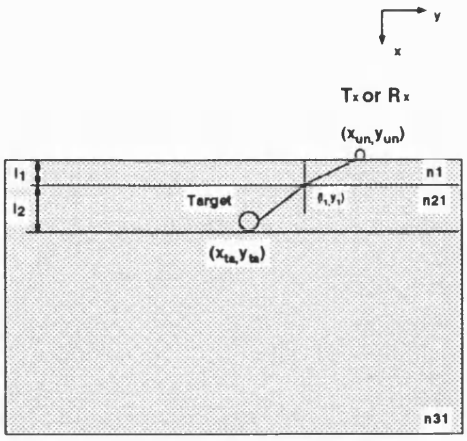

Figure C.1: Target in the Second Layer in the Layered Soil

$$FNF(y_1, y_2) = n_1(y_1 - y_{un})\sqrt{l_2^2 + (y_2 - y_1)^2} - n_{21}(y_2 - y_1)\sqrt{l_1^2 + (y_1 - y_{un})} \quad \text{(C.6)}$$

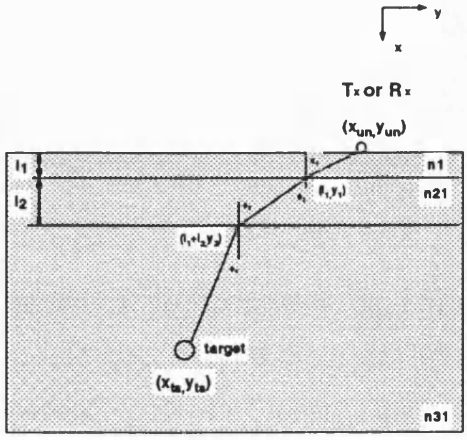

Figure C.2: Target in the Third Layer in the Layered Soil

Appendix D

Target Path Functions in Trenched Media

D.1 Target in n_{22}

D.1.1 Target Path $n_1 \rightarrow n_{22}$

Figure D.1

$$FNP_1 = \sqrt{l_1^2 + (y_1 - y_{un})^2} \tag{D.1}$$

$$FNP_2 = \sqrt{(y_{ta} - y_1)^2 + (x_{ta} - l_1)^2} \tag{D.2}$$

$$FNF(y_1) = n_1(y_1 - y_{un})FNP_2 - n_{22}(y_{ta} - y_1)FNP_1 \tag{D.3}$$

D.1.2 Target Path $n_1 \rightarrow n_{21} \rightarrow n_{22}$

Figure D.2

$$FNP_1 = \sqrt{l_1^2 + (y_1 - y_{un})^2} \tag{D.4}$$

$$FNP_3 = \sqrt{(x_1 - l_1)^2 + (y_1 - y_{t1})^2} \tag{D.5}$$

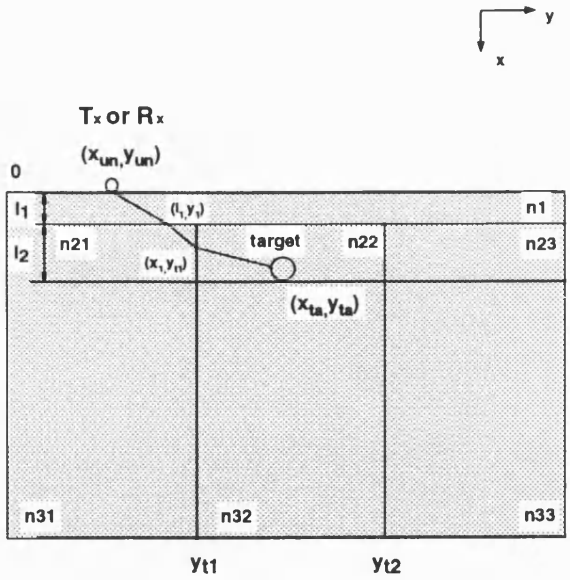

Figure D.1: Target Path $n_1 \rightarrow n_{22}$

$$FNP_4 = \sqrt{(y_{ta} - y_{t1})^2 + (x_{ta} - x_1)^2} \quad \text{(D.6)}$$

$$x_1 = \frac{\sqrt{n_{21}^2(y_{t1} - y_1)^2 FNP_1^2 - n_1^2(y_{t1} - y_1)^2(y_1 - y_{un})^2}}{n_1(y_1 - y_{un})} + l_1 \quad \text{(D.7)}$$

$$FNF(x_1, y_1) = n_{21}(x_1 - l_1)FNP_4 - n_{22}(x_{ta} - x_1)FNP_3 \quad \text{(D.8)}$$

D.1.3 Target Path $n_1 \rightarrow n_{23} \rightarrow n_{22}$

Figure D.3

$$FNP_1 = \sqrt{l_1^2 + (y_1 - y_{un})^2} \quad \text{(D.9)}$$

$$FNP_5 = \sqrt{(x_1 - l_1)^2 + (y_1 - y_{t2})^2} \quad \text{(D.10)}$$

$$FNP_8 = \sqrt{(x_{ta} - x_1)^2 + (y_{t2} - y_{ta})^2} \quad \text{(D.11)}$$

$$x_1 = \frac{\sqrt{n_{21}^2(y_{t2} - y_1)^2 FNP_1^2 - n_1^2(y_{t2} - y_1)^2(y_1 - y_{un})^2}}{n_1(y_1 - y_{un})} + l_1 \quad \text{(D.12)}$$

$$FNF(x_1, y_1) = n_{21}(x_1 - l_1)FNP_8 - n_{22}(x_{ta} - x_1)FNP_5 \quad \text{(D.13)}$$

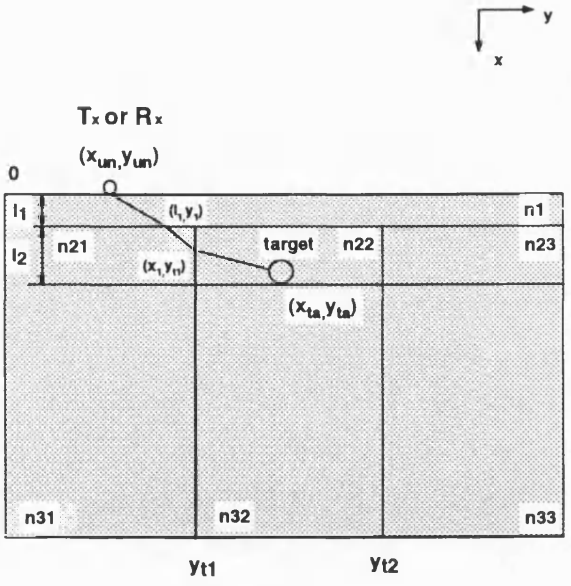

Figure D.2: Target Path $n_1 \rightarrow n_{21} \rightarrow n_{22}$

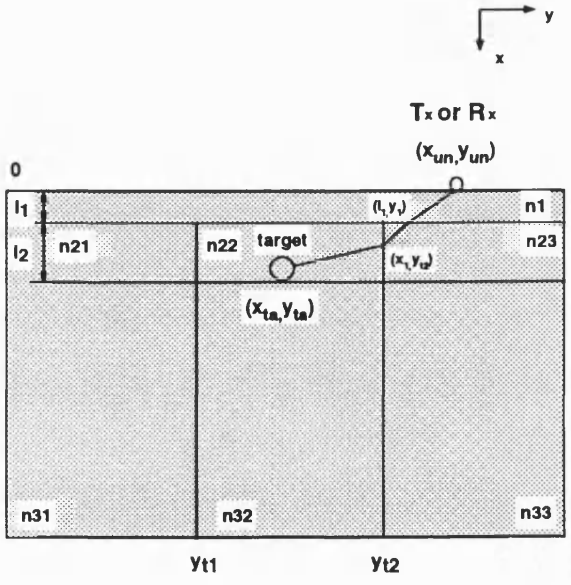

Figure D.3: Target Path $n_1 \rightarrow n_{23} \rightarrow n_{22}$

D.2 Target in n_{32}

D.2.1 Target Path $n_1 \rightarrow n_{22} \rightarrow n_{32}$

Figure D.4

$$FNP_1 = \sqrt{l_1^2 + (y_1 - y_{un})^2} \tag{D.14}$$

$$FNP_{10} = \sqrt{l_2^2 + (y_1 - y_2)^2} \tag{D.15}$$

$$FNP_{11} = \sqrt{(x_{ta} - l_1 - l_2)^2 + (y_2 - y_{ta})^2} \tag{D.16}$$

$$y_2 = y_1 - \frac{l_2 n_1 (y_{un} - y_1)}{\sqrt{n_{22}^2 FNP_1^2 - n_1^2 (y_1 - y_{un})^2}} \tag{D.17}$$

$$FNF(y_1, y_2) = n_{22}(y_1 - y_2)FNP_{11} - n_{32}(y_2 - y_{ta})FNP_{10} \tag{D.18}$$

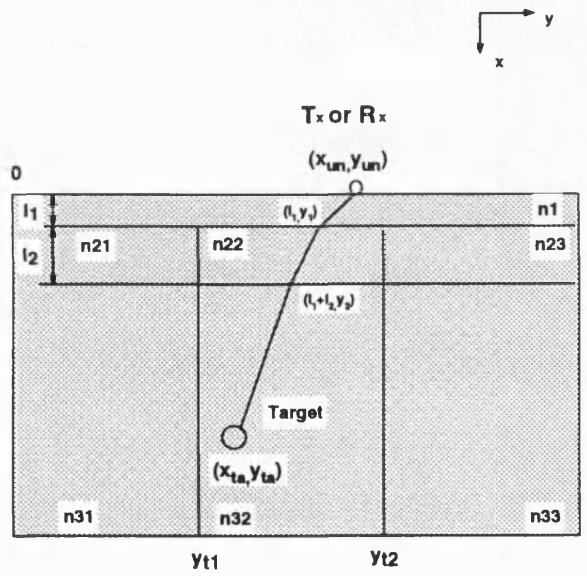

Figure D.4: Target Path $n_1 \rightarrow n_{22} \rightarrow n_{32}$

D.2.2 Target Path $n_1 \rightarrow n_{21} \rightarrow n_{31} \rightarrow n_{32}$

Figure D.5

$$FNP_1 = \sqrt{l_1^2 + (y_1 - y_{un})^2} \tag{D.19}$$

$$FNP_4 = \sqrt{(x_{ta} - x_1)_1^2 + (y_{ta} - y_{t1})^2} \tag{D.20}$$

$$FNP_{10} = \sqrt{l_2^2 + (y_1 - y_2)^2} \tag{D.21}$$

$$FNP_{12} = \sqrt{(x_{ta} - l_1 - l_2)^2 + (y_2 - y_{t1})^2} \tag{D.22}$$

$$y_2 = y_2 + \frac{l_2 n_1 (y_1 - y_{un})}{\sqrt{n_{21}^2 FNP_1^2 - n_1^2 (y_1 - y_{un})^2}} \tag{D.23}$$

$$x_1 = \frac{\sqrt{n_{31}^2 (y_2 - y_{t2})^2 FNP_{10}^2 - n_{21}^2 (y_1 - y_2)^2 (y_2 - y_{t1})^2}}{n_{21}(y_2 - y_1)} + l_1 + l_2 \tag{D.24}$$

$$FNF(x_1, y_1, y_2) = n_{31}(x_1 - l_1 - l_2) FNP_4 - n_{32}(x_{ta} - x_1) FNP_{12} \tag{D.25}$$

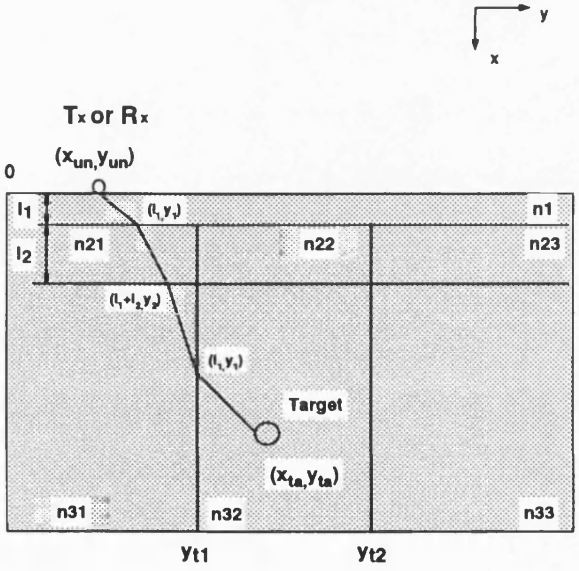

Figure D.5: Target Path $n_1 \rightarrow n_{21} \rightarrow n_{31} \rightarrow n_{32}$

D.2.3 Target Path $n_1 \rightarrow n_{21} \rightarrow n_{22} \rightarrow n_{32}$

Figure D.6

$$FNP_1 = \sqrt{l_1^2 + (y_1 - y_{un})^2} \tag{D.26}$$

$$FNP_{11} = \sqrt{(x_{ta} - l_1 - l_2)^2 + (y_2 - y_{ta})^2} \tag{D.27}$$

$$FNP_{12} = \sqrt{(x_{ta} - l_1 - l_2))^2 + (y_2 - y_{t1})^2} \tag{D.28}$$

$$x_1 = \frac{\sqrt{n_{21}^2 (y_1 - y_{t1})^2 FNP_1^2 - n_1^2 (y_1 - y_{t1})^2 (y_{un} - y_1)^2}}{n_1 (y_1 - y_{un})} + l_1 \tag{D.29}$$

$$FNPP = n_1^2(y_1 - y_{un})^2(x_1 - l_1)^2(l_1 + l_2 - x_1)^2 \quad \text{(D.30)}$$

$$y_2 = \frac{\sqrt{n_{22}^2(l_1 + l_2 - x_1)^2(y_{t1} - y_1)^2 FNP_1^2 - FNPP}}{n_1(y_1 - y_{un})} + y_{t1} \quad \text{(D.31)}$$

$$FNF(x_1, y_1, y_2) = n_{22}(y_2 - y_{t1})FNP_{11} - n_{32}(y_{ta} - y_2)FNP_{12} \quad \text{(D.32)}$$

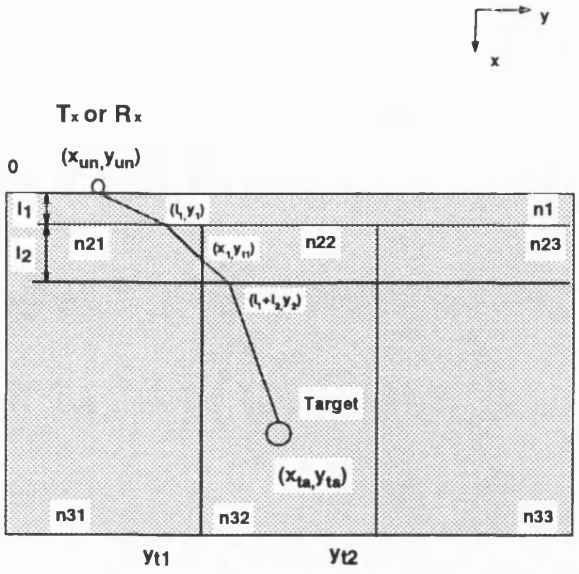

Figure D.6: Target Path $n_1 \rightarrow n_{21} \rightarrow n_{22} \rightarrow n_{32}$

D.2.4 Target Path $n_1 \rightarrow n_{23} \rightarrow n_{22} \rightarrow n_{32}$

Figure D.7

$$FNP_1 = \sqrt{l_1^2 + (y_1 - y_{un})^2} \quad \text{(D.33)}$$

$$FNP_{11} = \sqrt{(x_{ta} - l_1 - l_2)^2 + (y_2 - y_{ta})^2} \quad \text{(D.34)}$$

$$FNP_{13} = \sqrt{(x_1 - l_1 - l_2))^2 + (y_2 - y_{t2})^2} \quad \text{(D.35)}$$

$$x_1 = \frac{\sqrt{n_{23}^2(y_1 - y_{t2})^2 FNP_1^2 - n_1^2(y_1 - y_{t2})^2(y_{un} - y_1)^2}}{n_1(y_{un} - y_1)} + l_1 \quad \text{(D.36)}$$

$$y_2 = -\frac{\sqrt{n_{22}^2(l_1 + l_2 - x_1)^2 FNP_1^2 - n_1^2(y_1 - y_{un})^2(x_1 - l_1)^2(l_1 + l_2 - x_1)^2}}{n_1(y_{un} - l_1)} + y_{t2} \quad \text{(D.37)}$$

$$FNF(x_1, y_1, y_2) = n_{22}(y_{t2} - y_2)FNP_{11} - n_{32}(y_2 - y_{ta})FNP_{13} \quad \text{(D.38)}$$

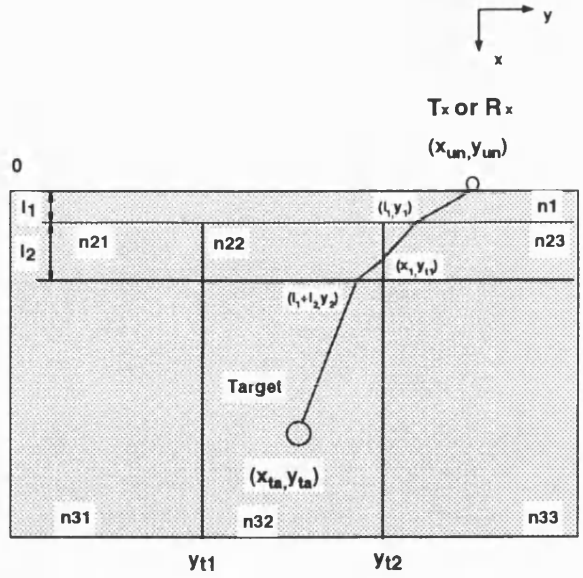

Figure D.7: Target Path $n_1 \rightarrow n_{23} \rightarrow n_{22} \rightarrow n_{32}$

D.2.5 Target Path $n_1 \rightarrow n_{23} \rightarrow n_{33} \rightarrow n_{32}$

Figure D.8

$$FNP_1 = \sqrt{l_1^2 + (y_1 - y_{un})^2} \tag{D.39}$$

$$FNP_8 = \sqrt{(x_{ta} - x_1)^2 + (y_{t2} - y_{ta})^2} \tag{D.40}$$

$$FNP_{10} = \sqrt{l_2^2 + (y_1 - y_2)^2} \tag{D.41}$$

$$FNP_{13} = \sqrt{(x_1 - (l_1 + l_2))^2 + (y_2 - y_{t2})^2} \tag{D.42}$$

$$y_2 = -\frac{l_2 n_1 (y_{un} - y_1)}{\sqrt{n_{23}^2 FNP_1^2 - n_1^2 (y_1 - y_{un})^2}} + y_1 \tag{D.43}$$

$$x_1 = \frac{\sqrt{n_{33}^2 (y_2 - y_{t2})^2 FNP_{10}^2 - n_{23}^2 (y_1 - y_2)^2 (y_2 - y_{t2})^2}}{n_{23}(y_1 - y_2)} + l_1 + l_2 \tag{D.44}$$

$$FNF(x_1, y_1, y_2) = n_{33}(x_1 - l_1 - l_2) FNP_8 - n_{32}(x_{ta} - x_2) FNP_{13} \tag{D.45}$$

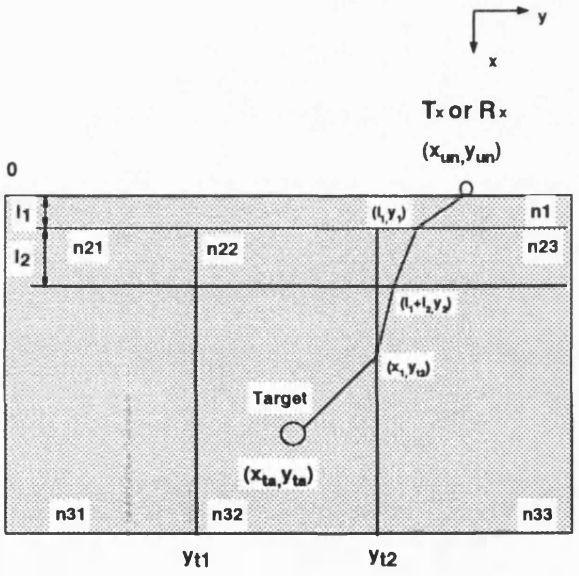

Figure D.8: Target Path $n_1 \rightarrow n_{23} \rightarrow n_{33} \rightarrow n_{32}$

Appendix E

Current FMCW System Configuration

A schematic diagram of the UHF sub-system design is shown in Figure E.1. The sub-system has been further sub-divided into four sub-systems:

- **Signal Generation Sub-System:** Generates a 250MHz to 750MHz signal for the transmitter sub-system by mixing a 1150MHz to 1650MHz sweep and a fixed 900MHz tone. The sub-system also provides a reference 1150MHz to 1650MHz swept frequency and a 900MHz tone to the receiver sub-system.
- **Transmitter Sub-System:** Provides amplification of the 250MHz to 750MHz signal to approx. +20dBm (10mW) for each channel using a number of amplifier stages.
- **Receiver Sub-System:** Amplifies the incoming signal from the antenna sub-system and uses an Intermediate Frequency (IF) of 900MHz in a two stage mixer to produce an audio-band frequency difference signal which is then filtered and amplified.
- **System Control and Data Acquisition Sub-System:** Provides the Frequency Modulation (FM) control signals to the signal generation sub-system to sweep the output frequency between 250MHz to 750MHz. The sub-system also produces the

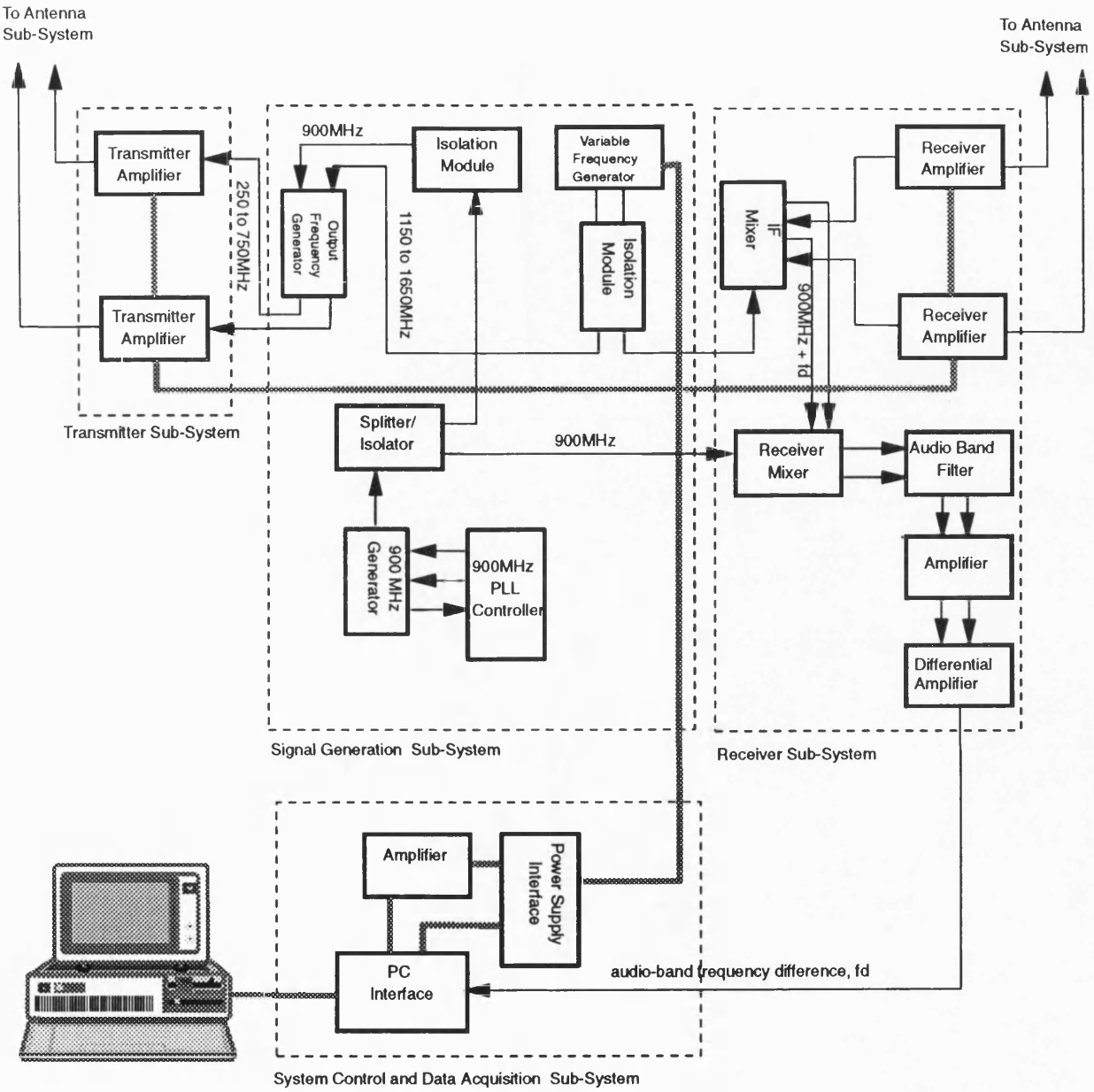

Figure E.1: UHF Sub-System Electronics

Amplitude Modulation (AM) control signals to the transmitter sub-system. The sub-system also samples the incoming audio-band frequency difference signal at a rate synchronised to the generation of the FM control signal.

Appendix F

Deviation of $\frac{\sin x}{x}$ Convolution with $\frac{\sin x}{x}$

This appendix gives the theoretical calculation of $\frac{\sin x}{x}$ Convolves $\frac{\sin x}{x}$.([1] [2]).

Suppose

$$f(t) = \frac{\sin \pi t}{\pi t}$$

The Fourier Transform of $f(t)$ is $F(\omega)$

$$\begin{aligned} F(\omega) &= \int_{-\infty}^{\infty} f(t) \exp(-j\omega t) dt \\ &= \int_{-\infty}^{\infty} \frac{\sin \pi t}{\pi t} (\cos \omega t - j \sin \omega t) dt \\ &= \int_{-\infty}^{\infty} \frac{\sin \pi t}{\pi t} \cos \omega t dt - j \int_{-\infty}^{\infty} \frac{\sin \pi t}{\pi t} \sin \omega t dt \end{aligned} \tag{F.1}$$

The integral of any odd function between symmetric limits is zero, thus

$$\int_{-\infty}^{\infty} \frac{\sin \pi t}{\pi t} \sin \omega t dt = 0$$

There remains then

$$F(\omega) = \int_{-\infty}^{\infty} \frac{\sin \pi t}{\pi t} \cos \omega t dt \tag{F.2}$$

By trigonometry, Equation F.2 becomes

$$\begin{aligned} F(\omega) &= \frac{1}{2}\int_{-\infty}^{\infty}\frac{\sin(\pi t+\omega t)}{\pi t}dt+\frac{1}{2}\int_{-\infty}^{\infty}\frac{\sin(\pi t-\omega t)}{\pi t}dt \\ &= \int_{0}^{\infty}\frac{\sin(\pi t+\omega t)}{\pi t}dt+\int_{0}^{\infty}\frac{\sin(\pi t-\omega t)}{\pi t}dt \end{aligned} \tag{F.3}$$

Using

$$\int_{0}^{\infty}\frac{\sin x}{x}dx=\frac{\pi}{2}$$

and substitute

$$a=\pi t+\omega t$$

$$b=\pi t-\omega t$$

Equation F.3 becomes

$$\begin{aligned} F(\omega) &= \frac{1}{\pi}\int_{0}^{\infty}\frac{\sin a}{a}da+\frac{1}{\pi}\int_{0}^{\infty}\frac{\sin b}{b}db \\ &= \frac{1}{2}+\frac{1}{2} \\ &= 1 \end{aligned} \tag{F.4}$$

Then

$$F(\omega)=\begin{cases} 1 & \text{if } |\omega|>\pi \\ 0 & \text{otherwise} \end{cases}$$

Using convolution property:

$$\mathcal{F}[f_1(t)*f_2(t)]=F_1(\omega)F_2(\omega)$$

here

$$\mathcal{F}[f(t)*f(t)]=F(\omega)F(\omega)=1$$

Then

$$\begin{aligned} g(t) &= \mathcal{F}^{-1}[\mathcal{F}(f(t)*f(t))] \\ &= \frac{1}{2\pi}\int_{-\pi}^{\pi}\exp(-j\omega t)d\omega \\ &= \frac{\sin\pi t}{\pi t} \end{aligned} \tag{F.5}$$

So

$$\frac{\sin x}{x} * \frac{\sin x}{x} = \frac{\sin x}{x}$$

References

[1] Arsac J. *Fourier Transform and the Theory of Distributions.* Prentice-Hall, Inc., 1966.

[2] Burdic WS, editor. *Radar Signal Analysis.* Prentice-Hall, Inc, 1968.